

CeCo₂P₂: a unique Co-antiferromagnetic topological heavy-fermion system with $P \cdot \mathcal{T}$ -protected Kondo effect and nodal-line excitations

Haoyu Hu,^{1,*} Yi Jiang,^{1,*} Defa Liu,^{2,3} Yulin Chen,^{4,5} Alexei M. Tsvelik,⁶ Yuanfeng Xu,⁷ Kristjan Haule,⁸ and B. Andrei Bernevig^{9,1,10,†}

¹Donostia International Physics Center (DIPC), Paseo Manuel de Lardizábal, 20018, San Sebastián, Spain

²School of Physics and Astronomy, Beijing Normal University, Beijing 100875, China

³Key Laboratory of Multiscale Spin Physics (Minsitry of Education), Beijing Normal University, Beijing 100875, China

⁴Department of Physics, University of Oxford, Oxford, OX1 3PU, United Kingdom

⁵School of Physical Science and Technology, ShanghaiTech University, Shanghai 201210, China

⁶Division of Condensed Matter Physics and Materials Science, Brookhaven National Laboratory, Upton, NY 11973-5000, USA

⁷Center for Correlated Matter and School of Physics, Zhejiang University, Hangzhou 310058, China

⁸Center for Materials Theory, Department of Physics and Astronomy, Rutgers University, Piscataway, NJ 08854, USA

⁹Department of Physics, Princeton University, Princeton, NJ 08544, USA

¹⁰IKERBASQUE, Basque Foundation for Science, 48013 Bilbao, Spain

Based on high-throughput screening [1] and experimental data [2], we find that CeCo₂P₂ is unique in heavy-fermion materials: it has a Kondo effect at a high temperature which is nonetheless below a Co-antiferromagnetic ordering temperature. This begs the question: how is the Kondo singlet formed? All other magnetic Kondo materials do not first form magnetism on the atoms whose electrons are supposed to screen the local moments. We theoretically explain these observations and show the multifaceted uniqueness of CeCo₂P₂: a playground for Kondo, magnetism, flat band, and topological physics. At high temperatures, the itinerant Co c electrons of the system form non-atomic bands with a narrow bandwidth, leading to a high antiferromagnetic transition temperature. We show that the quantum geometry of the bands promotes in-plane ferromagnetism, while the weak dispersion along the z direction facilitates out-of-plane antiferromagnetism. At low temperatures, we uncover a novel phase that manifests the coexistence of Co-antiferromagnetism and the Kondo effect, linked to the $P \cdot \mathcal{T}$ -protected Kramers' doublets and the filling-enforced metallic nature of c electrons in the antiferromagnetic phase. Subsequently, the emergence of the Kondo effect, in cooperation with glide-mirror- z symmetry, creates nodal-line excitation near the Fermi energy. Our results emphasize the importance of lattice symmetry and quantum geometry, Kondo physics, and magnetism in the understanding of the correlation physics of this unique compound. We also test our theory on the structurally similar compound LaCo₂P₂ and show how we are able to understand its vastly different phase diagram.

Introduction. The impact of symmetry and topology [3–5] in weakly correlated systems has been thoroughly explored, leading to significant success in both theory and experiment. Numerous topological materials, such as topological insulators [6–18], topological superconductors [19–26], and Dirac/Weyl semimetals [24, 27–48] have been extensively studied and their properties are now comprehensively understood. However, understanding the role of symmetry and topology in strongly correlated systems remains a challenging question. Recent advances in heavy-fermion materials have demonstrated that the interplay between lattice symmetry and correlation physics could potentially give rise to novel quantum phases, such as topological Kondo insulators [49–62] and Weyl Kondo semi-metals [63–66].

Recent experiments have discovered a unique topological heavy-fermion material, CeCo₂P₂, where the interplay among quantum geometry, band topology, Kondo effect, and magnetism gives rise to novel quantum phases [2]. This system contains two types of electrons: the itinerant c electrons, which include the d orbitals of Co and Ce as well as the p orbitals of P, and the correlated f electrons of Ce. The

experimental and theoretical phase diagram [2] is shown in Fig. 1, which highlights several unique features of the systems. Firstly, unlike in conventional heavy-fermion compounds where only the correlated f -electrons develop ordering, here c -electrons from Co atoms develop antiferromagnetic (AFM) order and the transition temperature ($T_{\text{AFM}} \sim 450\text{K}$) is also relatively high. Secondly, a Kondo effect develops at $T_{\text{Kondo}} \sim 100\text{K}$ inside the AFM phase, which contrasts with the conventional expectation that magnetism suppresses the Kondo effect. The coexistence of the Kondo effect and magnetism has also been observed in other heavy-fermion materials, including USb₂[67], UAs₂[68], and CeCoGe₃[69]. In all these compounds, both magnetism and the Kondo effect originate from the f -electron states, and the magnetic transition temperature is comparable to or lower than the Kondo temperature. The coexistence is attributed to the distinct behaviors of f electrons associated with different orbitals or different lattice sites[67–69]. In contrast, in CeCo₂P₂, the AFM order is formed by the c electrons (d orbitals of Co atoms), rather than the f electrons, and the AFM ordering temperature is much higher than the Kondo temperature. These distinctions suggest a fundamentally different mechanism for the coexistence of Kondo screening and magnetism in CeCo₂P₂. Finally, a topological nodal-line excitation can appear inside the AFM Kondo phase. In this work, we provide a theoretical understanding of these experimental observations. We

* These authors contributed equally to this work.

† bernevig@princeton.edu

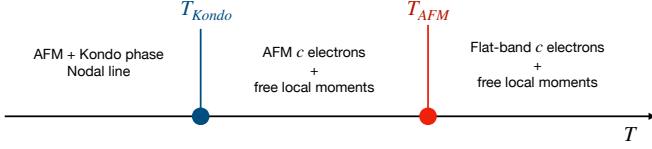


Figure 1. Theoretical and experimental phase diagram of the system.

demonstrate that the AFM order of Co c electrons is driven by their narrow bands, which feature non-trivial quantum geometry. The development of the Kondo effect in the AFM phase arises from the $P \cdot \mathcal{T}$ symmetry, where P represents inversion and \mathcal{T} denotes time-reversal transformation, and the filling-enforced metallic nature of the c electrons. The $P \cdot \mathcal{T}$ symmetry facilitates the formation of Kondo singlets involving c electrons from different layers. Concurrently, the metallic nature of the c electrons ensures a non-zero density of states, which is essential for the Kondo screening. Additionally, at low temperatures, the emergent Kondo excitation could form glide-mirror- z -symmetry-protected nodal-line excitation. We also note that earlier theoretical study[70] on this compound has primarily focused on surface effects in the AFM phase and Kondo effects in the paramagnetic phase. In contrast, our work provides new insights into the origin of antiferromagnetism, the coexistence of Kondo screening and magnetic order, and the topological properties of the system.

Finally, we also test our theory on a similar compound, LaCo_2P_2 , and explain the large differences between the two materials.

Model. The paramagnetic (PM) phase of the CeCo_2P_2 is described by space group 139 (I4/mmm). The Hamiltonian of the system (see Section III) can be written as $H = H_c + H_{c,U} + H_f + H_V$. H_c and $H_{c,U}$ are the kinetic term and interacting term of c electrons respectively. H_f describes the on-site coupling of f electrons including the Hubbard repulsion, spin-orbit couplings, and crystal field splitting. H_V is the hybridization between f and c electrons. We use $f_{\mathbf{R},a,i,\sigma}$ and $c_{\mathbf{R},a,i,\sigma}$ to describe the f electrons and c electrons respectively, where \mathbf{R} is the position of the unit cell, a is the sublattice index, i is the orbital index and σ is the spin index.

Narrow bands in the paramagnetic phase. In the high-temperature paramagnetic phase, due to the absence of the Kondo effect and strong Coulomb repulsion of f electrons, the low-energy single-particle excitation comes from c electrons. We perform *ab-initio* DFT calculations in the PM phase by treating f electrons as core states. In Fig. 2 (a), we show the band structures and density of states (DOS) obtained from DFT calculations. We observe a relatively flat (narrow) band near the Fermi energy formed by $d_{x^2-y^2}$ and d_{z^2} orbitals of Co atoms. The relatively flat bands produce an enhanced peak in the DOS. Such flat bands can be modeled by a two-orbital model in the primitive cell that only contains d_{z^2} and $d_{x^2-y^2}$ orbitals of Co atoms (Fig. 2 (b)). The Hamiltonian is $H_c = \sum_{\mathbf{k},\sigma} \psi_{\mathbf{k},\sigma}^\dagger h_{\mathbf{k}} \psi_{\mathbf{k},\sigma}$ (see Section V) with

$$\psi_{\mathbf{k}} = [c_{\mathbf{k},C_{O1},d_{z^2}}, c_{\mathbf{k},C_{O2},d_{z^2}}, c_{\mathbf{k},C_{O1},d_{x^2-y^2}}, c_{\mathbf{k},C_{O2},d_{x^2-y^2}}]$$

$$\begin{aligned} h_{\mathbf{k}} &= \begin{bmatrix} \epsilon_1 & 0 \\ 0 & \epsilon_2 \end{bmatrix} \tau_0 + \begin{bmatrix} 0 & n_{\mathbf{k}} \\ n_{\mathbf{k}} & g_{\mathbf{k}} \end{bmatrix} \tau_x \\ g_{\mathbf{k}} &= 4t_1 \cos\left(\frac{k_1 + k_3}{2}\right) \cos\left(\frac{k_2 + k_3}{2}\right) \\ n_{\mathbf{k}} &= -4t_2 \sin\left(\frac{k_1 + k_3}{2}\right) \sin\left(\frac{k_2 + k_3}{2}\right) \end{aligned} \quad (1)$$

where $\tau_{x,0}$ are Pauli matrices in the sublattice space. Without hopping between two orbitals ($t_2 = 0$), $d_{x^2-y^2}$ orbitals develop dispersive bands near the Fermi energy. After turning on the t_2 , additional effective hoppings between $d_{x^2-y^2}$ orbitals will be induced by t_2 via second-order perturbation effect. This additional contribution reduces the bandwidth of $d_{x^2-y^2}$ band and generates a relatively flat band (see Section V).

Flat-band magnetism. The narrow band and the corresponding enhanced DOS peak indicate strong magnetic instability. To understand the corresponding magnetic order, we first discuss the properties of narrow bands. The narrow bands are non-atomic along x, y directions which can be observed by the large hopping of d orbitals along x, y directions ($\sim 0.3\text{eV}$), but is atomic along z directions which can be seen by the small hopping of d orbitals along z directions ($\sim 0.04\text{eV}$). We now demonstrate this type of flat band will favor a type-A AFM order.

We first ignore the weak z -direction hopping of the system. Then, we have an effective 2D system with non-atomic flat bands near Fermi energy. For non-atomic flat band with projected Hubbard interactions, ferromagnetic state has the lowest energy [71–73] (see Section XIV). This mechanism accounts for the in-plane ferromagnetism observed in the system. The weak z -direction hopping, via second-order perturbation theory [74], generates an effective AFM coupling (see Section XIV). This effective AFM coupling combined with the in-plane ferromagnetism leads to a type-A antiferromagnetism with magnetic structure shown in Fig. 1 (d). The corresponding magnetic group is $P14/nnc$ (No. 126.386). We confirm our result with both mean-field and DFT calculations (see Section VI).

We therefore conclude the narrow bands near Fermi energy stabilize a type-A AFM phase. We present the band structures of the AFM phase in Fig. 2 (c), where we can observe the splitting of the narrow bands. Finally, we comment that the narrow bandwidth also indicates strong instabilities due to its enhanced density of states. This can be seen from the large energy difference ($\sim 0.24\text{eV}$) between the type-A AFM phase and PM phase. This also naturally explains the relatively high AFM transition temperatures.

After the development of the type-A AFM phase, we need to use the primitive cell of the AFM phase which is twice the size of the primitive cell of the PM phase (see Section II).

Comparison with LaCo_2P_2 . We also investigate the magnetism of LaCo_2P_2 , a material closely related to CeCo_2P_2 . Experimentally, LaCo_2P_2 develops a ferromagnetic order instead of a type-A AFM order [75]. The distinction in magnetic structures can be attributed to the differences in the distances between P atoms along the z direction. The P-P distance in LaCo_2P_2 is greater than that in CeCo_2P_2 [75], leading to weaker z -direction hopping between the p_z orbitals of

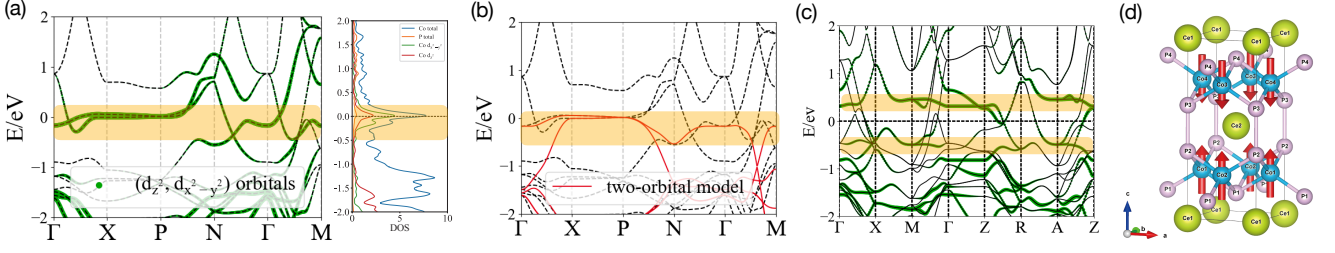


Figure 2. (a) DFT band structures in the primitive cell and density of states of PM phase. Green dot marks the weight of Co (d_{z^2} , $d_{x^2-y^2}$) orbitals. (b) Comparison between band structures of two-orbital model (red lines) and DFT model (dashed black lines). The two-orbital model successfully reproduces the narrow bands near the Fermi energy. (c) DFT band structures of AFM phase. Green dot marks the weight of Co (d_{z^2} , $d_{x^2-y^2}$) orbitals. The yellow-shaded region marks the narrow bands. (d) Magnetic structure of the system.

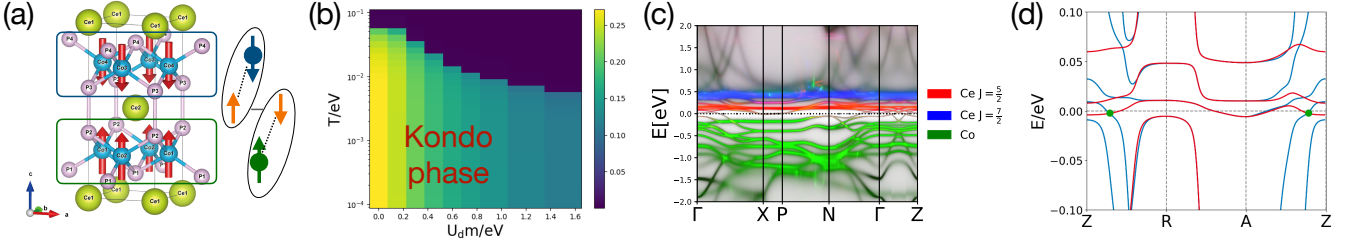


Figure 3. (a) Illustration of Kondo-singlet formation in the AFM phase. The spin \uparrow c electrons of Co-P layer I (green) and spin \downarrow c electrons of Co-P layer II (blue) are degenerate and form the Kondo singlet with the f local moments of Ce (orange). (b) Evolution of the $f c$ hybridization strength $\chi \sim \langle f^\dagger c \rangle$ at different strength of Co magnetic orders (U_{dm}) and temperatures T . We observe the stability of the Kondo phase, even in the presence of strong magnetic ordering. We can observe the Kondo temperature tends to saturate as we increase U_{dm} . (c) Spectrum of the Kondo phase obtained from embedded DMFT (DFT+DMFT) calculations. Different colors indicate the spectral weight contributions from various electronic components. (d) Band structures of the Kondo phase in a smaller energy window (obtained from large- N calculations). Red and blue mark the bands with opposite glide-mirror- z eigenvalues. We can observe the formation of the nodal line as marked by green dots.

P atoms. Consequently, this results in the mirror-even states formed by $p_z @ P$ in LaCo_2P_2 being lower in energy and appearing near the Fermi energy (see Section VII). These mirror-even states, with a Wannier center located between two Co layers, interact with Co d electrons from adjacent layers. This interaction induces effective ferromagnetic Ruderman-Kittel-Kasuya-Yosida (RKKY) interactions between the Co d electrons of the neighboring layers, thereby stabilizing the ferromagnetic state (see Section VII).

Development of Kondo effect in the antiferromagnetic phase. The specific magnetic structure, stabilized by the relatively narrow bands, induces a Kondo effect at low temperatures. Experimentally, a Kondo phase has been observed within the AFM phase, below $T_{\text{Kondo}} \sim 100\text{K}$ [2]. The co-existence of Co magnetism and the Kondo effect contrasts with conventional expectations and can be attributed to the $P \cdot \mathcal{T}$ symmetry present in the magnetic phase and the filling-enforced metallic nature of the c electrons.

Conventionally, the magnetic order is expected to suppress the spin-flipping scattering between f and c electrons by polarizing the electrons. This spin-flipping scattering is important for the Kondo effect and is directly generated by the Kondo coupling $\sim J_K(S_f^+ s_c^- + S_f^- s_c^+)$. Here, S_f^\pm, s_c^\pm denote the spin ladder operator of f and c electrons respectively. Consequently, the magnetic order is expected to suppress the

Kondo effect.

However, it is important to note the specific layered structure and the $P \cdot \mathcal{T}$ symmetry of the system. Each Ce layer is sandwiched between one Co-P layer above (layer I) and one below (layer II), as illustrated in Fig. 3 (a). Within each Co-P layer, electrons exhibit in-plane ferromagnetic ordering, while the spin moments of two adjacent layers are antiparallel. If only one of the two Co-P layers is considered, the Kondo effect would be suppressed due to the polarization of electrons within a single layer which also leads to a polarization of the f electrons. However, due to the $P \cdot \mathcal{T}$ symmetry, the spin \uparrow electrons of layer I ($c_{I,\uparrow}$) and spin \downarrow electrons of layer II ($c_{II,\downarrow}$) are energetically degenerate and form Kramers' doublets. Moreover, $P \cdot \mathcal{T}$ symmetry also ensures that the magnetic order of c electrons will not induce a magnetic order of f electrons from a Hartree-Fock contribution. Then, when the Kramers' doublet states of c electrons appear near the Fermi energy, a Kondo effect can then develop from the formation of the following type of spin-singlet state

$$\frac{1}{\sqrt{2}}(c_{I,\uparrow}^\dagger f_{\downarrow}^\dagger - c_{II,\downarrow}^\dagger f_{\uparrow}^\dagger)|0\rangle \quad (2)$$

where f_σ denotes the corresponding f electrons. An illustration of such Kondo singlet formation has also been shown in Fig. 3 (a).

We now show c electrons must be gapless, and the Kramers' doublets must appear at the Fermi energy. In the AFM phase with the magnetic group (126.386), the system must be metallic, due to the connectivity of the bands, if the total filling $n \bmod 4 \neq 0$ (see Section X 1). Since there are a total of 78 c electrons and $78 \bmod 4 = 2 \neq 0$, the c electrons are indeed gapless. This implies that the magnetic order cannot create a gap at the Fermi energy. This gapless nature further supports the development of the Kondo effect, as the formation of Kondo singlets requires the c electrons to appear near the Fermi energy [76].

We now demonstrate the stability of the Kondo effect from the mean-field calculations [76, 77]. We consider the following Kondo lattice model

$$H_{KL} = H_c^{\text{AFM}} + H_f + H_{\text{Kondo}}. \quad (3)$$

H_c^{AFM} represents the kinetic term of c electrons in the AFM phase. H_f is the interacting Hamiltonian of f electrons. H_{Kondo} is the Kondo coupling terms obtained from Schrieffer-Wolff transformation [78] (see Section IX).

We begin with a simplified model that includes only the $d_{x^2-y^2}, d_{z^2}$ orbitals of Co and the lowest Kramer-doublet states of Ce. We describe H_c^{AFM} by adding the a mean-field term to the non-interacting Hamiltonian H_c (Eq. 1)

$$H_c^{\text{AFM}} = H_c + H_{c,\text{MF}},$$

$$H_{c,\text{MF}} = mU_d \sum_{\mathbf{R},a,i,\sigma} s(\mathbf{R} + \mathbf{r}_a) \left(\sigma c_{\mathbf{R},a,i,\sigma}^\dagger c_{\mathbf{R},a,i,\sigma} \right) \quad (4)$$

where U_d is the Hubbard interactions of d electrons, m denotes the magnetic moments formed by these electrons, and $s(\mathbf{R} + \mathbf{r}_a) = \pm 1$ characterize the direction of the magnetic moment for the type-A AFM phase (Fig. 2 (d)). To explore the interplay between magnetic ordering and the Kondo effect, we treat the product of m and U_d as our tuning parameters and solve the Kondo Hamiltonian at the mean-field level. The hybridization fields $\chi \sim \langle f^\dagger c \rangle$ (see Section IX) are used to characterize the Kondo effect, where $|\chi| \neq 0$ indicates the development of the Kondo effect. We present the phase diagram in Fig. 3 (b). As we increase the strength of magnetic ordering (mU_d , with m the magnetic moments and U_d the Hubbard interactions of Co), the Kondo temperature initially decreases but eventually converges to a finite value. Thus, irrespective of the strength of the magnetic ordering, there exists a robust mechanism, the $P \cdot \mathcal{T}$ -protected Kramers' doublet states, that supports the development of the Kondo effect. In addition, we find that breaking $P \cdot \mathcal{T}$ symmetry suppresses the Kondo effect and can eventually destroy it when the symmetry breaking becomes sufficiently strong (see Section X 2). Therefore, the disorder effect that breaks $P \cdot \mathcal{T}$ symmetry could also suppress the Kondo effect. However, given that the hybridization function in the current system is relatively large, we expect that weak disorder will not qualitatively affect the Kondo effect.

To further substantiate the stability of the Kondo effect, we perform both mean-field (or large- N) calculations for using the complete electronic model derived from DFT calculations, which includes all orbitals (d orbitals of Ce and Co

and p orbitals of P) (see Section IX), and an embedded dynamical mean-field theory (eDMFT) calculation[79–82] (see Section X). In both calculations, we have observed a Kondo effect within the AFM phase. The interacting single-particle spectrum obtained from eDMFT is shown in Fig. 3 (c), where we could observe f electron bands (marked by red) appeared near the Fermi energy. Within eDMFT calculations, we have also observed a relatively high Kondo temperature ($> 100\text{K}$), which could be attributed to the relatively large hybridization functions (see Section X).

Nodal line in the Kondo phase. In our simulations, we have also observed that the correlated f -electron excitations form a topologically non-trivial band. This non-trivial band topology is illustrated in Fig.3 (d). At the $k_z = 1/2$ plane, the glide-mirror- z symmetry protects a nodal line [83–85].

At the $k_z = 1/2$ plane, each band is two-fold degenerate due to the $P \cdot \mathcal{T}$ symmetry. Furthermore, two degenerate bands share the same eigenvalue under glide-mirror- z symmetry, which is either

$$ie^{i\pi(k_x+k_y)} \text{ or } -ie^{i\pi(k_x+k_y)} \quad (5)$$

In Fig. 3 (d), bands with different glide-mirror- z eigenvalues are indicated by different colors. Here, the formation of a nodal line near the Fermi energy is evident between two bands with opposite glide-mirror- z eigenvalues.

Finally, we explore the surface states of our model by considering the system with an open boundary along the z -direction. At any fixed k_x, k_y , the system can be treated as an effective one-dimensional (1D) system, with $P \cdot \mathcal{T}$ and $\{M_Z|1/2, 1/2, 1/2\}$ symmetries. We then first analyze the surface states of the three-dimensional (3D) system by investigating those of the effective 1D system. In such an effective 1D framework, surface states could emerge if the ground state is an obstructed atomic insulator (OAI) [86–90]. However, as we will demonstrate, this system only has trivial surface states.

In the effective 1D system, Co atoms occupy the only maximal Wyckoff positions ($2a$), with R_z coordinates at $1/4$ and $3/4$. Meanwhile, Ce and P atoms are located at non-maximal Wyckoff positions $4b$ with $R_z = 0+z, 0-z, 1/2+z, 1/2-z$. The effective 1D system has two types of elementary band representations (EBRs) [3–5, 91, 92], denoted by EBR^+ and EBR^- . EBR^+ (EBR^-) corresponds to placing an s -orbital with spin \uparrow (\downarrow) at $R_z = 1/4$ and an s -orbital with spin \downarrow (\uparrow) at $R_z = 3/4$. By shifting the values of k_x, k_y from inside the nodal line to outside, one of the filled, two-fold degenerate bands with EBR^- becomes empty, and one of the empty, two-fold degenerate bands with EBR^+ becomes filled. Since Co atoms already occupy the only maximal Wyckoff positions, the effective 1D system does not form an OAI; thus, we do not expect the existence of non-trivial surface states. However, given that P and Ce atoms are located at non-maximal Wyckoff positions, they could potentially form molecular orbitals with Wannier centers that are distinct from the atomic positions. If the boundary of the system cuts through these molecular orbitals, trivial surface states could still emerge. As demonstrated in our simple model, which features only one d orbital at the Co site and one f orbital at the Ce site (see

Section XII), this mechanism indeed produces surface states. Since these surface states are not symmetry-protected in-gap states, we can introduce an additional boundary term to merge them into the bulk spectrum(see Section XII).

Summary. In this work, we theoretically analyze the phase diagrams of a unique heavy-fermion material CeCo_2P_2 . Key results include: (1) the quantum geometry and relatively narrow bands of Co d orbitals stabilize a type-A AFM phase; (2) the $P \cdot T$ symmetry and the filling-enforced metallic c electrons offer a robust mechanism that supports the development of the Kondo phase, even within the magnetically ordered phase; (3) the composite f -electron excitations in the Kondo phase exhibit non-trivial band topology characterized by a glide-mirror- z -protected nodal line.

ACKNOWLEDGMENTS

We thank Silke Paschen for the initial collaboration. H. H. and Y. J. were supported by the European Research Council (ERC) under the European Union’s Horizon 2020 research and innovation program (Grant Agreement No. 101020833). D.L. and Y.X. were supported by the National Natural Science Foundation of China (General Program no. 12374454, 12374163) and the Fundamental Research Funds for the Central Universities (grant no. 226-2024-00200). B.A.B was supported by the Gordon and Betty Moore Foundation through Grant No.GBMF8685 towards the Princeton theory program, the Gordon and Betty Moore Foundation’s EPIQS Initiative (Grant No. GBMF11070), Office of Naval Research (ONR Grant No. N00014-20-1-2303), Global Collaborative Network Grant at Princeton University, BSF Israel US foundation No. 2018226, NSF-MERSEC (Grant No. MERSEC DMR 2011750), Simons Collaboration on New Frontiers in Superconductivity and the Schmidt Foundation at the Princeton University.

-
- [1] Y. Xu, L. Elcoro, Z.-D. Song, B. J. Wieder, M. Vergniory, N. Regnault, Y. Chen, C. Felser, and B. A. Bernevig, *Nature* **586**, 702 (2020).
- [2] D. F. Liu, Y. F. Xu, H. Y. Hu, J. Y. Liu, T. P. Ying, Y. Y. Lv, Y. Jiang, C. Chen, Y. H. Yang, D. Pei, D. Prabhakaran, M. H. Gao, J. J. Wang, Q. H. Zhang, F. Q. Meng, B. Thiagarajan, C. Polley, M. Hashimoto, D. H. Lu, N. B. M. Schröter, V. N. Strocov, A. Louat, C. Cacho, D. Biswas, T. L. Lee, P. Steadman, P. Bencok, Y. B. Chen, L. Gu, T. Hesjeda, G. van der Laan, H. Hosono, L. X. Yang, Z. K. Liu, H. Q. Yuan, B. A. Bernevig, and Y. L. Chen, *Discovery of an anti-ferromagnetic topological nodal-line kondo semimetal* (2024), arXiv:2411.13898 [cond-mat.str-el].
- [3] B. Bradlyn, L. Elcoro, J. Cano, M. G. Vergniory, Z. Wang, C. Felser, M. I. Aroyo, and B. A. Bernevig, *Nature* **547**, 298 (2017).
- [4] J. Cano, B. Bradlyn, Z. Wang, L. Elcoro, M. G. Vergniory, C. Felser, M. I. Aroyo, and B. A. Bernevig, *Physical Review B* **97**, 035139 (2018).
- [5] L. Elcoro, B. J. Wieder, Z. Song, Y. Xu, B. Bradlyn, and B. A. Bernevig, *Nature communications* **12**, 5965 (2021).
- [6] C.-X. Liu, X.-L. Qi, H. Zhang, X. Dai, Z. Fang, and S.-C. Zhang, *Physical Review B* **82**, 045122 (2010), publisher: American Physical Society.
- [7] M. Z. Hasan and C. L. Kane, *Rev. Mod. Phys.* **82**, 3045 (2010).
- [8] X.-L. Qi and S.-C. Zhang, *Reviews of Modern Physics* **83**, 1057 (2011).
- [9] Y. Ando and L. Fu, *Annual Review of Condensed Matter Physics* **6**, 361 (2015).
- [10] Y. L. Chen, J. G. Analytis, J.-H. Chu, Z. K. Liu, S.-K. Mo, X. L. Qi, H. J. Zhang, D. H. Lu, X. Dai, Z. Fang, S. C. Zhang, I. R. Fisher, Z. Hussain, and Z.-X. Shen, *Science* **325**, 178 (2009), <https://www.science.org/doi/pdf/10.1126/science.1173034>.
- [11] H. Zhang, C.-X. Liu, X.-L. Qi, X. Dai, Z. Fang, and S.-C. Zhang, *Nature Physics* **5**, 438 (2009), publisher: Nature Publishing Group.
- [12] W. A. Benalcazar, B. A. Bernevig, and T. L. Hughes, *Science* **357**, 61 (2017), publisher: American Association for the Advancement of Science.
- [13] F. Schindler, A. M. Cook, M. G. Vergniory, Z. Wang, S. S. P. Parkin, B. A. Bernevig, and T. Neupert, *Science Advances* **4**, eaat0346 (2018), publisher: American Association for the Advancement of Science.
- [14] Y. Ando, *Journal of the Physical Society of Japan* **82**, 102001 (2013), <https://doi.org/10.7566/JPSJ.82.102001>.
- [15] Y. Tokura, K. Yasuda, and A. Tsukazaki, *Nature Reviews Physics* **1**, 126 (2019).
- [16] M. Z. Hasan and J. E. Moore, *Annual Review of Condensed Matter Physics* **2**, 55 (2011).
- [17] L. Fu, C. L. Kane, and E. J. Mele, *Phys. Rev. Lett.* **98**, 106803 (2007).
- [18] L. Fu and C. L. Kane, *Phys. Rev. B* **76**, 045302 (2007).
- [19] S. Nadj-Perge, I. K. Drozdov, J. Li, H. Chen, S. Jeon, J. Seo, A. H. MacDonald, B. A. Bernevig, and A. Yazdani, *Science* **346**, 602 (2014), publisher: American Association for the Advancement of Science.
- [20] Y. W. Li, H. J. Zheng, Y. Q. Fang, D. Q. Zhang, Y. J. Chen, C. Chen, A. J. Liang, W. J. Shi, D. Pei, L. X. Xu, S. Liu, J. Pan, D. H. Lu, M. Hashimoto, A. Barinov, S. W. Jung, C. Cacho, M. X. Wang, Y. He, L. Fu, H. J. Zhang, F. Q. Huang, L. X. Yang, Z. K. Liu, and Y. L. Chen, *Nature Communications* **12**, 2874 (2021), publisher: Nature Publishing Group.
- [21] P. Zhang, K. Yaji, T. Hashimoto, Y. Ota, T. Kondo, K. Okazaki, Z. Wang, J. Wen, G. D. Gu, H. Ding, and S. Shin, *Science* **360**, 182 (2018), publisher: American Association for the Advancement of Science.
- [22] W. A. Benalcazar, B. A. Bernevig, and T. L. Hughes, *Physical Review B* **96**, 245115 (2017), publisher: American Physical Society.
- [23] B. A. Bernevig and S.-C. Zhang, *Physical Review Letters* **96**, 106802 (2006), publisher: American Physical Society.
- [24] M. G. Vergniory, L. Elcoro, C. Felser, N. Regnault, B. A. Bernevig, and Z. Wang, *Nature* **566**, 480 (2019), publisher:

Nature Publishing Group.

- [25] F. Schindler, Z. Wang, M. G. Vergniory, A. M. Cook, A. Murani, S. Sengupta, A. Y. Kasumov, R. Deblock, S. Jeon, I. Drozdov, H. Bouchiat, S. Guéron, A. Yazdani, B. A. Bernevig, and T. Neupert, *Nature Physics* **14**, 918 (2018), publisher: Nature Publishing Group.
- [26] R. Yu, W. Zhang, H.-J. Zhang, S.-C. Zhang, X. Dai, and Z. Fang, *Science* **329**, 61 (2010), publisher: American Association for the Advancement of Science.
- [27] A. A. Soluyanov, D. Gresch, Z. Wang, Q. Wu, M. Troyer, X. Dai, and B. A. Bernevig, *Nature* **527**, 495 (2015), publisher: Nature Publishing Group.
- [28] X. Wan, A. M. Turner, A. Vishwanath, and S. Y. Savrasov, *Physical Review B* **83**, 205101 (2011), publisher: American Physical Society.
- [29] B. Lv, H. Weng, B. Fu, X. Wang, H. Miao, J. Ma, P. Richard, X. Huang, L. Zhao, G. Chen, Z. Fang, X. Dai, T. Qian, and H. Ding, *Physical Review X* **5**, 031013 (2015), publisher: American Physical Society.
- [30] H. Weng, C. Fang, Z. Fang, B. A. Bernevig, and X. Dai, *Physical Review X* **5**, 011029 (2015), publisher: American Physical Society.
- [31] D. F. Liu, A. J. Liang, E. K. Liu, Q. N. Xu, Y. W. Li, C. Chen, D. Pei, W. J. Shi, S. K. Mo, P. Dudin, T. Kim, C. Cacho, G. Li, Y. Sun, L. X. Yang, Z. K. Liu, S. S. P. Parkin, C. Felser, and Y. L. Chen, *Science* **365**, 1282 (2019), publisher: American Association for the Advancement of Science.
- [32] B. Lv, T. Qian, and H. Ding, *Reviews of Modern Physics* **93**, 025002 (2021), publisher: American Physical Society.
- [33] N. Armitage, E. Mele, and A. Vishwanath, *Reviews of Modern Physics* **90**, 015001 (2018).
- [34] Z. Wang, Y. Sun, X.-Q. Chen, C. Franchini, G. Xu, H. Weng, X. Dai, and Z. Fang, *Physical Review B* **85**, 195320 (2012), publisher: American Physical Society.
- [35] Z. K. Liu, B. Zhou, Y. Zhang, Z. J. Wang, H. M. Weng, D. Prabhakaran, S.-K. Mo, Z. X. Shen, Z. Fang, X. Dai, Z. Hussain, and Y. L. Chen, *Science* **343**, 864 (2014), publisher: American Association for the Advancement of Science.
- [36] B. Bradlyn, J. Cano, Z. Wang, M. G. Vergniory, C. Felser, R. J. Cava, and B. A. Bernevig, *Science* **353**, aaf5037 (2016), publisher: American Association for the Advancement of Science.
- [37] Z. K. Liu, J. Jiang, B. Zhou, Z. J. Wang, Y. Zhang, H. M. Weng, D. Prabhakaran, S.-K. Mo, H. Peng, P. Dudin, T. Kim, M. Hoesch, Z. Fang, X. Dai, Z. X. Shen, D. L. Feng, Z. Hussain, and Y. L. Chen, *Nature Materials* **13**, 677 (2014), publisher: Nature Publishing Group.
- [38] X. Huang, L. Zhao, Y. Long, P. Wang, D. Chen, Z. Yang, H. Liang, M. Xue, H. Weng, Z. Fang, X. Dai, and G. Chen, *Physical Review X* **5**, 031023 (2015), publisher: American Physical Society.
- [39] Z. Wang, H. Weng, Q. Wu, X. Dai, and Z. Fang, *Physical Review B* **88**, 125427 (2013), publisher: American Physical Society.
- [40] S. M. Young, S. Zaheer, J. C. Y. Teo, C. L. Kane, E. J. Mele, and A. M. Rappe, *Phys. Rev. Lett.* **108**, 140405 (2012).
- [41] S. M. Young and C. L. Kane, *Phys. Rev. Lett.* **115**, 126803 (2015).
- [42] S. Borisenko, Q. Gibson, D. Evtushinsky, V. Zabolotnyy, B. Büchner, and R. J. Cava, *Phys. Rev. Lett.* **113**, 027603 (2014).
- [43] J. Xiong, S. K. Kushwaha, T. Liang, J. W. Krizan, M. Hirschberger, W. Wang, R. J. Cava, and N. P. Ong, *Science* **350**, 413 (2015).
- [44] B. J. Wieder, Y. Kim, A. M. Rappe, and C. L. Kane, *Phys. Rev. Lett.* **116**, 186402 (2016).
- [45] M. Neupane, S.-Y. Xu, R. Sankar, N. Alidoust, G. Bian, C. Liu, I. Belopolski, T.-R. Chang, H.-T. Jeng, H. Lin, A. Bansil, F. Chou, and M. Z. Hasan, *Nature Communications* **5**, 3786 (2014).
- [46] B. Yan and C. Felser, *Annual Review of Condensed Matter Physics* **8**, 337 (2017).
- [47] A. A. Burkov and L. Balents, *Phys. Rev. Lett.* **107**, 127205 (2011).
- [48] L. X. Yang, Z. K. Liu, Y. Sun, H. Peng, H. F. Yang, T. Zhang, B. Zhou, Y. Zhang, Y. F. Guo, M. Rahn, D. Prabhakaran, Z. Hussain, S.-K. Mo, C. Felser, B. Yan, and Y. L. Chen, *Nature Physics* **11**, 728 (2015).
- [49] M. Dzero, J. Xia, V. Galitski, and P. Coleman, *Annual Review of Condensed Matter Physics* **7**, 249 (2016), publisher: Annual Reviews.
- [50] M. Dzero, K. Sun, P. Coleman, and V. Galitski, *Physical Review B* **85**, 045130 (2012), publisher: American Physical Society.
- [51] V. Alexandrov, M. Dzero, and P. Coleman, *Physical Review Letters* **111**, 226403 (2013), publisher: American Physical Society.
- [52] J. Knolle and N. R. Cooper, *Physical Review Letters* **118**, 096604 (2017), publisher: American Physical Society.
- [53] B. Roy, J. D. Sau, M. Dzero, and V. Galitski, *Physical Review B* **90**, 155314 (2014), publisher: American Physical Society.
- [54] P. Syers, D. Kim, M. S. Fuhrer, and J. Paglione, *Physical Review Letters* **114**, 096601 (2015), publisher: American Physical Society.
- [55] N. Xu, X. Shi, P. K. Biswas, C. E. Matt, R. S. Dhaka, Y. Huang, N. C. Plumb, M. Radović, J. H. Dil, E. Pomjakushina, K. Conder, A. Amato, Z. Salman, D. M. Paul, J. Mesot, H. Ding, and M. Shi, *Physical Review B* **88**, 121102 (2013), publisher: American Physical Society.
- [56] M.-T. Tran, T. Takimoto, and K.-S. Kim, *Physical Review B* **85**, 125128 (2012), publisher: American Physical Society.
- [57] H. Pirie, Y. Liu, A. Soumyanarayanan, P. Chen, Y. He, M. M. Yee, P. F. S. Rosa, J. D. Thompson, D.-J. Kim, Z. Fisk, X. Wang, J. Paglione, D. K. Morr, M. H. Hamidian, and J. E. Hoffman, *Nature Physics* **16**, 52 (2020), publisher: Nature Publishing Group.
- [58] N. Xu, P. K. Biswas, J. H. Dil, R. S. Dhaka, G. Landolt, S. Muff, C. E. Matt, X. Shi, N. C. Plumb, M. Radović, E. Pomjakushina, K. Conder, A. Amato, S. V. Borisenko, R. Yu, H.-M. Weng, Z. Fang, X. Dai, J. Mesot, H. Ding, and M. Shi, *Nature Communications* **5**, 4566 (2014), publisher: Nature Publishing Group.
- [59] M. Neupane, N. Alidoust, S.-Y. Xu, T. Kondo, Y. Ishida, D. J. Kim, C. Liu, I. Belopolski, Y. J. Jo, T.-R. Chang, H.-T. Jeng, T. Durakiewicz, L. Balicas, H. Lin, A. Bansil, S. Shin, Z. Fisk, and M. Z. Hasan, *Nature Communications* **4**, 2991 (2013), publisher: Nature Publishing Group.
- [60] Y. Nakajima, P. Syers, X. Wang, R. Wang, and J. Paglione, *Nature Physics* **12**, 213 (2016), publisher: Nature Publishing Group.
- [61] V. Alexandrov, P. Coleman, and O. Erten, *Physical Review Letters* **114**, 177202 (2015), publisher: American Physical Society.
- [62] A. Kofuji, Y. Michishita, and R. Peters, *Physical Review B* **104**, 085151 (2021), publisher: American Physical Society.
- [63] S. Dzsaber, X. Yan, M. Taupin, G. Eguchi, A. Prokofiev, T. Shiroka, P. Blaha, O. Rubel, S. E. Grefe, H.-H. Lai, Q. Si, and S. Paschen, *Proceedings of the National Academy of Sciences* **118**, 21071 (2021), publisher: National Academy of Sciences.

- ences **118**, e2013386118 (2021), publisher: Proceedings of the National Academy of Sciences.
- [64] S. E. Grefe, H.-H. Lai, S. Paschen, and Q. Si, *Physical Review B* **101**, 075138 (2020), publisher: American Physical Society.
- [65] H.-H. Lai, S. E. Grefe, S. Paschen, and Q. Si, *Proceedings of the National Academy of Sciences* **115**, 93 (2018), publisher: Proceedings of the National Academy of Sciences.
- [66] L. Chen, C. Setty, H. Hu, M. G. Vergniory, S. E. Grefe, L. Fischer, X. Yan, G. Eguchi, A. Prokofiev, S. Paschen, J. Cano, and Q. Si, *Nature Physics* **18**, 1341 (2022), publisher: Nature Publishing Group.
- [67] Q. Y. Chen, X. B. Luo, D. H. Xie, M. L. Li, X. Y. Ji, R. Zhou, Y. B. Huang, W. Zhang, W. Feng, Y. Zhang, L. Huang, Q. Q. Hao, Q. Liu, X. G. Zhu, Y. Liu, P. Zhang, X. C. Lai, Q. Si, and S. Y. Tan, *Phys. Rev. Lett.* **123**, 106402 (2019).
- [68] X. Ji, X. Luo, Q. Chen, W. Feng, Q. Hao, Q. Liu, Y. Zhang, Y. Liu, X. Wang, S. Tan, and X. Lai, *Phys. Rev. B* **106**, 125120 (2022).
- [69] P. Li, H. Ye, Y. Hu, Y. Fang, Z. Xiao, Z. Wu, Z. Shan, R. P. Singh, G. Balakrishnan, D. Shen, Y.-f. Yang, C. Cao, N. C. Plumb, M. Smidman, M. Shi, J. Kroha, H. Yuan, F. Steglich, and Y. Liu, *Phys. Rev. B* **107**, L201104 (2023).
- [70] S.-K. Zhang, Z.-Y. Zeng, Y.-J. Xu, X.-R. Chen, and G.-F. Ji, *Phys. Rev. B* **107**, 195440 (2023).
- [71] A. Mielke, *Journal of Physics A: Mathematical and General* **24**, 3311 (1991).
- [72] H. Tasaki, *Physical Review Letters* **69**, 1608 (1992), publisher: American Physical Society.
- [73] B. Lian, Z.-D. Song, N. Regnault, D. K. Efetov, A. Yazdani, and B. A. Bernevig, *Physical Review B* **103**, 205414 (2021).
- [74] A. Auerbach, *Interacting electrons and quantum magnetism* (Springer Science & Business Media, 2012).
- [75] Y. Tian, Y. Kong, K. Liu, A. Zhang, R. He, and Q. Zhang, *Physica B: Condensed Matter* **512**, 75 (2017).
- [76] P. Coleman, *Introduction to many-body physics* (Cambridge University Press, 2015).
- [77] P. Coleman, *Phys. Rev. B* **35**, 5072 (1987).
- [78] J. R. Schrieffer and P. A. Wolff, *Phys. Rev.* **149**, 491 (1966).
- [79] G. Kotliar, S. Y. Savrasov, K. Haule, V. S. Oudovenko, O. Parcollet, and C. A. Marianetti, *Rev. Mod. Phys.* **78**, 865 (2006).
- [80] A. Georges, G. Kotliar, W. Krauth, and M. J. Rozenberg, *Rev. Mod. Phys.* **68**, 13 (1996).
- [81] K. Haule and T. Birol, *Phys. Rev. Lett.* **115**, 256402 (2015).
- [82] K. Haule, *Phys. Rev. Lett.* **115**, 196403 (2015).
- [83] C. Fang, Y. Chen, H.-Y. Kee, and L. Fu, *Physical Review B* **92**, 081201 (2015), publisher: American Physical Society.
- [84] C. Fang, H. Weng, X. Dai, and Z. Fang, *Chinese Physics B* **25**, 117106 (2016), publisher: IOP Publishing.
- [85] R. Yu, Z. Fang, X. Dai, and H. Weng, *Frontiers of Physics* **12**, 127202 (2017).
- [86] Y. Xu, L. Elcoro, Z.-D. Song, M. Vergniory, C. Felser, S. S. Parkin, N. Regnault, J. L. Mañes, and B. A. Bernevig, *Physical Review B* **109**, 165139 (2024).
- [87] Y. Xu, L. Elcoro, G. Li, Z.-D. Song, N. Regnault, Q. Yang, Y. Sun, S. Parkin, C. Felser, and B. A. Bernevig, arXiv preprint arXiv:2111.02433 (2021).
- [88] Z.-D. Song, L. Elcoro, and B. A. Bernevig, *Science* **367**, 794 (2020).
- [89] W. A. Benalcazar, B. A. Bernevig, and T. L. Hughes, *Science* **357**, 61 (2017).
- [90] Z. Song, Z. Fang, and C. Fang, *Physical review letters* **119**, 246402 (2017).
- [91] L. Elcoro, B. Bradlyn, Z. Wang, M. G. Vergniory, J. Cano, C. Felser, B. A. Bernevig, D. Orobengoa, G. de la Flor, and M. I. Aroyo, *J. Appl. Cryst.* **50**, 1457 (2017).
- [92] M. G. Vergniory, L. Elcoro, Z. Wang, J. Cano, C. Felser, M. I. Aroyo, B. A. Bernevig, and B. Bradlyn, *Phys. Rev. E* **96**, 023310 (2017).
- [93] G. Kresse and J. Furthmüller, *Computational materials science* **6**, 15 (1996).
- [94] G. Kresse and J. Hafner, *Physical Review B* **48**, 13115 (1993).
- [95] G. Kresse and J. Hafner, *Physical review B* **47**, 558 (1993).
- [96] G. Kresse and J. Hafner, *Physical Review B* **49**, 14251 (1994).
- [97] G. Kresse and J. Furthmüller, *Physical review B* **54**, 11169 (1996).
- [98] J. P. Perdew, K. Burke, and M. Ernzerhof, *Physical review letters* **77**, 3865 (1996).
- [99] N. Marzari and D. Vanderbilt, *Physical review B* **56**, 12847 (1997).
- [100] I. Souza, N. Marzari, and D. Vanderbilt, *Physical Review B* **65**, 035109 (2001).
- [101] N. Marzari, A. A. Mostofi, J. R. Yates, I. Souza, and D. Vanderbilt, *Reviews of Modern Physics* **84**, 1419 (2012).
- [102] G. Pizzi, V. Vitale, R. Arita, S. Blügel, F. Freimuth, G. Géranton, M. Gibertini, D. Gresch, C. Johnson, T. Koretsune, *et al.*, *Journal of Physics: Condensed Matter* **32**, 165902 (2020).
- [103] Q. Wu, S. Zhang, H.-F. Song, M. Troyer, and A. A. Soluyanov, *Computer Physics Communications* **224**, 405 (2018).
- [104] J. Gao, Q. Wu, C. Persson, and Z. Wang, *Computer Physics Communications* **261**, 107760 (2021).
- [105] Z. Zhang, Z.-M. Yu, G.-B. Liu, and Y. Yao, *Computer Physics Communications* **270**, 108153 (2022).
- [106] Y. Jiang, H. Hu, D. Călugăru, C. Felser, S. Blanco-Canosa, H. Weng, Y. Xu, and B. A. Bernevig, *Kagome materials ii: Sg 191: Fege as a lego building block for the entire 1:6:6 series: hidden d-orbital decoupling of flat band sectors, effective models and interaction hamiltonians* (2023), arXiv:2311.09290 [cond-mat.str-el].
- [107] J. Herzog-Arbeitman, A. Chew, K.-E. Huhtinen, P. Törmä, and B. A. Bernevig, *Many-body superconductivity in topological flat bands* (2022), arXiv:2209.00007 [cond-mat.str-el].
- [108] H. Hu and B. A. Bernevig, to appear.
- [109] F. Aryasetiawan, M. Imada, A. Georges, G. Kotliar, S. Biermann, and A. I. Lichtenstein, *Phys. Rev. B* **70**, 195104 (2004).
- [110] F. Aryasetiawan, K. Karlsson, O. Jepsen, and U. Schönberger, *Physical Review B* **74**, 125106 (2006).
- [111] T. Miyake, F. Aryasetiawan, and M. Imada, *Physical Review B* **80**, 155134 (2009).
- [112] H. Hu, B. A. Bernevig, and A. M. Tsvelik, *Phys. Rev. Lett.* **131**, 026502 (2023).
- [113] M. A. Ruderman and C. Kittel, *Phys. Rev.* **96**, 99 (1954).
- [114] T. Kasuya, *Progress of Theoretical Physics* **16**, 45 (1956), <https://academic.oup.com/ptp/article-pdf/16/1/45/5266722/16-1-45.pdf>.
- [115] K. Yosida, *Phys. Rev.* **106**, 893 (1957).
- [116] H. Hu, G. Rai, L. Crippa, J. Herzog-Arbeitman, D. Călugăru, T. Wehling, G. Sangiovanni, R. Valentí, A. M. Tsvelik, and B. A. Bernevig, *Phys. Rev. Lett.* **131**, 166501 (2023).
- [117] C. Petrovic, P. Pagliuso, M. F. Hundley, R. Movshovich, J. L. Sarrao, J. D. Thompson, Z. Fisk, and P. Monthoux, *Journal of Physics: Condensed Matter* **13**, L337 (2001).
- [118] S. Kirchner, S. Paschen, Q. Chen, S. Wirth, D. Feng, J. D. Thompson, and Q. Si, *Rev. Mod. Phys.* **92**, 011002 (2020).
- [119] M. Reehuis, W. Jeitschko, G. Kotzbya, B. Zimmer, and X. Hu, *Journal of alloys and compounds* **266**, 54 (1998).
- [120] M. Reehuis and W. Jeitschko, *Journal of Physics and Chemistry of Solids* **51**, 961 (1990).

- [121] Bilbao Crystallographic Server, <https://www.cryst.ehu.es/>.
- [122] B. Peng, Y. Jiang, Z. Fang, H. Weng, and C. Fang, *Physical Review B* **105**, 235138 (2022).
- [123] X.-L. Qi, T. L. Hughes, and S.-C. Zhang, *Physical Review B* **78**, 195424 (2008).
- [124] C. Fang, M. J. Gilbert, and B. A. Bernevig, *Physical Review B* **86**, 115112 (2012).
- [125] Y. Xu, L. Elcoro, Z.-D. Song, M. Vergniory, C. Felser, S. S. Parkin, N. Regnault, J. L. Mañes, and B. A. Bernevig, arXiv preprint arXiv:2106.10276 (2021).
- [126] Z. Wang, A. Alexandradinata, R. J. Cava, and B. A. Bernevig, *Nature* **532**, 189 (2016).
- [127] B. A. Bernevig, B. Lian, A. Cowsik, F. Xie, N. Regnault, and Z.-D. Song, *Phys. Rev. B* **103**, 205415 (2021).

Supplemental Material: A unique topological heavy-fermion system: CeCo_2P_2 with $P \cdot \mathcal{T}$ -protected Kondo effect and nodal-line excitations in the antiferromagnetic phase

CONTENTS

Acknowledgments	5
I. Experimental observations	11
II. Lattice structure	11
1. Primitive cell	11
2. Conventional cell	12
III. Model and Hamiltonian	13
IV. DFT calculation details	13
V. Relatively flat bands in the paramagnetic phase	14
VI. Antiferromagnetism of c electrons	17
1. Mean-field theory	18
2. Mean-field and DFT results of the AFM phase	19
VII. Magnetism of LaCo_2P_2	21
VIII. Atomic limit of f electron	24
1. Hubbard interactions and charge ± 1 excitation	25
2. Spin-orbit coupling	26
3. Crystal field splitting	26
IX. Kondo lattice model	27
1. Kondo coupling	27
2. Mean-field theory of Kondo phase	31
X. Kondo effect in the AFM phase	32
1. Filling-enforced metallic phase of the c electrons	33
2. $P \cdot \mathcal{T}$ symmetry and the Kondo effect in the AFM phase	33
3. Development of Kondo effect in the DFT model	35
4. Hybridization function	37
5. eDMFT calculations	39
XI. Band topology of the Kondo phase	39
1. Glide mirror- z symmetry	39
2. Nodal line in the Kondo phase	40
3. Irreducible representation of the Kondo bands	42
XII. Surface state	44
1. Symmetry properties	44
2. Effective model of nodal line	45
3. Surface states	47
XIII. Schrieffer-Wolff transformation	52
XIV. Flat-band ferromagnetism/anti-ferromagnetism	54
1. Ferromagnetism from 2D non-atomic flat band	54
a. Orthonormal basis	57
b. Charge ± 1 excitation state	59
2. z direction hopping and out-of-plane antiferromagnetism	63

a. Contribution from I	68
b. Contribution from II	68
c. Contribution from III	69
d. Contribution from IV	70
e. Effective spin-spin interaction terms	71

Appendix I: Experimental observations

In this section, we list the experimental observations of the CeCo_2P_2 [2].

- The system develops a type-A antiferromagnetic (AFM) order at $T_{\text{AFM}} \sim 450\text{K}$. The magnetic ordering comes from the electrons of Co. The magnetic structure has been shown in Fig. S4.
- From XPS and XAS measurement [2], Ce atoms have been found to behave as

$$\text{Ce}^{3+} : 4f^1 5d^0 5s^0 \quad (\text{S1.1})$$

In other words, there is one f electron per Ce atom. Therefore, f electron at Ce atom behaves as a local moment.

- Both resistivity and ARPES measurements suggest the development of the Kondo effect below $T \sim 100\text{K}$.
- At low temperatures (below the Kondo temperature), ARPES measurement identifies a nodal line at $k_z = 1/2$ planes.

In this work, we will provide a comprehensive understanding of the above experimental observations.

Appendix II: Lattice structure

1. Primitive cell

The paramagnetic (PM) phase (at $T > T_{\text{AFM}}$) has space group 139. The unit cell (primitive cell) of the paramagnetic phase has the following lattice vectors

$$\begin{aligned} \mathbf{a}_1 &= (-1.9475\text{\AA} \quad 1.9475\text{\AA} \quad 4.802\text{\AA}) \\ \mathbf{a}_2 &= (1.9475\text{\AA} \quad -1.9475\text{\AA} \quad 4.802\text{\AA}) \\ \mathbf{a}_3 &= (1.9475\text{\AA} \quad 1.9475\text{\AA} \quad -4.802\text{\AA}) \end{aligned} \quad (\text{S2.1})$$

The reciprocal lattice vectors are

$$\begin{aligned} \mathbf{b}_1 &= 2\pi(0 \quad 0.2567\text{\AA}^{-1} \quad 0.1041\text{\AA}^{-1}) \\ \mathbf{b}_2 &= 2\pi(0.2567\text{\AA}^{-1} \quad 0 \quad 0.1041\text{\AA}^{-1}) \\ \mathbf{b}_3 &= 2\pi(0.2567\text{\AA}^{-1} \quad 0.2567\text{\AA}^{-1} \quad 0) \end{aligned} \quad (\text{S2.2})$$

There are two Co atoms two P atoms and one Ce atom per unit cell located at

$$\begin{aligned} \text{Co} &: (3/4, 1/4, 1/2), \quad (1/4, 3/4, 1/2) \\ \text{Ce} &: (0, 0, 0) \\ \text{P} &: (0.628, 0.628, 0), \quad (0.372, 0.372, 0) \end{aligned} \quad (\text{S2.3})$$

The relevant orbitals we considered in this work are: (1) five d orbitals and seven f orbitals of Ce atoms; (2) five d orbitals of Co atoms; (3) three p orbitals of P atoms. The d orbitals, p orbitals, and f orbitals are

$$\begin{aligned} &d_{z^2}, d_{xz}, d_{yz}, d_{x^2-y^2}, d_{xy} \\ &p_z, p_x, p_y \\ &f_{z^3}, f_{xz^2}, f_{yz^2}, f_{z(x^2-y^2)}, f_{xyz}, f_{x(x^2-3y^2)}, f_{y(3x^2-y^2)} \end{aligned} \quad (\text{S2.4})$$

The high symmetry points of the primitive cell are

$$\Gamma = (0, 0, 0), \quad M = \left(\frac{-1}{2}, \frac{1}{2}, \frac{1}{2}\right), \quad X = \left(0, 0, \frac{1}{2}\right), \quad P = \left(\frac{1}{4}, \frac{1}{4}, \frac{1}{4}\right), \quad N = \left(0, \frac{1}{2}, 0\right) \quad (\text{S2.5})$$

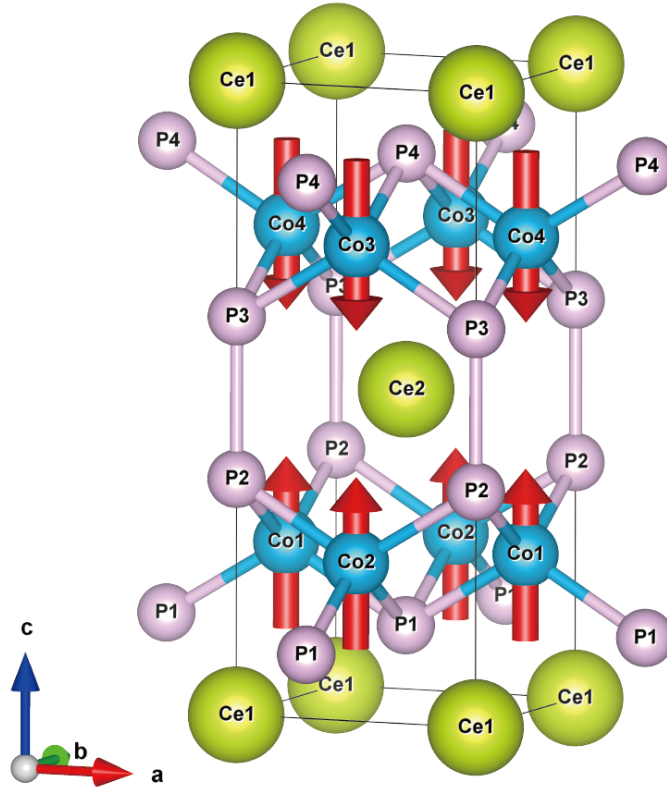


Figure S4. Lattice structures and magnetic structures.

2. Conventional cell

The system develops an AFM order below $T_{\text{AFM}} \approx 450\text{K}$. The AFM phase is described by the magnetic group 126.386 ($P14/nnc$). The unit cell of the AFM phase corresponds to the conventional cell of the PM phase. For future reference, we denote the unit cell of the AFM phase as the conventional cell, and the unit cell of the PM phase as the primitive cell.

The lattice vectors of the conventional cell are

$$\mathbf{A}_1 = \mathbf{a}_2 + \mathbf{a}_3, \quad \mathbf{A}_2 = \mathbf{a}_3 + \mathbf{a}_1, \quad \mathbf{A}_3 = \mathbf{a}_1 + \mathbf{a}_2 \quad (\text{S2.6})$$

The reciprocal lattice vectors of the conventional cell (\mathbf{B}_i) and primitive cell (\mathbf{b}_i) have the following relations

$$\mathbf{B}_1 = \frac{1}{2}(-\mathbf{b}_1 + \mathbf{b}_2 + \mathbf{b}_3), \quad \mathbf{B}_2 = \frac{1}{2}(\mathbf{b}_1 - \mathbf{b}_2 + \mathbf{b}_3), \quad \mathbf{B}_3 = \frac{1}{2}(\mathbf{b}_1 + \mathbf{b}_2 - \mathbf{b}_3) \quad (\text{S2.7})$$

In the conventional cell, the number of atoms is doubled. The atoms are located at (in the unit of $\mathbf{A}_1, \mathbf{A}_2, \mathbf{A}_3$)

$$\begin{aligned} \text{Co} &: \left(0, \frac{1}{2}, \frac{1}{4}\right), \left(\frac{1}{2}, 0, \frac{1}{4}\right), \left(\frac{1}{2}, 0, \frac{3}{4}\right), \left(0, \frac{1}{2}, \frac{3}{4}\right) \\ \text{Ce} &: (0, 0, 0), \left(\frac{1}{2}, \frac{1}{2}, \frac{1}{2}\right) \\ \text{P} &: \left(\frac{1}{2}, \frac{1}{2}, z\right), \left(0, 0, \frac{1}{2} - z\right), \left(0, 0, \frac{1}{2} + z\right), \left(\frac{1}{2}, \frac{1}{2}, 1 - z\right), \quad z = 0.128. \end{aligned} \quad (\text{S2.8})$$

The high symmetry points of the conventional cell are

$$\begin{aligned} \Gamma &= (0, 0, 0), \quad X = \left(0, \frac{1}{2}, 0\right), \quad M = \left(\frac{1}{2}, \frac{1}{2}, 0\right) \\ Z &= \left(0, 0, \frac{1}{2}\right), \quad R = \left(0, \frac{1}{2}, \frac{1}{2}\right), \quad A = \left(\frac{1}{2}, \frac{1}{2}, \frac{1}{2}\right) \end{aligned} \quad (\text{S2.9})$$

Appendix III: Model and Hamiltonian

The electrons in the system can be separated into the correlated f electrons and itinerant c electrons. The f electrons correspond to the f orbitals of Ce. The c electrons correspond to the d orbitals of Ce, d orbitals of Co, and p orbitals of P. We use $f_{\mathbf{R},a,i,\sigma}$ and $c_{\mathbf{R},a,i,\sigma}$ to describe the f electrons and c electrons respectively, where \mathbf{R} is the position of the unit cell, a is the sublattice index, i is the orbital index and σ is the spin index. We will clarify in each section whether a conventional cell or a primitive cell is being used. The Hamiltonian takes the form of a periodic Anderson model

$$H = H_c + H_V + H_{c,U} + H_f. \quad (\text{S3.1})$$

H_c describes the hopping of c electrons

$$H_c = \sum_{\mathbf{k},ab,ij,\sigma} \epsilon_{\mathbf{k},ab,ij} c_{\mathbf{k},a,i,\sigma}^\dagger c_{\mathbf{k},b,j,\sigma}. \quad (\text{S3.2})$$

H_V describes the hybridization between f and c electrons

$$H_V = \sum_{\mathbf{R},\Delta\mathbf{R},ab,ij,\sigma} V_{ab,ij}^c(\Delta\mathbf{R}) f_{\mathbf{R},a,i,\sigma}^\dagger c_{\mathbf{R}+\Delta\mathbf{R},b,j,\sigma} + \text{h.c.} \quad (\text{S3.3})$$

$H_{c,U}$ denotes the on-site interactions of c electrons, which takes the form of multi-orbital Hubbard interactions

$$\begin{aligned} H_{c,U} = & \frac{1}{2} \sum_{\mathbf{R},a,(i,\sigma) \neq (j,\sigma')} U_{ij,a} : c_{\mathbf{R},a,i,\sigma}^\dagger c_{\mathbf{R},a,i,\sigma} c_{\mathbf{R},a,j,\sigma'}^\dagger c_{\mathbf{R},a,j,\sigma'} : \\ & - \frac{1}{2} \sum_{\mathbf{R},a,i,j,\sigma,\sigma'} J_{ij,a} : c_{\mathbf{R},a,i,\sigma}^\dagger c_{\mathbf{R},a,i,\sigma} c_{\mathbf{R},a,j,\sigma'}^\dagger c_{\mathbf{R},a,j,\sigma'} : + \frac{1}{2} \sum_{\mathbf{R},a,i,j,\sigma,\sigma'} J_{ij,a} : c_{\mathbf{R},a,i,\sigma}^\dagger c_{\mathbf{R},a,i,\sigma} c_{\mathbf{R},a,j,\sigma'}^\dagger c_{\mathbf{R},a,j,\sigma'} : \end{aligned} \quad (\text{S3.4})$$

where $U_{ij,a}$ are the density-density interactions and $J_{ij,a}$ are the Hund's couplings. The values of these interactions will be derived from DFT calculations. For a given operator O , we have defined the normal ordering of the operator as $: O :$.

H_f describes all the on-site coupling terms of f electrons, including the crystal-field splittings, spin-orbital couplings, and Hubbard repulsion. It takes the form of

$$H_f = \sum_{\mathbf{R},a} H_{loc}[f_{\mathbf{R},a}^\dagger, f_{\mathbf{R},a}] \quad (\text{S3.5})$$

where $H_{loc}[f^\dagger, f]$ describes the local Hamiltonian of f electrons. $H_{loc}[f^\dagger, f]$ can be decomposed into three parts, the Hubbard interactions, crystal field splitting, and spin-orbit coupling (SOC)

$$\begin{aligned} H_{loc}[f^\dagger, f] &= H_U[f^\dagger, f] + H_{CEF}[f^\dagger, f] + H_{soc}[f^\dagger, f] \\ H_U[f^\dagger, f] &= \frac{U}{2} \left(\sum_{i,\sigma} f_{i,\sigma}^\dagger f_{i,\sigma} - n_0 \right)^2 \\ H_{CEF}[f^\dagger, f] &= \sum_{ij} \epsilon_{f,ij} f_{i,\sigma}^\dagger f_{j,\sigma} \\ H_{soc}[f, f^\dagger] &= \lambda \sum_{\mu} L^\mu S^\mu \end{aligned} \quad (\text{S3.6})$$

Here, since there is only one electron in the f shell of Ce, we take $n_0 = 1$. In the limit of large U , the filling of f electrons will be fixed to be $n_0 = 1$. $\epsilon_{f,ij}$ describes crystal field splitting of f electrons. λ is the strength of spin-orbit coupling where L^μ, S^μ the angular-momentum and spin operators of f electrons respectively.

Appendix IV: DFT calculation details

We use the Vienna ab-initio Simulation Package (VASP)[93–97] to perform the *ab-initio* calculations in this work, where the generalized gradient approximation of Perdew-Burke-Ernzerhof (PBE) exchange-correlation potential[98] is adopted. An $11 \times 11 \times 11$ uniform k -mesh and an energy cutoff of 400 eV are used for self-consistency computations. The maximally localized Wannier functions are obtained using WANNIER90[99–102]. The Wannier TB models are symmetrized using *Wannhr_symm* in *WannierTools*[103]. The irreducible representations are computed using *IR2TB*[104]. The minimal TB model is built with *MagneticTB*[105].

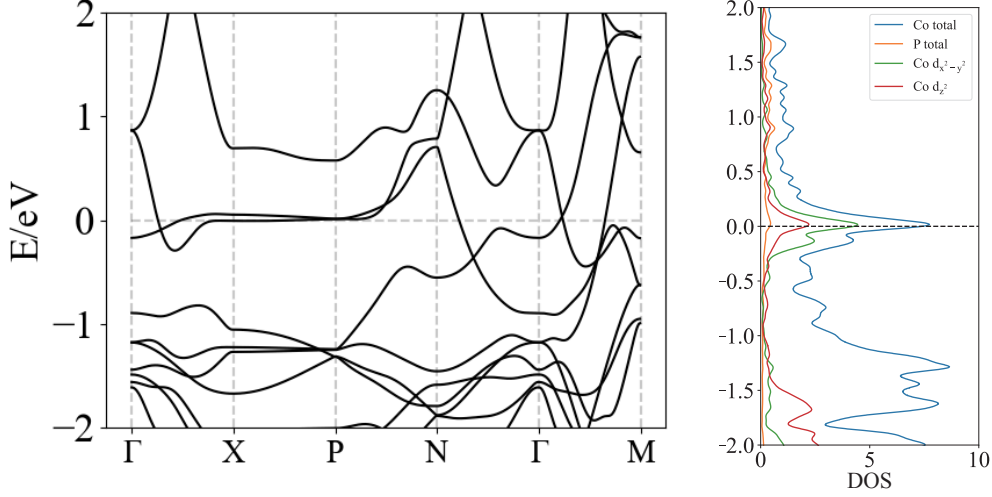


Figure S5. DFT-calculated band structure and density of states (DOS) of PM phase where f electrons have been treated as core states.

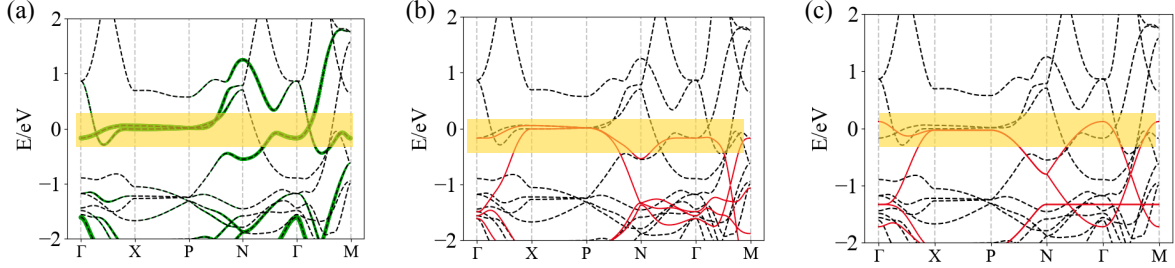


Figure S6. (a) DFT band structure. The green dots mark the orbital weights of the $d_{x^2-y^2}$, d_{z^2} orbitals of Co. Yellow areas mark the relative flat band. (b) Comparison between DFT band structures (black dashed lines) and the band structures obtained from two-orbital models (red solid lines). (c) Comparison between the DFT band structure (black dashed lines) and the band structure obtained from the simplified two-orbital model (red solid lines) given in Eq. S5.1.

Appendix V: Relatively flat bands in the paramagnetic phase

We discuss the band structure of the high-temperature paramagnetic phase. In this phase, due to the absence of the Kondo effect and large Hubbard interactions, f electrons will not contribute to the low-energy single-particle excitation. The band structures are described by only c electrons. We therefore obtain the band structures by treating f electron as core states (fully occupied f shell) and performing DFT calculations.

In Fig. S5, we show the band structures and the density of states (DOS) obtained from DFT calculations. We can observe an enhanced DOS peak appearing near the Fermi energy coming from the relatively flat band near the Fermi energy. This flat band is mostly formed by the $d_{x^2-y^2}$, d_{z^2} orbitals of Co.

We introduce the following three types of tight-binding models to model the relatively flat band in the PM phase (see Fig. S6 for the comparison between different models):

- **DFT model:** tight-binding model of PM phase obtained from DFT calculations (see Fig. S5 and Fig. S6 (a) for band structure).
- **Two-orbital model:** tight-binding model obtained by only including the hoppings of $d_{x^2-y^2}@Co$, $d_{z^2}@Co$ orbitals of DFT model (see Fig. S6 (b) for band structure).
- **Simplified two-orbital model:** the nearest-neighbor tight-binding model obtained by only keeping the dominant nearest-neighbor hopping of the two-orbital model (see Fig. S6 (c) for band structure).

We now discuss each model. In the DFT model, the enhanced DOS comes from $d_{x^2-y^2}$ and d_{z^2} orbitals of Co (Fig. S5, Fig. S6 (a)). This indicates the relatively flat band can be approximately described by a model that only contains $d_{x^2-y^2}$, d_{z^2}

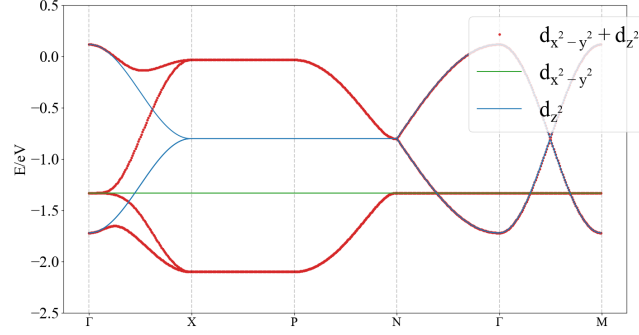


Figure S7. The band structure of the simplified two-orbital model is shown in red. The green and blue lines represent the band structures of the $d_{x^2-y^2}$ and d_{z^2} orbitals, respectively, in the absence of hybridization between these orbitals ($t_2 = 0$).

orbitals of Co atoms. Thus, we build a two-orbital model by only keeping the hopping of these two orbitals in the DFT model. The resulting band structure gives a good description of the flat band near Fermi energy as shown in Fig. S6 (b).

To understand the origin of the flat band, we find the two-orbital model can be further simplified into the following tight-binding model by only keeping the dominant nearest-neighbor hopping

$$\begin{aligned}
 H_c &= \sum_{\mathbf{k}, \sigma} \psi_{\mathbf{k}, \sigma}^\dagger h_{\mathbf{k}} \psi_{\mathbf{k}, \sigma} \\
 \psi_{\mathbf{k}} &= [c_{\mathbf{k}, Co1, z^2, \sigma} \quad c_{\mathbf{k}, Co2, z^2, \sigma} \quad c_{\mathbf{k}, Co1, x^2-y^2, \sigma} \quad c_{\mathbf{k}, Co2, x^2-y^2, \sigma}] \\
 h_{\mathbf{k}} &= \begin{bmatrix} \epsilon_1 & 0 & 0 & -4t_2 \sin\left(\frac{k_1+k_3}{2}\right) \sin\left(\frac{k_2+k_3}{2}\right) \\ 0 & \epsilon_1 & -4t_2 \sin\left(\frac{k_1+k_3}{2}\right) \sin\left(\frac{k_2+k_3}{2}\right) & 0 \\ 0 & -4t_2 \sin\left(\frac{k_1+k_3}{2}\right) \sin\left(\frac{k_2+k_3}{2}\right) & 0 & 0 \\ -4t_2 \sin\left(\frac{k_1+k_3}{2}\right) \sin\left(\frac{k_2+k_3}{2}\right) & 0 & 0 & 0 \end{bmatrix} \\
 g_{\mathbf{k}} &= 4t_1 \cos\left(\frac{k_1+k_3}{2}\right) \cos\left(\frac{k_2+k_3}{2}\right)
 \end{aligned} \tag{S5.1}$$

where the parameters are

$$\begin{aligned}
 \epsilon_1 &= -1.33eV, & \epsilon_2 &= -0.8eV \\
 t_2 &= -0.25eV, & t_1 &= -0.23eV
 \end{aligned} \tag{S5.2}$$

t_1 denotes the nearest-neighbor (in-plane) hopping between $d_{x^2-y^2}$ orbitals. t_2 denotes the nearest-neighbor (in-plane) hopping between $d_{x^2-y^2}$ and d_{z^2} orbitals. ϵ_1, ϵ_2 are the on-site energies of $d_{z^2}, d_{x^2-y^2}$ orbitals respectively. The nearest-neighbor hopping of d_{z^2} orbitals is relatively weak and has been dropped. We observe that the amplitudes of the d_{z^2} Wannier orbital are primarily concentrated along the z -axis, resulting in weak in-plane hopping of the d_{z^2} orbital. Furthermore, due to the large separation between Co atoms in different layers, the hopping along the z -direction is also relatively weak and has been neglected. The band structure of the simplified two-orbital model is given in Fig. S6 (c).

We now diagonalize the non-interacting Hamiltonian S5.1. We first introduce the following new basis,

$$\begin{bmatrix} \tilde{c}_{\mathbf{k}, 1, x^2-y^2, \sigma} \\ \tilde{c}_{\mathbf{k}, 2, x^2-y^2, \sigma} \\ \tilde{c}_{\mathbf{k}, 1, z^2, \sigma} \\ \tilde{c}_{\mathbf{k}, 2, z^2, \sigma} \end{bmatrix} = \frac{1}{\sqrt{2}} \begin{bmatrix} 1 & g_{\mathbf{k}}/|g_{\mathbf{k}}| & 0 & 0 \\ 1 & -g_{\mathbf{k}}/|g_{\mathbf{k}}| & 0 & 0 \\ 0 & 0 & 1 & g_{\mathbf{k}}/|g_{\mathbf{k}}| \\ 0 & 0 & 1 & -g_{\mathbf{k}}/|g_{\mathbf{k}}| \end{bmatrix} \begin{bmatrix} c_{\mathbf{k}, Co1, x^2-y^2, \sigma} \\ c_{\mathbf{k}, Co2, x^2-y^2, \sigma} \\ c_{\mathbf{k}, Co1, z^2, \sigma} \\ c_{\mathbf{k}, Co2, z^2, \sigma} \end{bmatrix} \tag{S5.3}$$

where $g_{\mathbf{k}} = g_{\mathbf{k}}^*$, and $g_{\mathbf{k}}/|g_{\mathbf{k}}| = \text{sign}(g_{\mathbf{k}})$. In the new basis, the Hamiltonians of $d_{x^2-y^2}$ block and d_{z^2} block have been diagonalized. There is still a coupling between the two orbitals. The new Hamiltonian becomes

$$\begin{aligned}
 H_c &= \sum_{\mathbf{k}, \sigma} \left[\epsilon_2 + |g_{\mathbf{k}}| \right] \tilde{c}_{\mathbf{k}, 1, x^2-y^2, \sigma}^\dagger \tilde{c}_{\mathbf{k}, 1, x^2-y^2, \sigma} + \left[\epsilon_2 - |g_{\mathbf{k}}| \right] \tilde{c}_{\mathbf{k}, 2, x^2-y^2, \sigma}^\dagger \tilde{c}_{\mathbf{k}, 2, x^2-y^2, \sigma} + \sum_{\mathbf{k}, i, \sigma} \epsilon_1 \tilde{c}_{\mathbf{k}, i, z^2, \sigma}^\dagger \tilde{c}_{\mathbf{k}, i, z^2, \sigma} \\
 &+ \sum_{\mathbf{k}, \sigma} \left\{ 4t_2 \sin\left(\frac{k_1+k_3}{2}\right) \sin\left(\frac{k_2+k_3}{2}\right) \left[\tilde{c}_{\mathbf{k}, 1, z^2, \sigma}^\dagger \quad \tilde{c}_{\mathbf{k}, 2, z^2, \sigma}^\dagger \right] \begin{bmatrix} -g_{\mathbf{k}}/|g_{\mathbf{k}}| & 0 \\ 0 & g_{\mathbf{k}}/|g_{\mathbf{k}}| \end{bmatrix} \begin{bmatrix} \tilde{c}_{\mathbf{k}, 1, x^2-y^2, \sigma} \\ \tilde{c}_{\mathbf{k}, 2, x^2-y^2, \sigma} \end{bmatrix} + \text{h.c.} \right\}
 \end{aligned} \tag{S5.4}$$

We first consider the case of $t_2 = 0$, where the hybridization between $d_{x^2-y^2}$ orbitals and d_{z^2} orbitals vanishes. In this case, $d_{x^2-y^2}$ orbitals have a relatively large dispersion due to the nearest-neighbor hopping t_1 , and d_{z^2} produces atomic flat bands (but far away from Fermi energy at ϵ_1) as shown in Fig. S7. We now show that, after turning on the hybridization, the hybridization term produces a relatively flat band (Fig. S7).

The hybridization term t_2 introduces coupling between $\tilde{c}_{\mathbf{k},1,x^2-y^2,\sigma}$ and $\tilde{c}_{\mathbf{k},1,z^2,\sigma}$, and coupling between $\tilde{c}_{\mathbf{k},2,x^2-y^2,\sigma}$ and $\tilde{c}_{\mathbf{k},2,z^2,\sigma}$. Since, $\tilde{c}_{\mathbf{k},1,x^2-y^2,\sigma}$ is more close to the Fermi energy at $t_2 = 0$ limit, we focus on the $(\tilde{c}_{\mathbf{k},1,x^2-y^2,\sigma}, \tilde{c}_{\mathbf{k},1,z^2,\sigma})$ sector. The corresponding Hamiltonian can be written as (from Eq. S5.4)

$$\begin{aligned} H'_c &= \sum_{\mathbf{k},\sigma} \begin{bmatrix} \tilde{c}_{\mathbf{k},1,x^2-y^2,\sigma}^\dagger & \tilde{c}_{\mathbf{k},1,z^2,\sigma}^\dagger \end{bmatrix} \begin{bmatrix} \Delta + \epsilon_{\mathbf{k}} & v_{\mathbf{k}} \\ v_{\mathbf{k}} & \epsilon_1 \end{bmatrix} \begin{bmatrix} \tilde{c}_{\mathbf{k},1,x^2-y^2,\sigma} \\ \tilde{c}_{\mathbf{k},1,z^2,\sigma} \end{bmatrix} \\ v_{\mathbf{k}} &= -4t_2 \sin\left(\frac{k_1 + k_3}{2}\right) \sin\left(\frac{k_2 + k_3}{2}\right) \frac{g_{\mathbf{k}}}{|g_{\mathbf{k}}|} \\ \Delta &= \epsilon_2 + \text{mean}_{\mathbf{k} \in BZ} |g_{\mathbf{k}}| \approx -0.34eV \\ \epsilon_{\mathbf{k}} &= |g_{\mathbf{k}}| - \text{mean}_{\mathbf{k} \in BZ} |g_{\mathbf{k}}| \end{aligned} \quad (\text{S5.5})$$

where we have subtracted the mean value of $|g_{\mathbf{k}}|$, such that we can separate the dispersion of $\tilde{c}_{\mathbf{k},1,x^2-y^2,\sigma}$ orbitals into a constant part Δ and a dispersive part $\epsilon_{\mathbf{k}}$ (with $\text{mean}_{\mathbf{k} \in BZ} \epsilon_{\mathbf{k}} = 0$). The dispersions of Hamiltonian shown in Eq. S5.5 are

$$E_{1/2,\mathbf{k}} = \frac{\epsilon_1 + \Delta + \epsilon_{\mathbf{k}}}{2} \pm \sqrt{\left(\frac{\epsilon_1 - \Delta - \epsilon_{\mathbf{k}}}{2}\right)^2 + v_{\mathbf{k}}^2} \quad (\text{S5.6})$$

We then show that, the upper band with dispersion $E_{1,\mathbf{k}}$ gives a relatively flat band. We notice that $\max \epsilon_{\mathbf{k}} - \min \epsilon_{\mathbf{k}} = 0.9eV$, $\max |v_{\mathbf{k}}| - \min |v_{\mathbf{k}}| = 1.0eV$, $\epsilon_1 - \Delta = 1.7$. We therefore perform an expansion by treating $\epsilon_{\mathbf{k}}, v_{\mathbf{k}}$ as small parameters and find

$$E_{1,\mathbf{k}} \approx \Delta + \epsilon_{\mathbf{k}} + \frac{v_{\mathbf{k}}^2}{|\Delta - \epsilon_1|} \quad (\text{S5.7})$$

$\epsilon_{\mathbf{k}}$ describes the original dispersions of $d_{x^2-y^2}$ orbitals (see Eq. S5.5), and $\frac{v_{\mathbf{k}}^2}{|\Delta - \epsilon_1|}$ denotes the contribution from the $d_{x^2-y^2}-d_{z^2}$ hybridization term. We now show that, by combining the contribution of two terms, we could generate a relatively flat band. We check the dispersion at high symmetry points

$$\begin{aligned} E_{1,\Gamma=(0,0,0)} &\approx \epsilon_2 + 4|t_1| \\ E_{1,M=(\frac{1}{2},\frac{1}{2},-\frac{1}{2})} &\approx \epsilon_2 + 4|t_1| \\ E_{1,X=(0,0,\frac{1}{2})} &\approx \epsilon_2 + \frac{16t_2^2}{|\Delta - \epsilon_1|} \\ E_{1,P=(\frac{1}{4},\frac{1}{4},\frac{1}{4})} &\approx \epsilon_2 + \frac{16t_2^2}{|\Delta - \epsilon_1|} \\ E_{1,N=(0,\frac{1}{2},0)} &\approx \epsilon_2 \end{aligned} \quad (\text{S5.8})$$

If we turn off the hybridization term $t_2 = 0$, the energies of X, P points are much lower than the energy of Γ, M points (with energy difference $4|t_1|$). However, these energy differences are reduced by the hybridization. As a consequence, the energies of Γ, M, X, P points become similar. If we take

$$\frac{|\Delta - \epsilon_1||t_1|}{4t_2^2} = 1 \quad (\text{S5.9})$$

we can realize a relatively flat band with four out of five high symmetry points having similar energy

$$E_{\Gamma} \approx E_M \approx E_X \approx E_P \quad (\text{S5.10})$$

In practice, using the DFT numerical values, we find the system is close to the condition in Eq. S5.9 with $\frac{|\Delta - \epsilon_1||t_1|}{4t_2^2} = 0.91 \approx 1$.

Besides the high symmetry points, we also consider the dispersion along the high-symmetry line $\Gamma - X$. From Eq. S5.7, we find

$$\Gamma-X \quad : \quad \{(0, 0, x) | x \in [0, \frac{1}{2}]\}$$

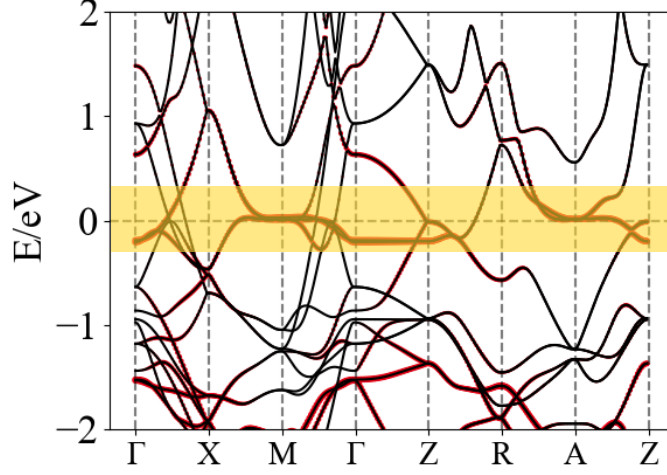


Figure S8. Dispersion in the conventional cell. Red dots label the orbital weights of $d_{x^2-y^2}, d_{z^2}$ orbitals.

$$E_{1,(0,0,x)} \approx \epsilon_2 + |4t_1| \cos\left(\frac{x}{2}\right)^2 + \frac{16t_2^2}{|\Delta - \epsilon_1|} \sin\left(\frac{x}{2}\right)^4 = \epsilon_2 + |4t_1| - |4t_1| \sin\left(\frac{x}{2}\right)^2 + \frac{16t_2^2}{|\Delta - \epsilon_1|} \sin\left(\frac{x}{2}\right)^4 \quad (\text{S5.11})$$

We can find the bandwidth along Γ - X line

$$\begin{aligned} \max_x E_{1,(0,0,x)} &= E_{1,(0,0,0)} = \epsilon_2 + 4|t_1| \\ \min_x E_{1,(0,0,x)} &= E_{1,(0,0,y)} \Big|_{\sin(y/2) = \frac{4|t_2|^2}{|t_1||\Delta - \epsilon_1|}} = \epsilon_2 + 4|t_2| - \frac{|\Delta - \epsilon_1|}{4} \\ \max_x E_{1,(0,0,x)} - \min_x E_{1,(0,0,x)} &= \frac{|\Delta - \epsilon_1|}{4} \approx 0.24\text{eV} \end{aligned} \quad (\text{S5.12})$$

where we observe the bandwidth has been reduced compared to the original bandwidth ($4t_2 \sim 1\text{eV}$) of the $d_{x^2-y^2}$ orbital along Γ - X line in the zero-hybridization limit ($t_2 = 0$). In addition, since the simplified two-orbital model has vanishing z -direction hopping, the band is flat along $\mathbf{b}_1 + \mathbf{b}_2 - \mathbf{b}_3$ direction (k_z direction).

In summary, we conclude that, due to the hybridization (or hopping) between $d_{x^2-y^2}$ and d_{z^2} orbitals, a relatively flat band has been generated near the Fermi energy.

To confirm the validity of the simplified two-orbital model, we also compare the flat-band wavefunctions obtained from the simplified two-orbital model and the DFT model. We find a good match between the two models, where the overlap of the wavefunctions reaches 84.7% [106].

Finally, we also show the band structure in the conventional cell (Fig. S8). The Brillouin zone of the conventional cell is folded, and we can still observe the relatively flat bands near Fermi energy formed by $d_{x^2-y^2}, d_{z^2}$ orbitals.

Appendix VI: Antiferromagnetism of c electrons

The existence of the relatively flat band leads to magnetic instability as we lower the temperature. Since the magnetic transition in the experiment happens at a relatively high temperature $T \sim 450\text{K}$. At such a high temperature, the Kondo effect is not present, and we can approximately treat f and c electrons as two decoupled degrees of freedom. We therefore only focus on the c electrons during our study of antiferromagnetism.

Before we discuss the corresponding instability, we first discuss the properties of flat bands. We notice that the lattice has a layered structure (Fig. S4). In our simplified two-orbital model (Eq. S5.1), t_1 denotes the in-plane (xy plane) hopping of $d_{x^2-y^2}$ orbitals, and t_2 denotes the in-plane (xy plane) hopping between $d_{x^2-y^2}$ and d_{z^2} orbitals. Moreover, the system is decoupled along z directions in the simplified two-orbital model. This indicates the relatively flat bands we discussed in Sec. V are atomic along z direction but non-atomic along xy directions.

The non-atomic nature along xy direction indicates the in-plane ferromagnetism [107]. The atomic nature along z direction combined with the weak dispersion along z direction leads to an out-of-plane antiferromagnetism [108]. We thus expect our current relatively flat band to stabilize a type-A antiferromagnetism (in-plane ferromagnetism and out-of-plane antiferromagnetism) with the magnetic structure shown in Fig. S4.

To understand the antiferromagnetism, we have performed the following calculations

- Mean-field calculations.
- A direct DFT calculation in the AFM phase where f electrons are treated as core states.
- Analytical calculations on the toy model (see Sec. XIV for the definition of the model and the details of the calculations).

As we will show later in this section, three calculations are qualitatively consistent with each other.

1. Mean-field theory

We first discuss the procedure of mean-field calculations. We consider the following interacting Hamiltonian of c electrons

$$H_{c,int} = H_c + H_{c,U} \quad (S6.1)$$

The interaction terms are

$$H_{c,U} = \frac{1}{2} \sum_{\mathbf{R},a,(i,\sigma) \neq (j,\sigma')} U_{ij,a} : c_{\mathbf{R},a,i,\sigma}^\dagger c_{\mathbf{R},a,i,\sigma} c_{\mathbf{R},a,j,\sigma'}^\dagger c_{\mathbf{R},a,j,\sigma'} : - \frac{1}{2} \sum_{\mathbf{R},a,i,j,\sigma,\sigma'} J_{ij,a} : c_{\mathbf{R},a,i,\sigma}^\dagger c_{\mathbf{R},a,i,\sigma'} c_{\mathbf{R},a,j,\sigma'}^\dagger c_{\mathbf{R},a,j,\sigma} : + \frac{1}{2} \sum_{\mathbf{R},a,i,j,\sigma,\sigma'} J_{ij,a} : c_{\mathbf{R},a,i,\sigma}^\dagger c_{\mathbf{R},a,i,\sigma'}^\dagger c_{\mathbf{R},a,j,\sigma'} c_{\mathbf{R},a,j,\sigma} : \quad (S6.2)$$

The interaction matrices for the five d orbitals of each Co atom are obtained from the *ab-initio* calculations using constraint random phase approximation [109–111] and are given below

$$U_a = \begin{bmatrix} 3.79eV & 2.78eV & 2.78eV & 2.33eV & 2.35eV \\ 2.78eV & 3.35eV & 2.33eV & 2.41eV & 2.45eV \\ 2.78eV & 2.33eV & 3.35eV & 2.41eV & 2.45eV \\ 2.33eV & 2.41eV & 2.41eV & 3.37eV & 2.96eV \\ 2.35eV & 2.45eV & 2.45eV & 2.96eV & 3.68eV \end{bmatrix}_{ij}, \quad J_a = \begin{bmatrix} 0eV & 0.39eV & 0.39eV & 0.64eV & 0.68eV \\ 0.39eV & 0eV & 0.48eV & 0.51eV & 0.53eV \\ 0.39eV & 0.48eV & 0eV & 0.51eV & 0.53eV \\ 0.64eV & 0.51eV & 0.51eV & 0eV & 0.28eV \\ 0.68eV & 0.53eV & 0.53eV & 0.28eV & 0eV \end{bmatrix}_{ij} \quad (S6.3)$$

To perform the mean-field coupling, we first rewrite the interaction term $H_{U,c}$ into the following generic formula

$$H_{U,c} = \frac{1}{2} \sum_{\mathbf{R},a} V_{\alpha\beta\gamma\delta} : c_{\mathbf{R},a,\alpha}^\dagger c_{\mathbf{R},a,\beta}^\dagger c_{\mathbf{R},a,\gamma} c_{\mathbf{R},a,\delta} : \quad (S6.4)$$

where we use $\alpha, \beta, \gamma, \delta$ to denote both the spin and orbital indices, and the on-site interactions are characterized by the tensor V . The Hartree-Fock (mean-field) decoupling of the four-fermion interactions term reads

$$H_{U,c}^{MF} = \frac{1}{2} \sum_{\mathbf{R},\alpha\beta\gamma\delta} V_{\alpha\beta\gamma\delta} \left\{ -O_{\mathbf{R},a,\alpha\delta} O_{\mathbf{R},a,\beta,\gamma} + O_{\mathbf{R},a,\alpha\gamma} O_{\mathbf{R},a,\beta,\delta} + \left[O_{\mathbf{R},a,\alpha\delta} : c_{\mathbf{R},a,\beta}^\dagger c_{\mathbf{R},a,\gamma} : - O_{\mathbf{R},a,\alpha\gamma} : c_{\mathbf{R},a,\beta}^\dagger c_{\mathbf{R},a,\delta} : + \text{h.c.} \right] \right\} \quad (S6.5)$$

where we have introduced the mean-fields

$$O_{\mathbf{R},a,\alpha\beta} = \langle : c_{\mathbf{R},a,\alpha}^\dagger c_{\mathbf{R},a,\beta} : \rangle \quad (S6.6)$$

The expectation value is taken with respect to the mean-field Hamiltonian

$$H_c^{MF} = H_c + H_{U,c}^{MF} \quad (S6.7)$$

The mean fields (Eq. S6.6) will be self-consistently determined. The final mean-field Hamiltonian then describes the dispersion of c electrons in the AFM phase

$$H_c^{AFM} = \sum_{\mathbf{k},ab,ij,\sigma\sigma'} \epsilon_{\mathbf{k},ab,ij,\sigma\sigma'}^{AFM} c_{\mathbf{k},a,i,\sigma}^\dagger c_{\mathbf{k},b,j,\sigma'} + E_0 \quad (S6.8)$$

where $\epsilon_{\mathbf{k},ab,ij}^{AFM}$ includes the contribution from the non-interacting Hamiltonian and also the contribution from mean-fields decoupling (Eq. S6.5). We will later specify which model was considered in the mean-field calculations. E_0 is the constant term from mean-field decoupling (Eq. S6.5).

2. Mean-field and DFT results of the AFM phase

To describe the magnetic order, it is more convenient to use the conventional cell. For what follows, we will always take the conventional cell as our unit cell. In addition, the conventional cell of the PM phase is the primitive cell of the type-A AFM phase. As we will show later in this section, the type-A AFM state is also the ground state with the lowest energy.

We first show the band structure of the PM phase in the conventional cell. As shown in Fig. S9, we can, again, observe the two-orbital model reproduce the relatively flat bands near the Fermi energy. We then discuss the mean-field results of the two-orbital model.

To describe the magnetic order, we note that there are four Co per unit cell (conventional cell) located at (see Fig. S4)

$$\left(0, \frac{1}{2}, \frac{1}{4}\right), \quad \left(\frac{1}{2}, 0, \frac{1}{4}\right), \quad \left(\frac{1}{2}, 0, \frac{3}{4}\right), \quad \left(0, \frac{1}{2}, \frac{3}{4}\right) \quad (\text{S6.9})$$

To realize different magnetic ordering, we take different initializations of the mean-fields O^{init} . We consider four types of magnetic order as shown below

- Type-A AFM

$$O_{\mathbf{R},a,(i\sigma,j\sigma')}^{init} = \begin{cases} n_0\sigma\delta_{i,j}\delta_{\sigma,\sigma'} & , \text{ if } a \in \{Co_1, Co_2\} \\ -n_0\sigma\delta_{i,j}\delta_{\sigma,\sigma'} & , \text{ if } a \in \{Co_3, Co_4\} \\ 0 & , \text{ otherwise} \end{cases} \quad (\text{S6.10})$$

- FM

$$O_{\mathbf{R},a,(i\sigma,j\sigma')}^{init} = \begin{cases} n_0\sigma\delta_{i,j}\delta_{\sigma,\sigma'} & , \text{ if } a \in \{Co_1, Co_2, Co_3, Co_4\} \\ 0 & , \text{ otherwise} \end{cases} \quad (\text{S6.11})$$

- In-plane AFM and out-of-plane AFM

$$O_{\mathbf{R},a,(i\sigma,j\sigma')}^{init} = \begin{cases} n_0\sigma\delta_{i,j}\delta_{\sigma,\sigma'} & , \text{ if } a \in \{Co_1, Co_3\} \\ -n_0\sigma\delta_{i,j}\delta_{\sigma,\sigma'} & , \text{ if } a \in \{Co_2, Co_4\} \\ 0 & , \text{ otherwise} \end{cases} \quad (\text{S6.12})$$

- In-plane AFM and out-of-plane FM

$$O_{\mathbf{R},a,(i\sigma,j\sigma')}^{init} = \begin{cases} n_0\sigma\delta_{i,j}\delta_{\sigma,\sigma'} & , \text{ if } a \in \{Co_1, Co_4\} \\ -n_0\sigma\delta_{i,j}\delta_{\sigma,\sigma'} & , \text{ if } a \in \{Co_2, Co_3\} \\ 0 & , \text{ otherwise} \end{cases} \quad (\text{S6.13})$$

The mean-field energies of the above states are

Order	Type-A AFM	FM	In-plane AFM and out-of-plane AFM	In-plane AFM and out-of-plane FM
$(E - E_0)/eV$	0	0.006	0.184	0.153

where we have subtracted the energy of the ground state E_0 (the energy of the type-A AFM phase).

We can observe that the type-A AFM phase is favored. Moreover, we can observe states with in-plane ferromagnetism (type-A AFM and FM) have much lower energy than in-plane antiferromagnetic states ($\sim 0.1eV$ lower). The energy difference between type-A AFM and FM is small ($\sim 0.01eV$). This is because the z -direction correlation comes from the out-of-plane coupling. Since the out-of-plane coupling is weak, the energy difference between type-A AFM and FM is relatively small.

In Fig. S10, we also show the mean-field band structures of the type-A AFM phase. We can also observe the magnetic order splits the relatively flat bands. We also perform calculations of the type-A AFM phase at different temperatures, where the evolution of order parameters as a function of temperature is given in Fig. S11. The order parameter is defined as the average magnetic momentum of each Co atom

$$m = \frac{1}{4N} \sum_{\mathbf{R},\sigma} \sum_i \left\langle \left[\sigma c_{\mathbf{R},Co1,i,\sigma}^\dagger c_{\mathbf{R},Co1,i,\sigma} + \sigma c_{\mathbf{R},Co2,i,\sigma}^\dagger c_{\mathbf{R},Co2,i,\sigma} \right] \right\rangle$$

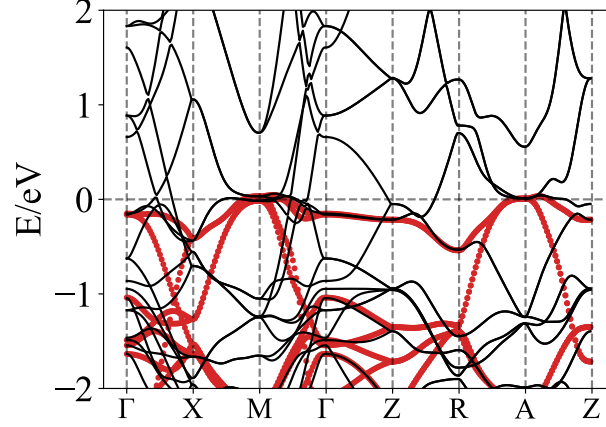


Figure S9. Comparison between DFT bands of c electrons (black) and the bands from the two-orbital model (red) in the conventional cell in the PM phase. In the conventional cell, the two-orbital model produces 8 two-fold-degenerate bands. We observe that the two-orbital model reproduces the relatively flat bands near the Fermi energy.

AFM band structure from mean-field calculation (two-orbital model)

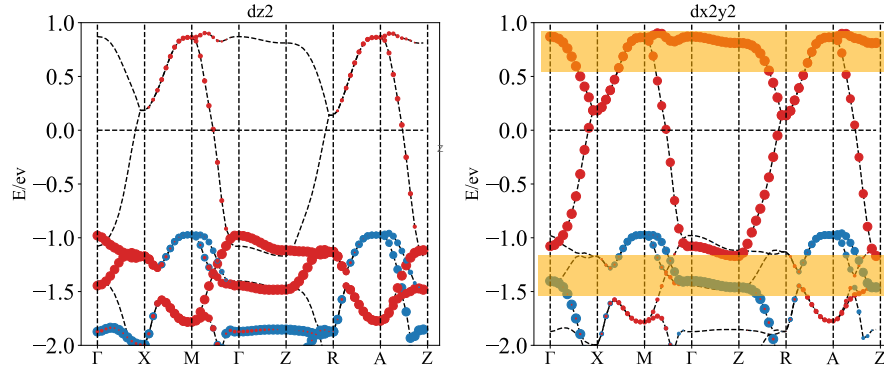


Figure S10. Dispersion of AFM phase obtained by solving two-orbital model via mean-field approximations at low temperatures $T = 0.001$ eV. Red color labels bands from spin \downarrow electrons of Co_1, Co_2 atoms and spin \uparrow electrons of Co_3, Co_4 atoms. Blue color labels bands from spin \uparrow electrons of Co_1, Co_2 atoms and spin \downarrow electrons of Co_3, Co_4 atoms. We can observe the splitting of the relatively flat bands due to the magnetism (yellow-shaded region). Sizes of the dots characterize the orbital weights of two relevant d orbitals. We observe that the polarized flat bands mostly come from the $d_{x^2-y^2}$ orbitals, which is also consistent with DFT results (Fig. S12).

$$- \left. \begin{aligned} & \sigma c_{\mathbf{R}, \text{Co}3, i, \sigma}^\dagger c_{\mathbf{R}, \text{Co}3, i, \sigma} - \sigma c_{\mathbf{R}, \text{Co}4, i, \sigma}^\dagger c_{\mathbf{R}, \text{Co}4, i, \sigma} \end{aligned} \right\} \quad (\text{S6.14})$$

Finally, we directly perform the DFT calculations in the magnetic phase which include all the spd orbitals and treat f electrons as core states. Again, we observe the type-A AFM phase has the lowest energy. The energies of various magnetic states are given below

Order ($E - E_0$)/eV	Type-A AFM	FM	In-plane AFM and out-of-plane AFM	In-plane AFM and out-of-plane FM
	0	0.013	0.236	0.238

where we have subtracted the energy of the ground state E_0 (the energy of the type-A AFM phase). The DFT band structures of the type-A AFM phase are shown in Fig. S12.

Finally, in Sec. XIV, we also employ perturbation theory to analytically demonstrate the stability of the AFM phase. Thus, all our calculations consistently support each other and indicate the stability of the AFM phase.

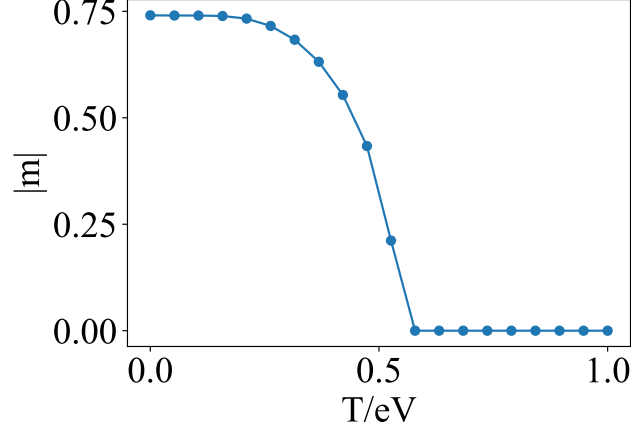


Figure S11. Evolution of order parameter m (Eq. S6.14) as a function of temperature.

AFM band structures from DFT calculations

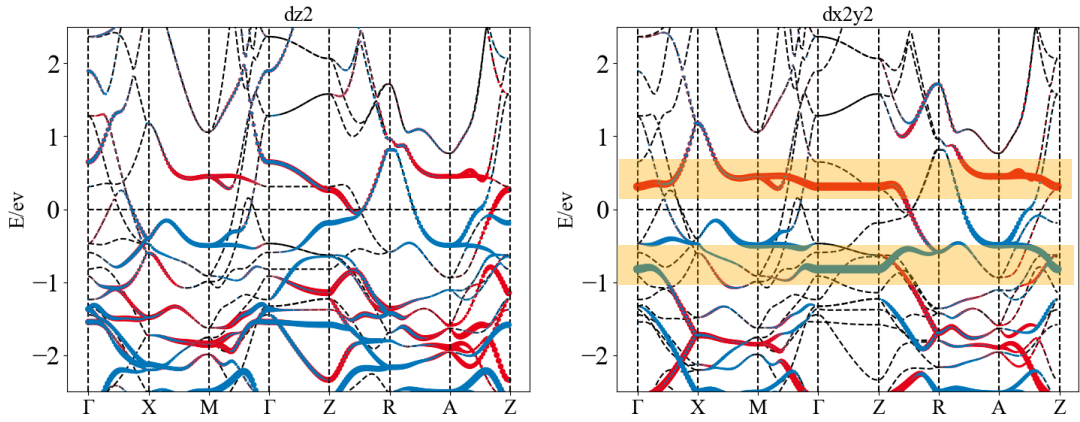


Figure S12. Direct DFT calculations in the AFM phase. The yellow regions mark the positions of the relatively flat bands. Red color labels bands from spin \downarrow electrons of Co_1 , Co_2 atoms and spin \uparrow electrons of Co_3 , Co_4 atoms. Blue color labels bands from spin \uparrow electrons of Co_1 , Co_2 atoms and spin \downarrow electrons of Co_3 , Co_4 atoms. Sizes of the dots characterize the orbital weights of two relevant d orbitals.

Appendix VII: Magnetism of LaCo_2P_2

We also study the magnetism in a related compound LaCo_2P_2 . There are two main differences between LaCo_2P_2 and CeCo_2P_2 . First, La holds zero f electrons, which indicates the absence of Kondo behavior. Second, due to the change of the distance between P atoms, $p_z@P$ electron bands cross the Fermi energy in LaCo_2P_2 (see Fig. S14). The same bands are above the Fermi energy in CeCo_2P_2 . As a consequence, these additional bands introduce effective RKKY interactions and stabilize ferromagnetic states. Here we comment that, in the CeCo_2P_2 , the $p_z@P$ orbitals are far from the Fermi energy and will not contribute to effective RKKY interactions.

We first discuss the band structures of LaCo_2P_2 and CeCo_2P_2 . We define the mirror-even and mirror-odd basis of $p_z@P$ orbitals in the conventional cell (Fig. S13)

$$\begin{aligned}
 c_{\mathbf{R},e/o,1,\sigma} &= \frac{1}{\sqrt{2}} \left(c_{\mathbf{R},P_1,p_z,\sigma} \pm c_{\mathbf{R}-(0,0,1),P_4,p_z,\sigma} \right) \\
 c_{\mathbf{R},e/o,2,\sigma} &= \frac{1}{\sqrt{2}} \left(c_{\mathbf{R},P_3,p_z,\sigma} \pm c_{\mathbf{R},P_2,p_z,\sigma} \right)
 \end{aligned} \tag{S7.1}$$

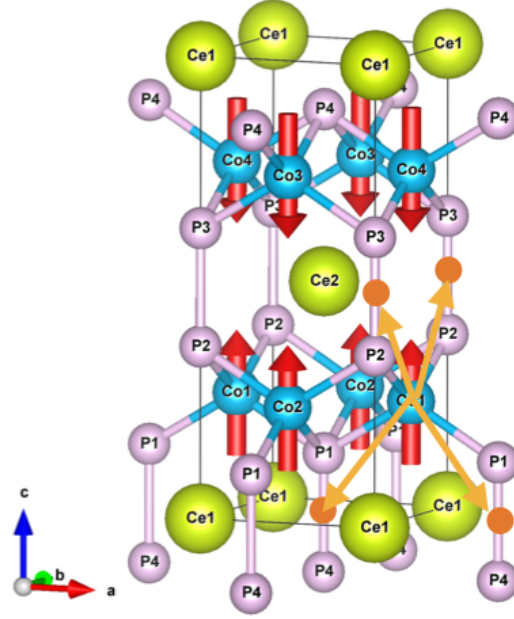


Figure S13. Orange dots mark the Wannier center of the mirror-even (mirror-odd) orbital of $p_z@P$ (Eq. S7.1). The orange arrows mark the nearest-neighbor hopping between the mirror-even orbitals and $d_{x^2-y^2}$ orbitals of Co₁ atom (Eq. S7.3).

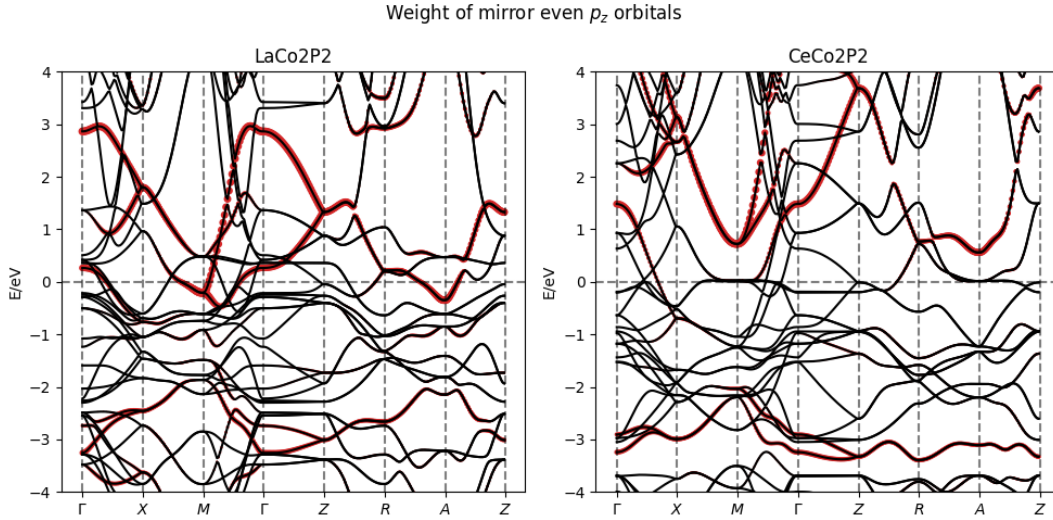


Figure S14. Band structures of LaCo₂P₂ and CeCo₂P₂ in the conventional cell. The red dots mark the orbital weights of the mirror even p_z orbitals.

We show the orbital weights of the mirror-even states in Fig. S14. We can observe that the mirror even states in the LaCo₂P₂ are close to the Fermi energy. This is because, the nearest-neighbor hopping $t_{p_z,z}$ of $p_z@P$ orbitals along z directions are 2.13eV

for LaCo_2P_2 and 2.65eV for CeCo_2P_2 . This hopping, after projecting to the mirror-even orbitals, behaves as a mass term

$$t_{p_z,z} \sum_{\mathbf{R},i=1,2,\sigma} c_{\mathbf{R},e,i,\sigma}^\dagger c_{\mathbf{R},e,i,\sigma} \quad (\text{S7.2})$$

Therefore, by reducing the values of $t_{p_z,z}$ in LaCo_2P_2 , the energy of $c_{\mathbf{R},e,i,\sigma}$ orbitals is also lower.

We next show the RKKY-like interactions induced by the coupling to the mirror-even p_z orbitals generate effective ferromagnetic interactions between Co d atoms and then stabilize a ferromagnetic order in LaCo_2P_2 . Since magnetism is mostly contributed by the $d_{x^2-y^2}$ orbitals of Co, we first investigate the hopping between $p_z@P$ and $d_{x^2-y^2}@Co$. The $d_{x^2-y^2}@Co$ couples to the four nearest-neighbor $p_z@P$ orbitals with strength $t_{p_z,d_{x^2-y^2}} = -0.487\text{eV}$. Then the nearest-neighbor coupling between mirror-even states and $d_{x^2-y^2}$ electrons reads (Fig. S13)

$$\begin{aligned} & \sum_{\mathbf{R},\sigma} \frac{1}{\sqrt{2}} t_{p_z,d_{x^2-y^2}} \left[c_{\mathbf{R},Co_1,d_{x^2-y^2}}^\dagger \left(c_{\mathbf{R},e,1,\sigma} + c_{\mathbf{R}+(-1,0,0),e,1,\sigma} + c_{\mathbf{R},e,2,\sigma} + c_{\mathbf{R}+(0,1,0),e,2,\sigma} \right) \right. \\ & + c_{\mathbf{R},Co_2,d_{x^2-y^2}}^\dagger \left(c_{\mathbf{R},e,1,\sigma} + c_{\mathbf{R}+(1,0,0),e,1,\sigma} + c_{\mathbf{R},e,2,\sigma} + c_{\mathbf{R}+(0,-1,0),e,2,\sigma} \right) \\ & + c_{\mathbf{R},Co_3,d_{x^2-y^2}}^\dagger \left(c_{\mathbf{R}+(0,0,1),e,1,\sigma} + c_{\mathbf{R}+(1,0,1),e,1,\sigma} + c_{\mathbf{R},e,2,\sigma} + c_{\mathbf{R}+(0,-1,0),e,2,\sigma} \right) \\ & \left. + c_{\mathbf{R},Co_4,d_{x^2-y^2}}^\dagger \left(c_{\mathbf{R}+(0,0,1),e,1,\sigma} + c_{\mathbf{R}+(0,1,1),e,1,\sigma} + c_{\mathbf{R},e,2,\sigma} + c_{\mathbf{R}+(-1,0,0),e,2,\sigma} \right) + \text{h.c.} \right] \quad (\text{S7.3}) \end{aligned}$$

We can then observe that, locally, each $c_{\mathbf{R},Co_i,d_{x^2-y^2}}$ orbitals couple to a molecular orbital formed by the mirror-even states of p_z electrons. We can thus define

$$\begin{aligned} w_{\mathbf{R},e,1,\sigma} &= \frac{1}{2} \left(c_{\mathbf{R},e,1,\sigma} + c_{\mathbf{R}+(-1,0,0),e,1,\sigma} + c_{\mathbf{R},e,2,\sigma} + c_{\mathbf{R}+(0,1,0),e,2,\sigma} \right) \\ w_{\mathbf{R},e,2,\sigma} &= \frac{1}{2} \left(c_{\mathbf{R},e,1,\sigma} + c_{\mathbf{R}+(1,0,0),e,1,\sigma} + c_{\mathbf{R},e,2,\sigma} + c_{\mathbf{R}+(0,-1,0),e,2,\sigma} \right) \\ w_{\mathbf{R},e,3,\sigma} &= \frac{1}{2} \left(c_{\mathbf{R}+(0,0,1),e,1,\sigma} + c_{\mathbf{R}+(1,0,1),e,1,\sigma} + c_{\mathbf{R},e,2,\sigma} + c_{\mathbf{R}+(0,-1,0),e,2,\sigma} \right) \\ w_{\mathbf{R},e,4,\sigma} &= \frac{1}{2} \left(c_{\mathbf{R}+(0,0,1),e,1,\sigma} + c_{\mathbf{R}+(0,1,1),e,1,\sigma} + c_{\mathbf{R},e,2,\sigma} + c_{\mathbf{R}+(-1,0,0),e,2,\sigma} \right) \quad (\text{S7.4}) \end{aligned}$$

and then Eq. S7.3 can be written as

$$\sum_{\mathbf{R},\sigma} \sum_{i=1,2,3,4} \sqrt{2} t_{p_z,d_{x^2-y^2}} \left[c_{\mathbf{R},Co_i,d_{x^2-y^2}}^\dagger w_{\mathbf{R},e,i,\sigma} + \text{h.c.} \right] \quad (\text{S7.5})$$

This hopping term then introduces an effective spin-spin or Kondo-like coupling between $w_{\mathbf{R},b,i,\sigma}$ and $c_{\mathbf{R},Co_i,d_{x^2-y^2}}$ (see also Appendix IX)

$$J_K \sum_{\mathbf{R},i,\mu,\sigma_1,\sigma_2,\sigma_3,\sigma_4} w_{\mathbf{R},b,i,\sigma_1}^\dagger \sigma_{\sigma_1,\sigma_2}^\mu w_{\mathbf{R},b,i,\sigma_2} c_{\mathbf{R},Co_i,d_{x^2-y^2},\sigma_3}^\dagger \frac{\sigma_{\sigma_3,\sigma_4}^\mu}{2} c_{\mathbf{R},Co_i,d_{x^2-y^2},\sigma_4} \quad (\text{S7.6})$$

where $J_K = 4|t_{p_z,d_{x^2-y^2}}|^2/|U_d|$ is the coupling strength. U_d is the strength of Hubbard repulsion of Co d electrons. We observe d electron develops magnetic order and has strong interactions $U_d \sim 4\text{eV}$ (from DFT calculation). This indicates d electrons are correlated. However, in general, p_z orbitals are itinerant and weakly correlated, since p orbitals have a very strong hopping ($\sim 2\text{eV}$). Therefore, d orbitals and p orbitals are coupled via an effective Kondo type of coupling. The particle-hole fluctuations of the p orbitals then generate effective RKKY interactions between d orbitals via the Kondo coupling (see Appendix S5 of Ref. [112] for the derivations of RKKY interactions and also Refs. [113–115]) are

$$\begin{aligned} & \sum_{\mathbf{R},\mathbf{R}'} J_{\mathbf{R}-\mathbf{R}'}^{RKKY} S_{\mathbf{R},Co_i,d_{z^2}}^\mu S_{\mathbf{R}',Co_i,d_{z^2}}^\nu \\ J_{\mathbf{R}-\mathbf{R}'}^{RKKY} &= -\frac{1}{2} J_K^2 \chi_{ij,\mathbf{R}-\mathbf{R}'} \quad (\text{S7.7}) \end{aligned}$$

where $S_{\mathbf{R},Co_i,d_{z^2}} = \sum_{\sigma_1,\sigma_2} c_{\mathbf{R},Co_i,d_{x^2-y^2},\sigma_1} \frac{\sigma_1^\mu \sigma_2^\mu}{2} c_{\mathbf{R},Co_i,d_{x^2-y^2},\sigma_2}^\dagger$ is the spin operator of $d_{x^2-y^2}$ orbitals of Co_i atom and the susceptibility is defined as

$$\begin{aligned} \chi_{ij,\mathbf{R}-\mathbf{R}'} &= - \int_0^\beta G_{ij}(\mathbf{R}-\mathbf{R}',\tau) G_{ji}(\mathbf{R}'-\mathbf{R},-\tau) d\tau \\ G_{ij}(\mathbf{R},\tau) &= - \langle T_\tau w_{\mathbf{R},b,i,\sigma}(\tau) w_{\mathbf{R}',b,j,\sigma}^\dagger(0) \rangle \end{aligned} \quad (\text{S7.8})$$

Since we have a strong in-plane ferromagnetic coupling due to the non-atomic nature of the flat band, we now aim to understand what types of out-of-plane coupling the RKKY interaction generates. We can estimate the nearest-neighbor RKKY coupling along z directions, which is equivalent to calculate

$$J_z = -\frac{J_K^2}{2} \chi_{14,\mathbf{R}=0} = -\frac{J_K^2}{2} \chi_{23,\mathbf{R}=0} \quad (\text{S7.9})$$

By numerical calculations, we find $\chi_{14,\mathbf{R}=0} = \chi_{23,\mathbf{R}=0} = 0.018\text{eV}^{-1} > 0$. We observe that, Co_4 (Co_3) atom is on top of the Co_1 (Co_2) atom. Then the nearest-neighbor RKKY interactions along z directions are proportional to $\chi_{12,\mathbf{R}=0}$ or $\chi_{23,\mathbf{R}=0}$. These interactions are ferromagnetic and favor the formation of ferromagnetism along z directions.

To further confirm the stability of the ferromagnetic state, we calculate the energy of the ferromagnetic state and type-A antiferromagnetic state via DFT calculations. We indeed find that the energy of the ferromagnetic state is 6.2 meV lower than the type-A antiferromagnetic state.

Appendix VIII: Atomic limit of f electron

In this appendix, we discuss the atomic physics of f electrons. We pick out f electrons at site \mathbf{R}_0 and sublattice a

$$f_{i,\sigma} = f_{\mathbf{R}_0,a,i,\sigma} \quad (\text{S8.1})$$

Since all Ce atoms are equivalent, the choice of \mathbf{R}_0, a does not affect the atomic physics. The single-site Hamiltonian of f electrons is given in Eq. S3.6 and is also shown below

$$\begin{aligned} H_{loc}[f^\dagger, f] &= H_U[f^\dagger, f] + H_{CEF}[f^\dagger, f] + H_{soc}[f^\dagger, f] \\ H_U[f^\dagger, f] &= \frac{U}{2} \left(\sum_{i,\sigma} f_{i,\sigma}^\dagger f_{i,\sigma} - n_0 \right)^2 \\ H_{CEF}[f^\dagger, f] &= \sum_{ij} \epsilon_{f,ij} f_{i,\sigma}^\dagger f_{j,\sigma} \\ H_{soc}[f, f^\dagger] &= \lambda \sum_{\mu} L^\mu S^\mu. \end{aligned} \quad (\text{S8.2})$$

H_U is the on-site Hubbard interaction, H_{CEF} is the crystal field splitting and H_{soc} is the spin-orbit coupling (Eq. S8.9). Seven f orbitals are labeled by

$$f_1 = f_{z^3}, \quad f_2 = f_{xz^2}, \quad f_3 = f_{yz^2}, \quad f_4 = f_{z(x^2-y^2)}, \quad f_5 = f_{xyz}, \quad f_6 = f_{x(x^2-3y^2)}, \quad f_7 = f_{y(3x^2-y^2)} \quad (\text{S8.3})$$

The site symmetry group of Ce is $4/mmm$. After including the spin index, the orbitals form the following irreducible representations of the site symmetry group (see Tab. S1)

$$\begin{aligned} f_{1,\uparrow}^\dagger, f_{1,\downarrow}^\dagger &: \overline{\Gamma}_9 \\ f_{4,\uparrow}^\dagger, f_{4,\downarrow}^\dagger &: \overline{\Gamma}_8 \\ f_{5,\uparrow}^\dagger, f_{5,\downarrow}^\dagger &: \overline{\Gamma}_8 \\ \frac{f_{2,\uparrow}^\dagger - if_{3,\uparrow}^\dagger}{\sqrt{2}}, \frac{f_{2,\downarrow}^\dagger + if_{3,\downarrow}^\dagger}{\sqrt{2}} &: \overline{\Gamma}_9 \\ \frac{f_{2,\downarrow}^\dagger - if_{3,\downarrow}^\dagger}{\sqrt{2}}, \frac{f_{2,\uparrow}^\dagger + if_{3,\uparrow}^\dagger}{\sqrt{2}} &: \overline{\Gamma}_8 \end{aligned}$$

Irrep	2 ₀₀₁	4 ₀₀₁ ⁺	2 ₀₁₀	-1
$\bar{\Gamma}_8$	0	$-\sqrt{3}$	0	-2
$\bar{\Gamma}_9$	0	$\sqrt{2}$	0	-2

Table S1. Character table of 4/mmm.

$$\begin{aligned}
& \frac{f_{6,\uparrow}^\dagger - if_{7,\uparrow}^\dagger}{\sqrt{2}}, \frac{f_{6,\downarrow}^\dagger + if_{7,\downarrow}^\dagger}{\sqrt{2}} : \bar{\Gamma}_8 \\
& \frac{f_{6,\downarrow}^\dagger - if_{7,\downarrow}^\dagger}{\sqrt{2}}, \frac{f_{6,\uparrow}^\dagger + if_{7,\uparrow}^\dagger}{\sqrt{2}} : \bar{\Gamma}_9
\end{aligned} \tag{S8.4}$$

For future convenience, we also show the relation between the wavefunction of $f_{1,\dots,7}$ and spherical harmonic wave functions below:

Orbital	Wavefunction	Harmonics
$f_1 = f_{z^3}$	$\frac{\sqrt{7}}{4\sqrt{\pi}}(5 \cos^3(\theta) - 3 \cos(\theta))$	Y_3^0
$f_2 = f_{xz^2}$	$\frac{\sqrt{21}}{4\sqrt{2\pi}}(5 \cos^2(\theta) - 1) \sin(\theta) \cos(\phi)$	$(Y_3^{-1} - Y_3^1)/\sqrt{2}$
$f_3 = f_{yz^2}$	$\frac{\sqrt{21}}{4\sqrt{2\pi}}(5 \cos^2(\theta) - 1) \sin(\theta) \sin(\phi)$	$i(Y_3^{-1} + Y_3^1)/\sqrt{2}$
$f_4 = f_{z(x^2-y^2)}$	$\frac{\sqrt{105}}{4\sqrt{\pi}} \sin(\theta)^2 \cos(\theta) \cos(2\phi)$	$\frac{1}{\sqrt{2}}(Y_3^{-2} + Y_3^2)$
$f_5 = f_{xyz}$	$\frac{\sqrt{105}}{4\sqrt{\pi}} \sin(\theta)^2 \cos(\theta) \sin(2\phi)$	$\frac{i}{\sqrt{2}}(Y_3^{-2} - Y_3^2)$
$f_6 = f_{x(x^2-3y^2)}$	$\frac{\sqrt{35}}{4\sqrt{2\pi}} \sin^3(\theta)(\cos^2(\phi) - 3 \sin^2(\phi)) \cos(\phi)$	$\frac{1}{\sqrt{2}}(Y_3^{-3} - Y_3^3)$
$f_7 = f_{y(3x^2-y^2)}$	$\frac{\sqrt{35}}{4\sqrt{2\pi}} \sin^3(\theta)(3 \cos^2(\phi) - \sin^2(\phi)) \cos(\phi)$	$\frac{i}{\sqrt{2}}(Y_3^{-3} + Y_3^3)$

Y_L^m denotes the spherical Harmonic function which is also the eigenfunctions of the angular-momentum operator along z -direction (L^z). Based on the eigenvectors of L^z , we can introduce the following new electron operators $g_{l,\sigma}$

$$\begin{aligned}
g_{0,\sigma}^\dagger &= f_{1,\sigma}^\dagger \\
g_{1,\sigma}^\dagger &= \frac{1}{\sqrt{2}}(-f_{2,\sigma}^\dagger - if_{3,\sigma}^\dagger), \quad g_{-1,\sigma}^\dagger = \frac{1}{\sqrt{2}}(f_{2,\sigma}^\dagger - if_{3,\sigma}^\dagger) \\
g_{2,\sigma}^\dagger &= \frac{1}{\sqrt{2}}(f_{4,\sigma}^\dagger + if_{5,\sigma}^\dagger), \quad g_{-2,\sigma}^\dagger = \frac{1}{\sqrt{2}}(f_{4,\sigma}^\dagger - if_{5,\sigma}^\dagger) \\
g_{3,\sigma}^\dagger &= \frac{1}{\sqrt{2}}(-f_{6,\sigma}^\dagger - if_{7,\sigma}^\dagger), \quad g_{-3,\sigma}^\dagger = \frac{1}{\sqrt{2}}(f_{6,\sigma}^\dagger - if_{7,\sigma}^\dagger)
\end{aligned} \tag{S8.5}$$

where $g_{l,\sigma}^\dagger$ creates an f electron with L^z eigenvalue l and spin σ .

In what follows, we will discuss the eigenstates of the atomic Hamiltonian of f electrons. The Hubbard interaction ($\sim 10\text{eV}$) is the largest energy scale which forces the filling of f electrons to be 1 for each site. The spin-orbit coupling ($\sim 0.1\text{eV}$) is the second-largest energy scale which introduces an energy splitting between states with different total angular momentum. The crystal field splitting ($\sim 0.01\text{eV}$) is the smallest energy scale which further splits the energies of the states with the same total angular momentum.

1. Hubbard interactions and charge ± 1 excitation

We first discuss the effect of Hubbard interactions

$$H_U[f, f^\dagger] = \frac{U}{2}(n^f - n_0)^2 \tag{S8.6}$$

where

$$n^f = \sum_{i,\sigma} f_{i,\sigma}^\dagger f_{i,\sigma} \tag{S8.7}$$

Since the system is in the Kondo limit with one f electron per Ce atoms, the charge fluctuations of f electron are suppressed by the Hubbard U . We then take $n_0 = 1$ and treat U as the largest energy scale of the problem. The ground states of the H_U are described by the atomic states of f electron with exactly one f electron. The excitation energy of charge ± 1 excitation is $U/2$. Here, we also comment that, to simplify the problem, we do not include the orbital dependency of the Hubbard repulsion.

2. Spin-orbit coupling

The on-site Hubbard interaction fixes the filling of f electron to be one per Ce atom. This leads to a 14-fold degenerate one-electron ground states (7×2 f electrons). The degeneracy of the ground states will be lifted by the spin-orbit coupling and crystal fields. From our DFT calculations by treating f electrons as valence electrons, we find the strength of the spin-orbit coupling is

$$\lambda = 0.092\text{eV}. \quad (\text{S8.8})$$

Since spin-orbit coupling is usually larger than the crystal field splitting, we first consider the effect of H_{soc} . In the $g_{l,\sigma}$ basis (Eq. S8.5), the spin-orbit coupling can be written as

$$\begin{aligned} H_{soc}[f, f^\dagger] &= \lambda \sum_{\mu} L^{\mu} S^{\mu} \\ S^{\mu} &= \sum_{l,\sigma\sigma'} g_{l,\sigma}^{\dagger} \frac{\sigma_{\sigma\sigma'}^{\mu}}{2} g_{l,\sigma'} \\ L^{\mu} &= \sum_{l,l',\sigma\sigma'} g_{l,\sigma}^{\dagger} M_{l'l'}^{L,\mu} g_{l',\sigma} \end{aligned} \quad (\text{S8.9})$$

where σ^{μ} are Pauli matrices and the angular-momentum matrices $M_{l'l'}^{L,\mu}$ are defined as

$$\begin{aligned} M_{l'l'}^{L,z} &= \delta_{l,l'} l \\ M^{L,x} &= \frac{1}{2}(M^{L,+} + M^{L,-}), \quad M^{L,y} = \frac{1}{2i}(M^{L,+} - M^{L,-}) \\ M_{l'l'}^{L,+} &= \delta_{l'+1,l} \sqrt{L(L+1) - l'(l'+1)}, \quad M_{l'l'}^{L,-} = \delta_{l-1,l'} \sqrt{L(L+1) - l'(l'-1)}, \quad L = 3 \end{aligned} \quad (\text{S8.10})$$

After diagonalizing H_{soc} , we find the following eigenvalues (for the states with particle number 1)

$$\begin{aligned} E_0 &= -2\lambda, \quad 6\text{-fold degeneracy with total angular momentum } J = 5/2 \\ E_1 &= 3/2\lambda, \quad 8\text{-fold degeneracy with total angular momentum } J = 7/2 \end{aligned} \quad (\text{S8.11})$$

where $E_1 - E_0 \sim 0.322\text{eV}$.

3. Crystal field splitting

We next consider the crystal field splitting. The symmetry-allowed crystal field splitting can be obtained by only allowing hybridization between orbitals that form the same irreducible representation of the site-symmetry group and have the same spin indices. The crystal field splitting then takes the form of

$$\begin{aligned} H_{CEF}[f, f^\dagger] &= \sum_{\sigma} \left[\epsilon_1 f_{1,\sigma}^{\dagger} f_{1,\sigma} + \epsilon_2 (f_{2,\sigma}^{\dagger} f_{2,\sigma} + f_{3,\sigma}^{\dagger} f_{3,\sigma}) + \epsilon_4 f_{4,\sigma}^{\dagger} f_{4,\sigma} + \epsilon_5 f_{5,\sigma}^{\dagger} f_{5,\sigma} + \epsilon_6 (f_{6,\sigma}^{\dagger} f_{6,\sigma} + f_{7,\sigma}^{\dagger} f_{7,\sigma}) \right. \\ &\quad \left. + \epsilon_7 \left(-f_{2,\sigma}^{\dagger} f_{6,\sigma} + f_{3,\sigma}^{\dagger} f_{7,\sigma} + \text{h.c.} \right) \right] \\ &= \sum_{\sigma} \left[\epsilon_1 g_{0,\sigma}^{\dagger} g_{0,\sigma} + \epsilon_2 (g_{1,\sigma}^{\dagger} g_{1,\sigma} + g_{-1,\sigma}^{\dagger} g_{-1,\sigma}) + \epsilon_6 (g_{3,\sigma}^{\dagger} g_{3,\sigma} + g_{-3,\sigma}^{\dagger} g_{-3,\sigma}) \right. \\ &\quad \left. + \frac{\epsilon_4 + \epsilon_5}{2} (g_{2,\sigma}^{\dagger} g_{2,\sigma} + g_{-2,\sigma}^{\dagger} g_{-2,\sigma}) + \frac{\epsilon_4 - \epsilon_5}{2} (g_{2,\sigma}^{\dagger} g_{-2,\sigma} + g_{-2,\sigma}^{\dagger} g_{2,\sigma}) \right. \\ &\quad \left. + \epsilon_7 \left(g_{-1,\sigma}^{\dagger} g_{3,\sigma} + g_{1,\sigma}^{\dagger} g_{-3,\sigma} + \text{h.c.} \right) \right] \end{aligned} \quad (\text{S8.12})$$

where we have (from our DFT calculations by treating f as valence electrons)

$$\epsilon_1 = 0.0346eV, \quad \epsilon_2 = -0.0501eV, \quad \epsilon_4 = -0.0400eV, \quad \epsilon_5 = 0.0885eV, \quad \epsilon_6 = 0.00876eV, \quad \epsilon_7 = 0.0469eV. \quad (\text{S8.13})$$

H_{CEF} will lift the degeneracy of the 6-fold degenerate states with angular momentum $J = \frac{5}{2}$. It will also lift the degeneracy of the 8-fold degenerate states with angular momentum $J = \frac{7}{2}$.

For future reference, we now use η_i to denote the electrons corresponding to the i -th eigenstates of the whole atomic Hamiltonian with energy E_i

$$(H_U[f, f^\dagger] + H_{soc}[f, f^\dagger] + H_{CEF}[f, f^\dagger])\eta_i^\dagger|0\rangle = E_i\eta_i^\dagger|0\rangle, \quad i = 1, \dots, 14 \quad (\text{S8.14})$$

where η_i is a linear combination of f electron operators and can be obtained by solving the atomic Hamiltonian (Eq. S8.2). We note that the local Hamiltonian also has time-reversal symmetry, thus all the eigenstates with particle number 1 are two-fold degenerate. Without loss of generality, we take $E_{2i-1} = E_{2i}$ to characterize such degeneracy.

After introducing the crystal field splitting, the total angular momentum J is no longer a good quantum number because the crystal field term introduces hybridization between $J = 5/2$ states and $J = 7/2$ states. However, since crystal field splitting is relatively small compared to the spin-orbit coupling, the eigenvalues of the local Hamiltonian can still be separated into two groups with energy difference around $\frac{3}{2}\lambda - (-2\lambda) = \frac{7}{2}\lambda$ (Eq. S8.11). Therefore, we still use $J = 5/2$ and $J = 7/2$ to denote two groups of η states.

Numerically, we directly solve Eq. S8.14 and obtain the energy levels of the atomic problem with one f electron. The numerical values of E_i are

$$J = \frac{5}{2} : \begin{cases} E_1 = E_2 = -0.2073eV \\ E_3 = E_4 = -0.1983eV \\ E_5 = E_6 = -0.1771eV \end{cases} \quad J = \frac{7}{2} : \begin{cases} E_7 = E_8 = 0.1117eV \\ E_9 = E_{10} = 0.1196eV \\ E_{11} = E_{12} = 0.1727eV \\ E_{13} = E_{14} = 0.1789eV \end{cases} \quad (\text{S8.15})$$

We notice that with one f electron, the energy contribution from H_U (Eq. S8.6) is zero since $n_0 = 1$. We observe the energy difference $E_3 - E_1 \approx 9\text{meV}$ and $E_5 - E_1 \approx 30\text{meV}$. The energy differences between $J = \frac{7}{2}$ states and the ground state is around $\text{mean}_{j=7,\dots,14}(E_j - E_1) = 353.1\text{meV}$.

Appendix IX: Kondo lattice model

Due to the large Hubbard interactions, the charge fluctuations of f electrons are suppressed. There will be exactly one f electron for each Ce atom. In other words, f electrons now behave as local moments. We can perform a Schrieffer-Wolff transformation (as we describe in Sec. XIII) and map the original periodic Anderson model to a Kondo lattice model. Since the Kondo effect is developed below the T_{AFM} , for what follows, we will use the paramagnetic conventional cell, which is the magnetic primitive cell, to describe the system.

1. Kondo coupling

We start with the following periodic Anderson model

$$H = H_c^{\text{AFM}} + H_V + H_f \quad (\text{S9.1})$$

where

$$H_c^{\text{AFM}} = \sum_{\mathbf{k}, abij, \sigma} \epsilon_{\mathbf{k}, ai, bj}^{\text{AFM}} c_{\mathbf{k}, ai\sigma}^\dagger c_{\mathbf{k}, bj\sigma} \quad (\text{S9.2})$$

is the single-particle Hamiltonian of the c electrons in the AFM phase, H_V is the fc hybridization term (Eq. S3.3), and H_f describes the atomic Hamiltonian of f electrons (Eq. S3.5).

To perform the Schrieffer-Wolff transformation, we first separate the Hilbert space into low-energy subspace and high-energy subspace. We let the low-energy states be the states with 1 f electrons per Ce atom, and let the high-energy states be the states that violate the aforementioned filling constraints. The low-energy and high-energy subspaces are spanned by the low-energy and high-energy states respectively.

We let $\eta_{\mathbf{R},a,i}^\dagger$ to characterize the eigenstates of the interacting Hamiltonian of f electrons H_{loc} (Eq. S8.2). In Eq. S8.14, we have introduced η_i for the single-site/atomic problem. Here, similarly, we let $\eta_{\mathbf{R},a,i}^\dagger$ to denote the one-electron eigenstates of the local Hamiltonian of each site (Eq. S8.14)

$$\begin{aligned}\eta_{\mathbf{R},a,i}^\dagger|\mathbf{R},a,0\rangle &= |\mathbf{R},a,i\rangle, \quad i = 1, \dots, 14 \\ H_{loc}[f_{\mathbf{R},a}^\dagger, f_{\mathbf{R},a}]|\mathbf{R},a,i\rangle &= E_i|\mathbf{R},a,i\rangle\end{aligned}\quad (\text{S9.3})$$

\mathbf{R} is the position of unit cell and a is the sublattice. $|\mathbf{R},a,i\rangle$ is the eigenstate of H_{loc} with one f electrons at Ce_a atom in the unit cell \mathbf{R} . $|\mathbf{R},a,0\rangle$ denotes the state with zero f electron at Ce_a atom in the unit cell \mathbf{R} . $\eta_{\mathbf{R},a,i}$ is the superposition of f electron operators that creates the eigenstate of H_{loc} and can be written as

$$\eta_{\mathbf{R},a,i} = \sum_{j,\sigma} U_{i,j\sigma}^\eta f_{\mathbf{R},a,j,\sigma} \quad (\text{S9.4})$$

The matrix $U_{i,j\sigma}^\eta$ can be obtained by numerically solving the atomic Hamiltonian H_{loc} in the one-electron sector.

The high-energy states we considered are empty states ($|\mathbf{R},a,0\rangle$) and doubly-occupied states ($|\mathbf{R},a,i,j\rangle$) which corresponds to the charge ∓ 1 excitation of the local Hamiltonian

$$\begin{aligned}|\mathbf{R},a,0\rangle, \quad H_{loc}[f_{\mathbf{R},a}^\dagger, f_{\mathbf{R},a}]|\mathbf{R},0\rangle &\approx E_H|0\rangle \\ |\mathbf{R},a,i,j\rangle = \eta_{\mathbf{R},i}^\dagger \eta_{\mathbf{R},j}^\dagger |\mathbf{R},a,0\rangle, \quad H_{loc}[f_{\mathbf{R},a}^\dagger, f_{\mathbf{R},a}]|\mathbf{R},a,i,j\rangle &\approx E_H|\mathbf{R},a,i,j\rangle \\ E_H &= U/2\end{aligned}\quad (\text{S9.5})$$

where the fermion anti-commutation relation also indicates

$$|\mathbf{R},a,i,j\rangle = -|\mathbf{R},a,j,i\rangle \quad (\text{S9.6})$$

Since U is the largest scale, we ignore the effect of spin-orbit coupling and crystal field splitting on the charge ± 1 excitation and let the excitation energy be $E_H = \frac{U}{2}$.

In the η basis, we can also rewrite the fc hybridization term (Eq. S3.3) as

$$\begin{aligned}H_V &= \sum_{\mathbf{R}} \sum_{i,a,b,\Delta\mathbf{R},j\sigma} V_{ai,bj\sigma}(\Delta\mathbf{R}) \eta_{\mathbf{R},a,i}^\dagger c_{\mathbf{R}+\Delta\mathbf{R},b,j,\sigma} + \text{h.c.} \\ V_{ai,bj\sigma}(\Delta\mathbf{R}) &= \sum_{i'} U_{i,i'\sigma}^\eta V_{ab,i'j}^c(\Delta\mathbf{R})\end{aligned}\quad (\text{S9.7})$$

where $V_{ab,i'j}^c$ has been introduced in Eq. S3.3.

For convenience, we introduce the molecular orbital

$$\begin{aligned}w_{\mathbf{R},a,i} &= \frac{1}{v_{a,i}} \sum_{\Delta\mathbf{R},bj\sigma} V_{ai,bj\sigma}(\Delta\mathbf{R}) c_{\mathbf{R}+\Delta\mathbf{R},b,j,\sigma} \\ v_{a,i}^2 &= \sum_{\Delta\mathbf{R},bj\sigma} |V_{ai,bj\sigma}(\Delta\mathbf{R})|^2\end{aligned}\quad (\text{S9.8})$$

$\{w_{\mathbf{R},a,i}\}_{\mathbf{R},a,i}$ are not orthogonal and follow

$$\begin{aligned}\{w_{\mathbf{R},a,i}, w_{\mathbf{R}',b,j}^\dagger\} &= A_{\mathbf{R}ai,\mathbf{R}'bj} \\ A_{\mathbf{R}ai,\mathbf{R}'bj} &= \frac{1}{v_{a,i} v_{a,j}} \sum_{\Delta\mathbf{R},cs\sigma} V_{ai,cs\sigma}(\Delta\mathbf{R}) V_{bj,cs\sigma}^*(\mathbf{R} + \Delta\mathbf{R} - \mathbf{R}')\end{aligned}\quad (\text{S9.9})$$

We can observe that, in the $w_{\mathbf{R},a,i}$ electron basis, the hybridization term can be written in a more compact form

$$H_V = \sum_{\mathbf{R},ai} v_{a,i} \eta_{\mathbf{R},a,i}^\dagger w_{\mathbf{R},a,i} + \text{h.c.} \quad (\text{S9.10})$$

We now aim to perform SW transformation to our interacting Hamiltonian. We first separate our interacting Hamiltonian into the unperturbed part (H_0) and the perturbation (H_1)

$$H = H_0 + H_1$$

$$H_0 = H_c^{\text{AFM}} + \sum_{\mathbf{R},a} H'_{loc}(\mathbf{R}, a), \quad H'_{loc}(\mathbf{R}, a) = \sum_i E_{a,i} |\mathbf{R}, a, i\rangle \langle \mathbf{R}, a, i| + \frac{U}{2} \left[|\mathbf{R}, a, 0\rangle \langle \mathbf{R}, a, 0| + \sum_{i>j} |\mathbf{R}, a, i, j\rangle \langle \mathbf{R}, a, i, j| \right]$$

$$H_1 = \sum_{\mathbf{R},a,i} v_{a,i} \left[|\mathbf{R}, a, i\rangle \langle \mathbf{R}, a, 0| + \sum_{j \neq i} |\mathbf{R}, a, i, j\rangle \langle \mathbf{R}, a, j| \right] w_{\mathbf{R},a,i} + \text{h.c.} \quad (\text{S9.11})$$

H_0 includes the dispersion of c electrons in the AFM phase (H_c^{AFM}), and the local Hamiltonian of f electrons. H_1 corresponds to the fc hybridization term H_v . States with three or more f electrons are dropped due to their high energies. We thus write the Hamiltonian via $|\mathbf{R}, a, 0\rangle, |\mathbf{R}, a, i, j\rangle$ to reflect the fact that the new Hamiltonian does not involve the states with more than 2 electron.

Moreover, in Eq. S9.11, we have rewritten H_{loc} with operators $|\mathbf{R}, a, i\rangle, |\mathbf{R}, a, 0\rangle, |\mathbf{R}, a, i, j\rangle$. We can show that two definitions are equivalent when acting on the empty, singly occupied, and doubly occupied states. In other words,

$$H'_{loc}(\mathbf{R}, a) \sim H_{loc}[f_{\mathbf{R},a}^\dagger, f_{\mathbf{R},a}] \quad (\text{S9.12})$$

where $H'_{loc}(\mathbf{R}, a)$ has been introduced in Eq. S9.11. \sim means two Hamiltonian are equivalent when acting on the empty, singly occupied, and doubly occupied states. We prove the equivalence by showing

$$H_{loc}[f_{\mathbf{R},a}^\dagger, f_{\mathbf{R},a}] |\mathbf{R}, a, i\rangle = E_i |\mathbf{R}, a, i\rangle, \quad H'_{loc}(\mathbf{R}, a) |\mathbf{R}, a, i\rangle = \left(\sum_{i'} E_{i'} |\mathbf{R}, a, i'\rangle \langle \mathbf{R}, a, i'| \right) |\mathbf{R}, a, i\rangle = E_i |\mathbf{R}, a, i\rangle,$$

$$H_{loc}[f_{\mathbf{R},a}^\dagger, f_{\mathbf{R},a}] |\mathbf{R}, a, 0\rangle \approx \frac{U}{2} |\mathbf{R}, a, 0\rangle, \quad H'_{loc}(\mathbf{R}, a) |\mathbf{R}, a, 0\rangle = \left(\frac{U}{2} |\mathbf{R}, a, 0\rangle \langle \mathbf{R}, a, 0| \right) |\mathbf{R}, a, 0\rangle = \frac{U}{2} |\mathbf{R}, a, 0\rangle$$

$$H_{loc}[f_{\mathbf{R},a}^\dagger, f_{\mathbf{R},a}] |\mathbf{R}, a, i, j\rangle \approx \frac{U}{2} |\mathbf{R}, a, i, j\rangle, \quad H'_{loc}(\mathbf{R}, a) |\mathbf{R}, a, i, j\rangle = \left(\frac{U}{2} \sum_{i'>j'} |\mathbf{R}, a, i', j'\rangle \langle \mathbf{R}, a, i', j'| \right) |\mathbf{R}, a, i, j\rangle = \frac{U}{2} |\mathbf{R}, a, i, j\rangle \quad (\text{S9.13})$$

In the definition of H_1 in Eq. S9.11, we have also replaced $\eta_{\mathbf{R},a,i}^\dagger$ operator via

$$\tilde{\eta}_{\mathbf{R},a,i}^\dagger = |\mathbf{R}, a, i\rangle \langle \mathbf{R}, a, 0| + \sum_{j \neq i} |\mathbf{R}, a, i, j\rangle \langle \mathbf{R}, a, j| \quad (\text{S9.14})$$

We now show two definitions are equivalent when acting on the empty and singly occupied states. The equivalence can be seen by showing

$$\eta_{\mathbf{R},a,i}^\dagger |\mathbf{R}, a, 0\rangle = |\mathbf{R}, a, i\rangle, \quad \tilde{\eta}_{\mathbf{R},a,i}^\dagger |\mathbf{R}, a, 0\rangle = \left(|\mathbf{R}, a, i\rangle \langle \mathbf{R}, a, 0| \right) |\mathbf{R}, a, 0\rangle = |\mathbf{R}, a, i\rangle$$

$$\eta_{\mathbf{R},a,j}^\dagger |\mathbf{R}, a, j\rangle = |\mathbf{R}, a, i, j\rangle, \quad \tilde{\eta}_{\mathbf{R},a,i}^\dagger |\mathbf{R}, a, j\rangle = \left(|\mathbf{R}, a, i, j\rangle \langle \mathbf{R}, a, j| \right) |\mathbf{R}, a, j\rangle = |\mathbf{R}, a, i, j\rangle, \quad i \neq j \quad (\text{S9.15})$$

We can then utilize the Eq. S13.11 and Eq. S9.11 to perform Schrieffer-Wolff transformations. Since c electrons describe the low-energy gapless degrees of freedom, we always treat c electrons as our low-energy excitations. Therefore, we only rewrite f -electron operators with bra and ket notations (in Eq. S9.11), but keep using the operator formula of c electrons since it always maps a low-energy c states to another low-energy c states.

In practice, the effective Hamiltonian H_{SW} (Eq. S13.11) from Schrieffer-Wolff transformations comes from the virtual process

$$|L, J\rangle \rightarrow |H, M\rangle \rightarrow |L, I\rangle \quad (\text{S9.16})$$

where $|L, I\rangle$ labels the I -th low-energy state and $|H, M\rangle$ labels the M -th high-energy state. In the current model, only the following three types of virtual processes can be generated by H_1 (fc hybridization terms)

$$|\mathbf{R}, a, i\rangle \rightarrow |\mathbf{R}, a, 0\rangle \rightarrow |\mathbf{R}, a, j\rangle$$

$$\begin{aligned}
|\mathbf{R}, a, i\rangle &\rightarrow |\mathbf{R}, a, j, i\rangle \rightarrow |\mathbf{R}, a, i\rangle, & j \neq i \\
|\mathbf{R}, a, i\rangle &\rightarrow |\mathbf{R}, a, j, i\rangle \rightarrow |\mathbf{R}, a, j\rangle, & j \neq i
\end{aligned}
\tag{S9.17}$$

We now consider the contributions from each virtual process.

For,

$$\begin{aligned}
|L, J\rangle &= |\mathbf{R}, a, j\rangle, & |L, I\rangle &= |\mathbf{R}, a, i\rangle \\
|H, M\rangle &= |\mathbf{R}, a, 0\rangle
\end{aligned}
\tag{S9.18}$$

the contributions generated by Schrieffer-Wolff transformation (Eq. S13.11) is

$$H_{SW}^1 = \sum_{\mathbf{R}, a, i, j} \frac{1}{2} v_{a,j}^* v_{a,i} \left(\frac{1}{-\frac{U}{2}} + \frac{1}{-\frac{U}{2}} \right) |\mathbf{R}, a, i\rangle w_{\mathbf{R}, a, i} w_{\mathbf{R}, a, j}^\dagger \langle \mathbf{R}, a, j| = \frac{-2}{U} \sum_{\mathbf{R}, a, i, j} v_{a,j}^* v_{a,i} w_{\mathbf{R}, a, i} w_{\mathbf{R}, a, j}^\dagger |\mathbf{R}, a, i\rangle \langle \mathbf{R}, a, j|
\tag{S9.19}$$

When acting on the low-energy subspace (singly occupied states), we have the following equivalence

$$|\mathbf{R}, a, i\rangle \langle \mathbf{R}, a, j| \sim \eta_{\mathbf{R}, a, i}^\dagger \eta_{\mathbf{R}, a, j}
\tag{S9.20}$$

Then we have

$$H_{SW}^1 = \frac{-2}{U} \sum_{\mathbf{R}, a, i, j} v_{a,j}^* v_{a,i} w_{\mathbf{R}, a, i} w_{\mathbf{R}, a, j}^\dagger \eta_{\mathbf{R}, a, i}^\dagger \eta_{\mathbf{R}, a, j}
\tag{S9.21}$$

For

$$\begin{aligned}
|L, J\rangle &= |\mathbf{R}, a, i\rangle, & |L, I\rangle &= |\mathbf{R}, a, i\rangle \\
|H, M\rangle &= |\mathbf{R}, a, i, j\rangle
\end{aligned}
\tag{S9.22}$$

with $i \neq j$, the contributions generated by Schrieffer-Wolff transformation (Eq. S13.11) is

$$H_{SW}^2 = \sum_{\mathbf{R}, a, i, j \neq i} \frac{1}{2} v_{a,j}^* v_{a,i} \left(\frac{1}{-\frac{U}{2}} + \frac{1}{-\frac{U}{2}} \right) w_{\mathbf{R}, a, j}^\dagger |\mathbf{R}, a, i\rangle \langle \mathbf{R}, a, i| w_{\mathbf{R}, a, j} = \frac{-2}{U} \sum_{\mathbf{R}, a, i, j \neq i} v_{a,j}^* v_{a,i} w_{\mathbf{R}, a, j}^\dagger w_{\mathbf{R}, a, j} |\mathbf{R}, a, i\rangle \langle \mathbf{R}, a, i|
\tag{S9.23}$$

When acting on the low-energy subspace (singly occupied states), we have the following equivalence

$$\sum_i (1 - \delta_{i,j}) |\mathbf{R}, a, i\rangle \langle \mathbf{R}, a, i| \sim \eta_{\mathbf{R}, a, j} \eta_{\mathbf{R}, a, j}^\dagger
\tag{S9.24}$$

This can be seen from

$$\begin{aligned}
\left(\sum_i (1 - \delta_{i,j}) |\mathbf{R}, a, i\rangle \langle \mathbf{R}, a, i| \right) |\mathbf{R}, a, j\rangle &= 0, & \eta_{\mathbf{R}, a, j} \eta_{\mathbf{R}, a, j}^\dagger |\mathbf{R}, a, j\rangle &= 0 \\
\left(\sum_i (1 - \delta_{i,j}) |\mathbf{R}, a, i\rangle \langle \mathbf{R}, a, i| \right) |\mathbf{R}, a, i'\rangle &= |\mathbf{R}, a, i'\rangle, & \eta_{\mathbf{R}, a, j} \eta_{\mathbf{R}, a, j}^\dagger |\mathbf{R}, a, i'\rangle &= |\mathbf{R}, a, i'\rangle, & \text{for } i' \neq j
\end{aligned}
\tag{S9.25}$$

Then we have

$$H_{SW}^2 = \frac{-2}{U} \sum_{\mathbf{R}, a, j} v_{a,j}^* v_{a,j} w_{\mathbf{R}, a, j} w_{\mathbf{R}, a, j}^\dagger \eta_{\mathbf{R}, a, j} \eta_{\mathbf{R}, a, j}^\dagger
\tag{S9.26}$$

For

$$\begin{aligned}
|L, J\rangle &= |\mathbf{R}, a, j\rangle, & |L, I\rangle &= |\mathbf{R}, a, i\rangle \\
|H, M\rangle &= |\mathbf{R}, a, i, j\rangle
\end{aligned}
\tag{S9.27}$$

with $i \neq j$, the contributions generated by Schrieffer-Wolff transformation (Eq. S13.11) is

$$\begin{aligned} H_{SW}^3 &= \sum_{\mathbf{R}, a, i \neq j} \frac{1}{2} v_{a,j}^* v_{a,i} \left(\frac{1}{-\frac{U}{2}} + \frac{1}{-\frac{U}{2}} \right) (-1) w_{\mathbf{R}, a, j}^\dagger |\mathbf{R}, a, i\rangle \langle \mathbf{R}, a, j| w_{\mathbf{R}, a, i} \\ &= \frac{2}{U} \sum_{\mathbf{R}, a, i \neq j} v_{a,j}^* v_{a,i} w_{\mathbf{R}, a, j}^\dagger w_{\mathbf{R}, a, i} |\mathbf{R}, a, i\rangle \langle \mathbf{R}, a, j| \end{aligned} \quad (\text{S9.28})$$

where the additional minus sign can be seen from the definition of H_1 (Eq. S9.11), and the fact that $|\mathbf{R}, a, i, j\rangle = -|\mathbf{R}, a, j, i\rangle$. When acting on the low-energy subspace (singly occupied states), we have the following equivalence

$$|\mathbf{R}, a, i\rangle \langle \mathbf{R}, a, j| \sim \eta_{\mathbf{R}, a, i}^\dagger \eta_{\mathbf{R}, a, j} \quad (\text{S9.29})$$

Then we have

$$H_{SW}^3 = \frac{2}{U} \sum_{\mathbf{R}, a, i \neq j} v_{a,j}^* v_{a,i} w_{\mathbf{R}, a, j}^\dagger w_{\mathbf{R}, a, i} \eta_{\mathbf{R}, a, i}^\dagger \eta_{\mathbf{R}, a, j} \quad (\text{S9.30})$$

We can combining all three contributions (Eq. S9.21, Eq. S9.26, Eq. S9.26), and find

$$H_{SW} = H_{SW}^1 + H_{SW}^2 + H_{SW}^3 = -\frac{2}{U} \sum_{\mathbf{R}, a, i, j} v_{a,j}^* v_{a,i} \left(\eta_{\mathbf{R}, a, i}^\dagger w_{\mathbf{R}, a, i} w_{\mathbf{R}, a, j}^\dagger \eta_{\mathbf{R}, a, j} + w_{\mathbf{R}, a, j}^\dagger \eta_{\mathbf{R}, a, j} \eta_{\mathbf{R}, a, i}^\dagger w_{\mathbf{R}, a, i} \right) \quad (\text{S9.31})$$

The low-energy effective Hamiltonian, which describes a Kondo lattice model, now becomes

$$\begin{aligned} H_{KL} &= H_c^{AFM} + H_{\text{Kondo}} + H_{f,0} \\ H_{\text{Kondo}} = H_{SW} &= \frac{-2}{U} \sum_{\mathbf{R}} \sum_a \sum_{i,j} v_{a,i}^* v_{a,j} \left(\eta_{\mathbf{R}, a, j}^\dagger w_{\mathbf{R}, a, j} w_{\mathbf{R}, a, i}^\dagger \eta_{\mathbf{R}, a, i} + w_{\mathbf{R}, a, i}^\dagger \eta_{\mathbf{R}, a, i} \eta_{\mathbf{R}, a, j}^\dagger w_{\mathbf{R}, a, j} \right) \\ H_{f,0} &= \sum_{\mathbf{R}, a, i} E_i \eta_{\mathbf{R}, a, i}^\dagger \eta_{\mathbf{R}, a, i} \end{aligned} \quad (\text{S9.32})$$

where the Kondo coupling term comes from the Schrieffer-Wolff transformations. $H_{f,0}$ is the atomic Hamiltonian of f electrons. We can obtain it by noting the following equivalence (when acting on the low-energy singly occupied states)

$$E_i |\mathbf{R}, a, i\rangle \langle \mathbf{R}, a, i| \sim E_i \eta_{\mathbf{R}, a, i}^\dagger \eta_{\mathbf{R}, a, i} \quad (\text{S9.33})$$

Since the Hamiltonian is defined in the low-energy subspace with singly occupied f states. Therefore, we also introduce the following constraints (which enforce the filling of f electrons of each Ce atom to be 1)

$$\sum_i \eta_{\mathbf{R}, a, i}^\dagger \eta_{\mathbf{R}, a, i} = 1 \quad (\text{S9.34})$$

2. Mean-field theory of Kondo phase

To understand the Kondo effect, we perform mean-field calculations on the Hamiltonian defined in Eq. S9.32. In this section, we briefly describe the mean-field approach.

We first rewrite the Kondo coupling term in the conventional ordering ($\eta^\dagger \eta w^\dagger w$)

$$\begin{aligned} H_{\text{Kondo}} &= \frac{-2}{U} \sum_{\mathbf{R}} \sum_{a, i, j} v_{a,i}^* v_{a,j} \left[\eta_{\mathbf{R}, a, j}^\dagger \eta_{\mathbf{R}, a, i} (A_{\mathbf{R}a j, \mathbf{R}a i} - w_{\mathbf{R}, a, i}^\dagger w_{\mathbf{R}, a, j}) + (\delta_{i,j} - \eta_{\mathbf{R}, a, j}^\dagger \eta_{\mathbf{R}, a, i}) w_{\mathbf{R}, a, i}^\dagger w_{\mathbf{R}, a, j} \right] \\ &= \frac{4}{U} \sum_{\mathbf{R}} \sum_{a, i, j} v_{a,i}^* v_{a,j} \eta_{\mathbf{R}, a, j}^\dagger \eta_{\mathbf{R}, a, i} w_{\mathbf{R}, a, i}^\dagger w_{\mathbf{R}, a, j} - \frac{2}{U} \sum_{\mathbf{R}} \sum_{a, i, j} v_{a,i}^* v_{a,j} A_{\mathbf{R}a j, \mathbf{R}a i} \eta_{\mathbf{R}, a, j}^\dagger \eta_{\mathbf{R}, a, i} - \frac{2}{U} \sum_{\mathbf{R}} \sum_{a, i} v_{a,i}^* v_{a,i} w_{\mathbf{R}, a, i}^\dagger w_{\mathbf{R}, a, i} \end{aligned} \quad (\text{S9.35})$$

where the first term describes a four-fermion Kondo interaction term, and the remaining two terms are one-body terms.

We can then perform a mean-field decoupling of H_{Kondo}

$$\begin{aligned}
H_{\text{Kondo}}^{MF} = & -\frac{4}{U} \sum_{\mathbf{R}} \sum_{i,j,a} v_{a,i}^* v_{a,j} \left(\chi_{\eta w,a,j} w_{\mathbf{R},a,i}^\dagger \eta_{\mathbf{R},a,i} + \chi_{w\eta,a,i} \eta_{\mathbf{R},a,j}^\dagger w_{\mathbf{R},a,j} \right. \\
& \left. - \chi_{\eta\eta,a,j} w_{\mathbf{R},a,i}^\dagger w_{\mathbf{R},a,j} - \chi_{w w,a,i,j} \eta_{\mathbf{R},a,j}^\dagger \eta_{\mathbf{R},a,i} - \chi_{\eta w,a,j} \chi_{w\eta,a,i} + \chi_{\eta\eta,a,j} \chi_{w w,a,i,j} \right) \\
& + \frac{-2}{U} \sum_{\mathbf{R}} \sum_{i,j,a} v_{a,i}^* v_{a,j} A_{\mathbf{R}aj,\mathbf{R}ai} \eta_{\mathbf{R},a,j}^\dagger \eta_{\mathbf{R},a,i} + \frac{-2}{U} \sum_{\mathbf{R}} \sum_i v_{a,i}^* v_{a,i} w_{\mathbf{R},a,i}^\dagger w_{\mathbf{R},a,i}
\end{aligned} \tag{S9.36}$$

where the mean-fields are

$$\begin{aligned}
\chi_{\eta w,a,i} &= \frac{1}{N} \sum_{\mathbf{R}} \langle \eta_{\mathbf{R},a,i}^\dagger w_{\mathbf{R},a,i} \rangle \\
\chi_{w\eta,a,i} &= \frac{1}{N} \sum_{\mathbf{R}} \langle w_{\mathbf{R},a,i}^\dagger \eta_{\mathbf{R},a,i} \rangle = \chi_{\eta w,a,i}^* \\
\chi_{w w,a,i,j} &= \frac{1}{N} \sum_{\mathbf{R}} \langle w_{\mathbf{R},a,i}^\dagger w_{\mathbf{R},a,j} \rangle \\
\chi_{\eta\eta,a,i,j} &= \frac{1}{N} \sum_{\mathbf{R}} \langle \eta_{\mathbf{R},a,i}^\dagger \eta_{\mathbf{R},a,j} \rangle
\end{aligned} \tag{S9.37}$$

In addition, we also introduce the Lagrangian multiplier λ_a to enforce the following filling constraints of f electrons (see Eq. S9.34)

$$\frac{1}{N} \sum_{\mathbf{R},i} \langle \eta_{\mathbf{R},a,i}^\dagger \eta_{\mathbf{R},a,i} \rangle = 1 \tag{S9.38}$$

This leads to the following mean-field Hamiltonian

$$\begin{aligned}
H^{MF} &= H_c + H_{\text{Kondo}}^{MF} + H'_f \\
H'_f &= \sum_{\mathbf{R},a,i} E_i \eta_{\mathbf{R},a,i}^\dagger \eta_{\mathbf{R},a,i} + \sum_{\mathbf{R},a} \lambda_a \left(\sum_i \eta_{\mathbf{R},a,i}^\dagger \eta_{\mathbf{R},a,i} - 1 \right)
\end{aligned} \tag{S9.39}$$

The expectation values $\langle \rangle$ in Eq. S9.37 and Eq. S9.38 are taken with respect to the ground state of the mean-field Hamiltonian H^{MF} . The mean-field equations (Eq. S9.37) and the filling constraints (Eq. S9.38) are then solved self-consistently [116].

At the mean-field level, the development of the Kondo effect is characterized by

$$\chi_{\eta w,a,i} \neq 0 \tag{S9.40}$$

or equivalently $\chi_{w\eta,a,i} \neq 0$. Whenever $\chi_{\eta w,a,i} \neq 0$, f electron hybridizes with c electron and becomes an effective itinerant degree of freedom.

Appendix X: Kondo effect in the AFM phase

In this section, we demonstrate even with AFM ordering of c electrons a Kondo effect can still develop. Due to the existence of $P \cdot \mathcal{T}$ symmetry in the AFM phase (where P denotes inversion symmetry and \mathcal{T} denotes time-reversal symmetry), c electrons can still form two-fold degenerate Kramers' doublets. The doublets of c electrons can then screen the f -local moments.

We first illustrate the formation of the Kondo singlet in the AFM phase via a three-site spinful toy model. The Hamiltonian of the toy model is

$$H = \sum_{i=1,2,\sigma} (-\mu) c_{i,\sigma}^\dagger c_{i,\sigma} + \sum_{\sigma_1,\sigma_2} m_z (c_{1,\sigma_1}^\dagger \sigma_{\sigma_1\sigma_2}^z c_{1,\sigma_2} - c_{2,\sigma_1}^\dagger \sigma_{\sigma_1\sigma_2}^z c_{2,\sigma_2}) + J \sum_{i,j,\mu} S^\mu c_{i,\sigma} \sigma_{\sigma,\sigma'}^\mu c_{j,\sigma'}. \tag{S10.1}$$

$c_{i,\sigma}$ describes two c electrons that develop an antiferromagnetic order as characterized by a non-zero m_z . Two c electrons couple to the f local moment S^μ via a Kondo coupling term ($J > 0$). We can observe that c electrons develop an AFM order due to the m_z term which splits the energy of spin \uparrow and spin \downarrow states of c electrons at the same site. However, due to the existence

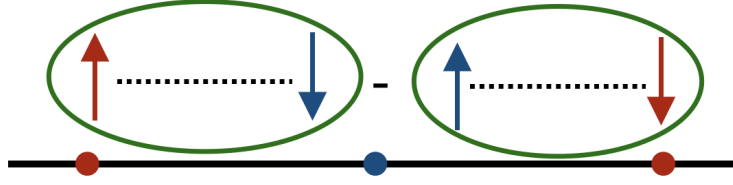


Figure S15. Illustration of the Kondo effect in the AFM phase. Red arrows denote the spins of c electrons, and blue arrows denote the spins of f electrons. The ground state is a Kondo-singlet state (Eq. S10.2).

of the $P \cdot \mathcal{T}$ symmetry, $c_{1,\uparrow}$ and $c_{2,\downarrow}$ electrons are still degenerate (similarly, $c_{1,\downarrow}$ and $c_{2,\uparrow}$ electrons are also degenerate). This degeneracy allows the formation of the Kondo singlet. For example, when $c_{\mathbf{R},1,\uparrow}$ and $c_{\mathbf{R},2,\downarrow}$ electrons are close to the Fermi energy (this can be realized by setting $\mu \sim m_z$), the many-body ground state of Hamiltonian in Eq. S10.1 is a Kondo singlet and can be written as (in the limit of large magnetic ordering $\mu = m_z \rightarrow \infty$)

$$|KS\rangle = \frac{c_{\mathbf{R},1,\uparrow}^\dagger f_{\mathbf{R},\downarrow}^\dagger - c_{\mathbf{R},2,\downarrow}^\dagger f_{\mathbf{R},\uparrow}^\dagger}{\sqrt{2}} |0\rangle \quad (\text{S10.2})$$

as also illustrated in Fig. S15. Clearly, such formation of the Kondo singlet is not affected by the AFM ordering and only relies on the existence of $P \cdot \mathcal{T}$ symmetry.

For what follows, we will show that a similar mechanism can be applied to the CeCo_2P_2 , where the $P \cdot \mathcal{T}$ symmetry also promotes the development of the Kondo effect.

1. Filling-enforced metallic phase of the c electrons

Besides the Kramers double, the development of the Kondo effect also requires a finite density of states of c electrons near the Fermi energy. In this section, we show that the c electron band is always metal in the AFM phase. For the symmetry group (126.386) of the AFM phase, all the spinful representations at high symmetry points A , M , R are four-dimensional. Therefore, if the total fillings of the systems n follow $n \bmod 4 \neq 0$, then the system has to be metal.

In the current model, each Ce has 11 electrons (without including the Ce f electrons which provide the local moments), each Co has 9 electrons, and each P has 5 electrons. Then, for each unit cell, we have in total $11 \times 2 + 9 \times 4 + 5 \times 4 = 78$ where $78 \bmod 4 = 2 \neq 0$. Then, c electrons are metallic. The filling-enforced metallic nature of the c electrons combined with the $P \cdot \mathcal{T}$ protected Kramers-doublet guarantee the development of the Kondo effect since we could always have c electron density of states near the Fermi energy no matter how strong the magnetic order is.

2. $P \cdot \mathcal{T}$ symmetry and the Kondo effect in the AFM phase

We now show the robustness of our Kondo phase against AFM ordering. In this section, we consider the conventional cell of the PM phase, which is equivalent to the primitive cell of the AFM phase. We start with the following simplified Kondo lattice model

$$H_{KL} = H_c^{\text{AFM}} + H_{\text{Kondo}} + H_{f,0} \quad (\text{S10.3})$$

For the c -electron part, we take the simplified two-orbital model that we introduced in Sec. V with an additional mean-field term that describes the magnetic ordering

$$H_c^{\text{AFM}} = H_c + H_{c,MF} \quad (\text{S10.4})$$

where H_c is the non-interacting part of the Co ($d_{x^2-y^2}$, d_{z^2}) orbitals introduced in Eq. S5.1 and $H_{c,MF}$ denotes the mean-field contributions that describes the AFM ordering

$$H_{c,MF} = U_d m \sum_{\mathbf{R}, a, i, \sigma} s(\mathbf{R} + \mathbf{r}_a) \left(\sigma c_{\mathbf{R}, a, i, \sigma}^\dagger c_{\mathbf{R}, a, i, \sigma} \right) \quad (\text{S10.5})$$

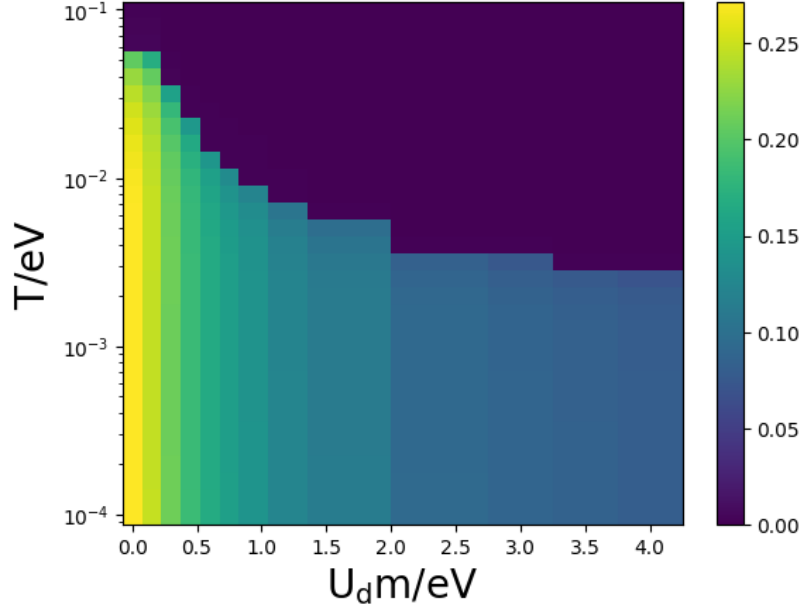


Figure S16. Maximum value of hybridization fields ($\max|\chi_{\eta w}|$) at various temperatures and tuning parameters $U_d m$.

$s(\mathbf{R} + \mathbf{r}_a) = \pm 1$ for the electrons of the $\text{Co}_{1,2}$ ($\text{Co}_{3,4}$) atoms. m is the mean-field parameter of the AFM order, and U_d is the strength of Coulomb repulsion. Since the Hamiltonian in Eq. S10.5 only depends on the product of m and U_d , we will treat $U_d m$ as our tuning parameters here. As we increase $U_d m$, the magnetic ordering of d orbitals becomes stronger.

For the f electron, we will only keep the lowest two-fold degenerate f electron states of the atomic problem to simplify the considerations (see Sec. VIII). Then we have

$$H_{f,0} = \sum_{\mathbf{R}} E_1 (\eta_{\mathbf{R},1}^\dagger \eta_{\mathbf{R},1} + \eta_{\mathbf{R},2}^\dagger \eta_{\mathbf{R},2}) \quad (\text{S10.6})$$

The Kondo coupling is derived from the Schrieffer-Wolff transformation (Sec XIII) with the nearest-neighbor coupling between $\eta_{\mathbf{R},1}$, $\eta_{\mathbf{R},2}$ and $d_{x^2-y^2}$, d_{z^2} states.

We then use the mean-field approaches (Sec. IX 2) to solve the Kondo Hamiltonian by fixing the filling of f electrons to be 1 for each Ce atom. For the d electrons, each unit cell contains 4 Co atoms, each Co atom has 2 d orbitals, and each d orbital has 2 spin flavors. This results in a total of $4 \times 2 \times 2 = 16$ d orbitals per unit cell (conventional cell of the PM phase). We then fill 14 d electrons per unit cell. We treat mU_d as the tuning parameters and solve the mean-field theory at Kondo coupling strength $J_K = t^2/U = 0.1\text{eV}$ (with t denoting the nearest-neighbor hybridization between $d_{x^2-y^2}$ orbitals and $\eta_{1/2}$ f orbitals) and at different temperatures. We show the evolution of the mean fields (f expectation value) $\max|\chi_{\eta w}|$ in Fig. S16. We can observe that, even with strong magnetic ordering (large Um_d), a non-zero Kondo temperature (the highest temperature where we have a non-zero $|\chi_{\eta w}|$) could always be found.

We emphasize that even though the strong magnetic ordering splits the spin σ states and spin $-\sigma$ states of the d electrons from the same Co layer. The spin σ states of one Co layer and the spin $-\sigma$ states of the nearby Co layer are still degenerate due to $P \cdot \mathcal{T}$ symmetry. These degenerate Kramer-doublet states are unaffected by the magnetic ordering and promote the formation of the Kondo effect.

Moreover, due to the presence of the $P \cdot \mathcal{T}$ symmetry, magnetic ordering of the c electrons does not induce magnetic ordering of the f electrons. This contrasts with the conventional expectation, where c -electron magnetism can induce f -electron magnetic order through a Hartree-Fock contribution. In our case, the site symmetry group of Ce atom has a $P \cdot \mathcal{T}$ symmetry with

$$P \cdot \mathcal{T} \mathbf{J}_{\mathbf{R},a}^\mu (P \cdot \mathcal{T})^{-1} = -\mathbf{J}_{\mathbf{R},a}^\mu, \quad (\text{S10.7})$$

where $\mathbf{J}_{\mathbf{R},a}^\mu$ denotes the total angular momentum of the f electrons at site \mathbf{R} and sublattice $a \in \{\text{Ce}_1, \text{Ce}_2\}$. As a result, the expectation value $\langle \mathbf{J}_{\mathbf{R},a}^\mu \rangle$ must vanish as long as the $P \cdot \mathcal{T}$ symmetry is preserved. In other words, the magnetic ordering of the c electrons, which respects the $P \cdot \mathcal{T}$ symmetry, cannot induce a magnetic order in the f electrons. This is also important for the formation of the Kondo effect, since the magnetic ordering of f electrons will also suppress the Kondo effect.

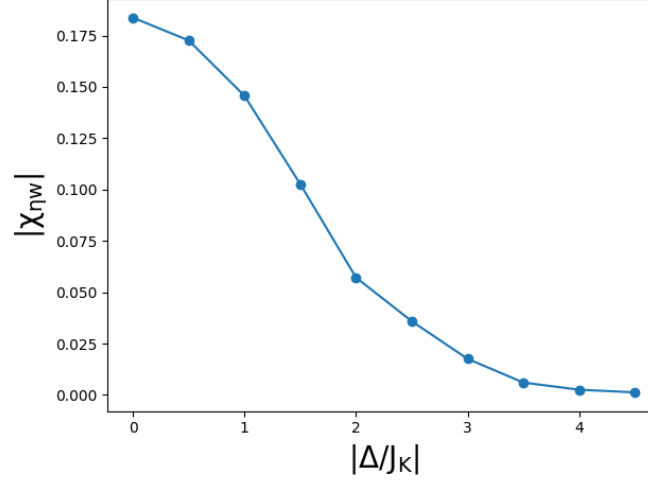


Figure S17. Maximum value of hybridization strength at fixed $\beta = 10^3 \text{ eV}^{-1}$ and $U_d m = 1 \text{ eV}$, and various $P \cdot \mathcal{T}$ symmetry breaking strength Δ (normalized by the Kondo coupling strength J_K).

For the purpose of discussion, we also consider the case in which the $P \cdot \mathcal{T}$ symmetry is broken. We consider the following term, which introduce an energy degeneracy of Co d electrons between different layers and breaks the $P \cdot \mathcal{T}$ symmetry:

$$H_{c,\Delta} = \Delta \sum_{\mathbf{R},\sigma,i} \left(\sum_{a \in \{Co_1, Co_2\}} c_{\mathbf{R},a,i,\sigma}^\dagger c_{\mathbf{R},a,i,\sigma} - \sum_{a \in \{Co_3, Co_4\}} c_{\mathbf{R},a,i,\sigma}^\dagger c_{\mathbf{R},a,i,\sigma} \right) \quad (\text{S10.8})$$

We perform calculations with varying strengths of $P \cdot \mathcal{T}$ symmetry breaking, in the low-temperature limit $\beta = 10^3 \text{ eV}^{-1}$, and with a fixed magnetic ordering strength of $mU_d = 1.0 \text{ eV}$. The result is shown in Fig. S17, where we observe that a finite Δ gradually reduces the hybridization strength and finally destroys the Kondo effect at sufficiently large symmetry breaking term.

3. Development of Kondo effect in the DFT model

In the previous section, we demonstrated the stability of Kondo effect against magnetic order in a simplified model that only considered two d orbitals of Co atoms and spin-1/2 states of the f orbitals. In this section, we support our previous findings by including all the c -electron orbitals (d orbitals of Ce atoms, d orbitals of Co atoms, p orbitals of P atoms) and all the f orbitals. The model we study takes the same formula as Eq. S10.3 which is

$$H_{KL} = H_c^{\text{AFM}} + H_{\text{Kondo}} + H_{f,0} \quad (\text{S10.9})$$

H_c^{AFM} is derived from DFT calculations in the AFM phase with all c electron orbitals being considered. H_{Kondo} is obtained from the Srieffer Wolff transformations (Sec. XIII) using the the parameters obtained from DFT calculations. $H_{f,0}$ is the atomic Hamiltonian obtained DFT calculations where all f orbitals have been included as we introduced in Eq. S9.32.

To investigate the Kondo effect, we first study the hybridization function. For the single-orbital Anderson model defined as

$$H_{\text{single-orbital Anderson}} = \sum_{\mathbf{k},\sigma} \epsilon_{\mathbf{k}} c_{\mathbf{k},\sigma}^\dagger c_{\mathbf{k},\sigma} + V \sum_{\mathbf{R},\sigma} (c_{\mathbf{k},\sigma}^\dagger f_{\mathbf{k},\sigma} + \text{h.c.}) + \sum_{\mathbf{R}} \frac{U}{2} \left(\sum_{\sigma} f_{\mathbf{R},\sigma}^\dagger f_{\mathbf{R},\sigma} - 1 \right)^2, \quad (\text{S10.10})$$

we can introduce the following hybridization function [76]

$$\Delta(\epsilon) = \frac{1}{N} \pi \sum_{\mathbf{k}} |V|^2 \delta(\epsilon - \epsilon_{\mathbf{k}}) = \pi V^2 \rho(\epsilon) \quad (\text{S10.11})$$

V is the fc hybridization strength, $\epsilon_{\mathbf{k}}$ is the dispersion of the conduction electrons (in the non-Kondo phase), N is the total number of unit cells, and $\rho(\epsilon)$ is the density of states of c electron bands. Physically, we can observe that the hybridization function is proportional to the density of states of c electrons and the square of hybridization strength between f and c electrons. Thus it effectively characterizes the strength of the Kondo effect [76].

We can generalize the hybridization function to the multi-orbital case. To do so, we first rewrite the Kondo hybridization in the momentum space (Eq. S9.7), which gives

$$H_V = \sum_{\mathbf{k}, ab, i, j, \sigma} V_{ai, bj\sigma}(\mathbf{k}) \eta_{\mathbf{k}, a, i}^\dagger c_{\mathbf{k}, b, j, \sigma} + \text{h.c.}, \quad V_{ai, bj\sigma}(\mathbf{k}) = \sum_{\Delta \mathbf{R}} V_{ai, bj\sigma}(\Delta \mathbf{R}) e^{-i\mathbf{k} \cdot (\Delta \mathbf{R} + \mathbf{r}_b - \mathbf{r}_a)} \quad (\text{S10.12})$$

We also introduce the band basis of c electrons

$$H_c^{AFM} = \sum_{\mathbf{k}, n} \epsilon_{\mathbf{k}, n} \gamma_{\mathbf{k}, n}^\dagger \gamma_{\mathbf{k}, n}, \quad \gamma_{\mathbf{k}, n} = \sum_{bj\sigma} U_{bj\sigma, n}^{c, *}(\mathbf{k}) c_{\mathbf{k}, bj\sigma}. \quad (\text{S10.13})$$

We then generalize the single-orbital formula of the hybridization function to the multi-orbital formula by considering the contributions from each orbital

$$\Delta_{ai, bj\sigma}(\omega) = \frac{\pi}{N} \sum_{\mathbf{k}, n} |V_{ai, bj\sigma}(\mathbf{k})|^2 \left(|U_{bj\sigma, n}^c(\mathbf{k})|^2 \delta(\epsilon - \epsilon_{\mathbf{k}, n}) \right) \quad (\text{S10.14})$$

$|V_{ai, bj\sigma}(\mathbf{k})|^2$ is the square of the momentum-dependent hybridization strength between $\eta_{\mathbf{k}, ai}$ and $c_{\mathbf{k}, bj\sigma}$. $|U_{bj\sigma, n}^c(\mathbf{k})|^2$ denotes the orbital weight of $c_{\mathbf{k}, bj\sigma}$ electrons. We comment that, the strength of Kondo effect is related to both the density of states of c electrons and the hybridization strength between f and c electrons. We therefore can construct the hybridization function $\Delta_{ai, bj\sigma}$ by combining the density of states and hybridization strength. Therefore, $\Delta_{ai, bj\sigma}$ characterizes the strength of the Kondo effect.

We now discuss the properties of $\Delta_{ai, bj\sigma}(\omega)$. We focus on $\{\eta_{\mathbf{R}, i, a}\}_{i=1,2,3,4,5,6}$ fermions which corresponds to the low energy f states with $J = 5/2$. f states with $J = 7/2$ have much higher energy (0.3eV higher) due to the spin-orbit coupling terms and are less relevant to the Kondo effect. As for the c electrons, we separate c electrons into three sets based on their orbital and sublattice indices

$$\begin{aligned} S_I &= \{(a, i) | a \in \{Co_1, Co_2, P_1, P_2\}\} \\ S_{II} &= \{(a, i) | a \in \{Co_3, Co_4, P_3, P_4\}\} \\ S_{III} &= \{(a, i) | a \in \{Ce_1, Ce_2\}\}. \end{aligned} \quad (\text{S10.15})$$

Electrons of set I correspond to one Co-P layer (layer I) and develop ferromagnetism within this layer. Electrons of set II correspond to another Co-P layer (layer II) and develop ferromagnetism within this layer, but with opposite spin directions compared to the electrons in layer I (Fig. S4). Electrons of set III correspond to the d electrons of Ce, which do not develop magnetic order.

We now discuss the hybridization strength between each set of c electrons and the low-energy $\{\eta_{\mathbf{R}, i, a}\}_{i=1,2,3,4,5,6}$ fermions. We let

$$\begin{aligned} \Delta_{I\uparrow}(\omega) &= \sum_{i \in \{1, \dots, 6\}, bj \in S_I} \Delta_{(Ce_a, i), bj\uparrow}(\omega), & \Delta_{I\downarrow}(\omega) &= \sum_{i \in \{1, \dots, 6\}, bj \in S_I} \Delta_{(Ce_a, i), bj\downarrow}(\omega) \\ \Delta_{II\uparrow}(\omega) &= \sum_{i \in \{1, \dots, 6\}, bj \in S_{II}} \Delta_{(Ce_a, i), bj\uparrow}(\omega), & \Delta_{II\downarrow}(\omega) &= \sum_{i \in \{1, \dots, 6\}, bj \in S_{II}} \Delta_{(Ce_a, i), bj\downarrow}(\omega) \\ \Delta_{III\uparrow}(\omega) &= \sum_{i \in \{1, \dots, 6\}, bj \in S_{III}} \Delta_{(Ce_a, i), bj\uparrow}(\omega), & \Delta_{III\downarrow}(\omega) &= \sum_{i \in \{1, \dots, 6\}, bj \in S_{III}} \Delta_{(Ce_a, i), bj\downarrow}(\omega) \end{aligned} \quad (\text{S10.16})$$

As shown in Fig. S18 (a), we observe that, due to the magnetic ordering, the contribution from spin \uparrow electrons and spin \downarrow electrons from the same Co-P layers are different, where the contribution from one of the spin sectors is suppressed. However, contributions from the set I electrons of spin \uparrow and the set II electrons of spin \downarrow are degenerate due to the $P \cdot \mathcal{T}$ symmetry. These contributions are also most relevant. Moreover, the contribution from Ce d electrons are less relevant.

In conclusion, we find that spin \uparrow c electrons of layer I Co-P atoms and spin \downarrow electrons of layer II Co-P atoms, which correspond to the majority carriers of the systems near the Fermi energy, are mostly relevant to the Kondo effect. These two types of electrons are degenerate due to $P \cdot \mathcal{T}$ symmetry which favors the formation of Kondo singlet, and their degeneracy is not affected by the magnetic ordering as long as $P \cdot \mathcal{T}$ symmetry is preserved.

To demonstrate the existence of the Kondo phase, we perform mean-field calculations at a relatively large Hubbard interaction of f electrons ($U = 12\text{eV}$). This value is much larger than the maximum hopping strength of the systems (~ 1 eV) and is comparable to the typical value of the Hubbard interactions for f electrons (~ 10 eV). To show the development of the Kondo effect, we perform calculations at various temperatures. We use $\chi_{\eta w, a, i}$ (as defined in Eq. S9.37) to characterize the strength of the Kondo effect. Whenever a non-zero $\chi_{\eta w, a, i}$ develops, the Kondo effect emerges. In Fig. S18 (b), we show the

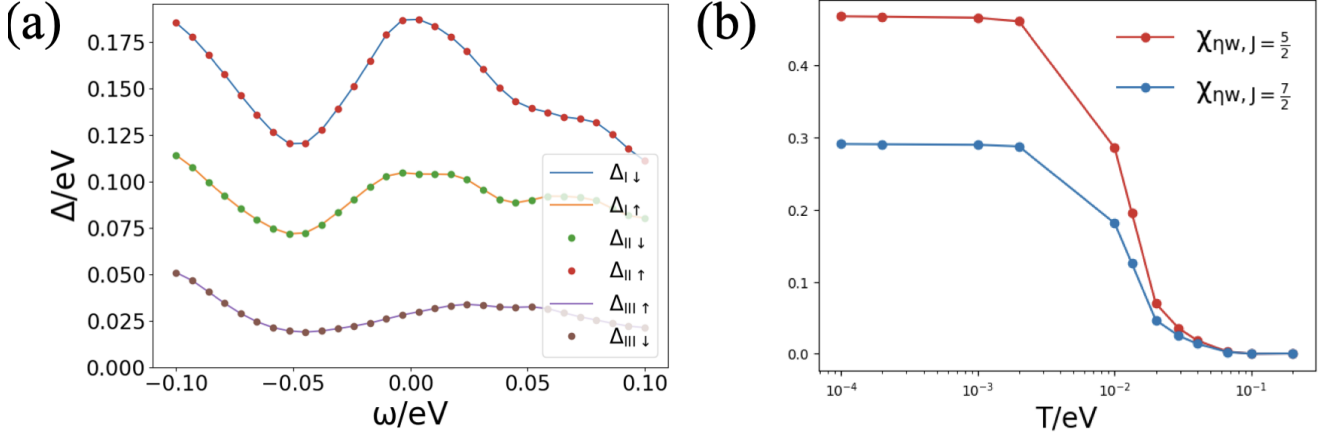


Figure S18. (Left) Hybridization functions from different c -electron channels (Eq. S10.16). (Right) Evolution of the hybridization fields as a function of temperature.

evolution of $\chi_{\eta w, J=5/2}, \chi_{\eta w, J=7/2}$ as a function of temperature. $\chi_{\eta w, J=5/2}, \chi_{\eta w, J=7/2}$ denote the contributions from $J = \frac{5}{2}$ f states (corresponding to $\eta_{\mathbf{R}, a, i=1, \dots, 6}$ fermions) and $J = \frac{7}{2}$ f states (corresponding to $\eta_{\mathbf{R}, a, i=7, \dots, 14}$ fermions) respectively

$$\begin{aligned} \chi_{\eta w, J=\frac{5}{2}} &= \sum_{j=1,2,3,4,5,6} |\chi_{\eta, w, C e_a, i}| \\ \chi_{\eta w, J=\frac{7}{2}} &= \sum_{j=7,8,9,10,11,12,13,14} |\chi_{\eta, w, C e_a, i}| \end{aligned} \quad (\text{S10.17})$$

with $\chi_{\eta w, a, i}$ defined in Eq. S9.37.

From Fig. S18 (b), we can observe, that the system starts to develop the Kondo effect at around $T \sim 0.1\text{eV}$. However, since mean-field calculations usually underestimate quantum fluctuations, the Kondo temperature of the real system will be much smaller. We also observe that both $J = 5/2, J = 7/2$ states contribute to the formation of Kondo states. Since $J = 5/2$ states have lower energy at the atomic limit (due to spin-orbit coupling, Sec. VIII 2), they are more relevant to the Kondo effect and their contributions are stronger.

At low temperatures, after the development of Kondo state, additional f -based excitations emerge. In Fig. S19, we show the band structure of the low-temperature Kondo phase by diagonalizing the mean-field Kondo Hamiltonian (Eq. S9.39). We can observe the presence of the Kondo excitation (marked by red dots). We observe two sets of Kondo bands (one near Fermi energy and the other one near $E \sim 0.3\text{eV}$). The first set of Kondo bands corresponds to the $J = \frac{5}{2}$ f -electron states whereas the second set of Kondo bands corresponds to the $J = \frac{7}{2}$ f -electron states. As we discussed in Sec. VIII 2, the energy gap between $J = \frac{5}{2}$ and $J = \frac{7}{2}$ states in the atomic limit is created by spin-orbit coupling. The value of this SOC gap in the atomic limit is $\sim \frac{7\lambda}{2} \approx 0.3\text{eV}$ which is also consistent with the band structures shown in Fig. S19.

4. Hybridization function

In this section, we further investigate the hybridization function by comparing our system with the well-studied heavy-fermion compound CeCoIn_5 . By analyzing the hybridization functions of CeCo_2P_2 and CeCoIn_5 , we find that the relatively high Kondo temperatures observed in CeCo_2P_2 can be attributed to its stronger hybridization strength.

Our focus is on the hybridization function associated with the low-energy f -electron state characterized by total angular momentum $J = 5/2$. For CeCo_2P_2 , the corresponding hybridization function can be obtained as follows:

$$\Delta_{J=5/2}(\omega) = \frac{\pi}{N} \sum_{a, i=1, \dots, 6} \delta_{a, C e_1} \sum_{\mathbf{k}, n} \left| \sum_{b, j, \sigma} V_{ai, bj\sigma}(\mathbf{k}) U_{bj\sigma, n}^c(\mathbf{k}) \right|^2 \delta(\epsilon - \epsilon_{\mathbf{k}, n}) \quad (\text{S10.18})$$

Here, $V_{ai, bj\sigma}(\mathbf{k})$ denotes the fc hybridization, and $U_{bj\sigma, n}^c(\mathbf{k})$ are the eigenvectors of the c -electron bands, as defined in Eqs. (S10.12) and (S10.13). We consider only the contributions from the Ce_1 atom, since both Ce atoms are equivalent. Furthermore, we restrict the analysis to the lowest 6 f -electron states with total angular momentum $J = 5/2$. The equivalent hybridization function for the $J = 5/2$ f -orbitals in CeCoIn_5 can be defined in the same manner.

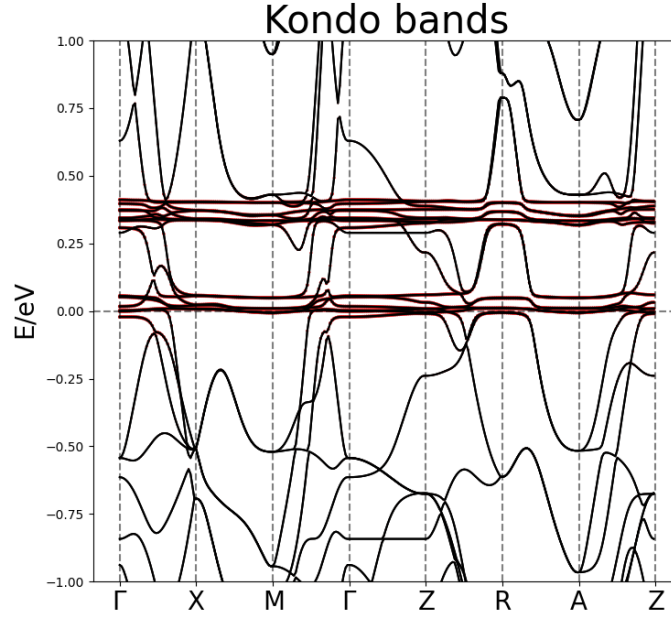


Figure S19. Band structure in the Kondo phase ($T = 10^{-4}$ eV), where red dots mark the orbital weights of f electrons.

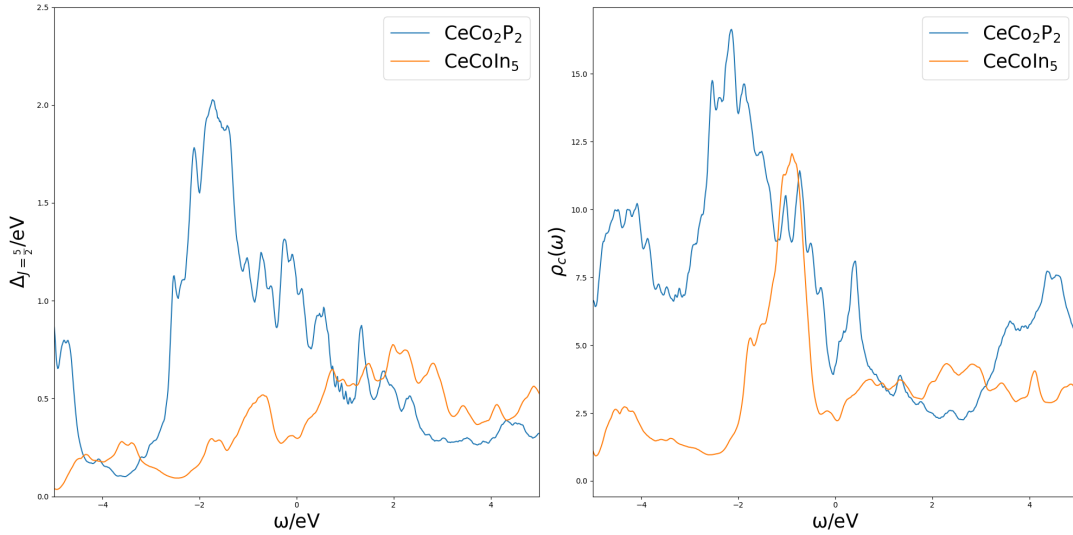


Figure S20. (Left) Hybridization functions of the CeCo_2P_2 in the AFM phase, and CeCoIn_5 . (Right) Conduction electron density of states of CeCo_2P_2 in the AFM phase, and CeCoIn_5 .

In Fig. S20, we compare the hybridization functions and the density of states of the c electrons, $\rho_c(\omega)$, for the two compounds (CeCo_2P_2 and CeCoIn_5). The c -electron density of states is defined as

$$\rho_c(\omega) = \frac{1}{N} \sum_{\mathbf{k}, n} \delta(\epsilon - \epsilon_{\mathbf{k}, n}) \quad (\text{S10.19})$$

We conclude that the hybridization function of CeCo_2P_2 at the Fermi energy is much larger than that of CeCoIn_5 , with the latter being approximately 30% of the former. This enhanced hybridization can be attributed to the larger c -electron density of states in CeCo_2P_2 , which allows more c electrons to participate in the hybridization. Such enhanced hybridization is expected to result in a higher Kondo temperature, which is qualitatively consistent with experimental observations: the Kondo temperature of CeCo_2P_2 is estimated to be around 100K, much higher than that of CeCoIn_5 , which is approximately 40K [117, 118].

Finally, we comment that the lattice constants may vary with temperature, as reported in Ref. [119], implying a potential temperature dependence of the hybridization functions. Such variations could, in turn, influence the effective Kondo temperatures.

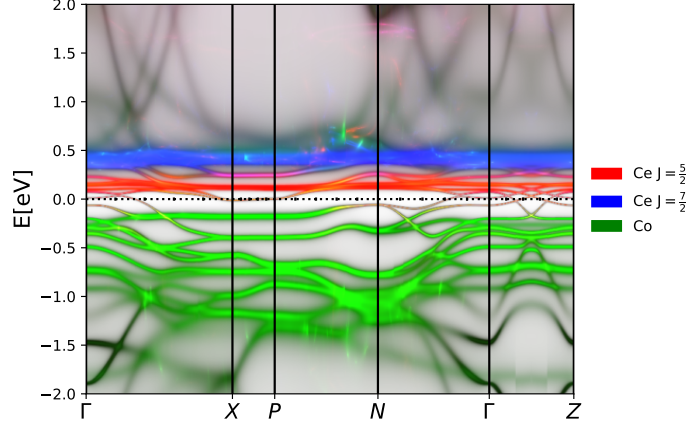


Figure S21. Momentum-resolved spectral function in the AFM phase. Colors indicate the spectral weight contribution from different electronic components.

Nonetheless, our results suggest that the relatively high Kondo temperature of CeCo_2P_2 may be understood via its relatively strong hybridization function.

5. eDMFT calculations

To further demonstrate the coexistence of the Kondo effect and antiferromagnetism (AFM), we perform embedded dynamical mean-field theory (eDMFT) calculations[79–82], combining DFT with DMFT. The calculations are carried out in the AFM phase at $T = 100$ K, using lattice structures taken from the experimental results of Ref. [120]. In Fig.S21, we present the k -resolved interacting spectral function, where the $J = 5/2$ f -electron states are observed near the Fermi energy. Similar features are seen in the local density of states (DOS) shown in Fig. S21. Both results indicate the development of the Kondo effect within the AFM phase.

Our eDMFT results at $T = 100$ K suggest that the Kondo temperature within the theoretical calculations is higher than 100 K. We note, however, that the lattice constants can vary with temperature in experiments, as reported in Ref. [119]. Such variations, which are not captured in the present theoretical calculations, could also affect the Kondo temperature. Therefore, an accurate theoretical determination of the Kondo temperature would require accounting for the temperature dependence of the lattice structure, which would involve rather costly calculations. We thus leave this for future work. Based on our current calculations, we can conclude that: (1) the Kondo effect coexists with antiferromagnetism; and (2) the Kondo temperature is relatively high. This relatively large Kondo temperature can be understood in terms of the strong hybridization function discussed near Fig. S20.

Appendix XI: Band topology of the Kondo phase

We discuss the band topology of the anti-ferromagnetic Kondo phase in this Appendix. In this section, we will use the conventional cell of the PM phase which is the primitive cell of the AFM phase.

1. Glide mirror- z symmetry

We discuss the properties of glide mirror- z symmetry. In this section, we consider the conventional unit cell. In the non-magnetic phase, the system exhibits mirror- z symmetry with the mirror plane located at the Ce plane in Fig. S4, which is symmorphic. However, in the magnetic phase, the mirror- z symmetry maps $\text{Co}_{1,2}$ atoms to $\text{Co}_{3,4}$ atoms. Since $\text{Co}_{1,2}$ and $\text{Co}_{3,4}$ atoms possess opposite magnetic moments, mirror- z is no longer a symmetry operation. However, by combining mirror- z with translational symmetry, we obtain a glide mirror- z transformation defined as

$$h = \{M_z | 1/2, 1/2, 1/2\} \quad (\text{S11.1})$$

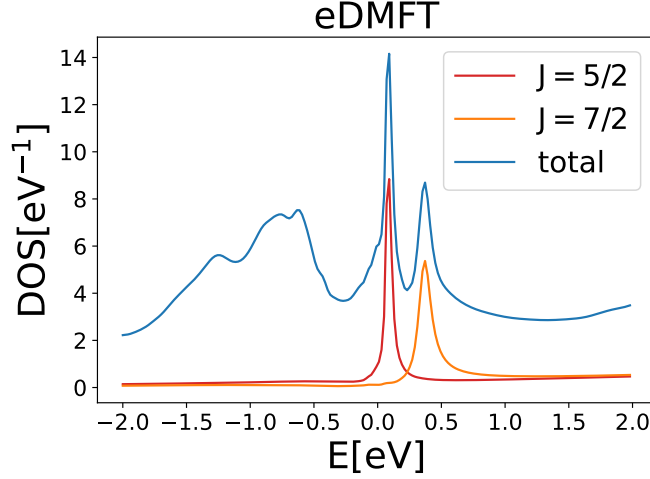


Figure S22. Density of states (DOS) of Ce $4f$ electrons with $J = 5/2$ and $J = 7/2$, along with the total electron density of states.

which characterizes a mirror z transformation followed by a $(1/2, 1/2, 1/2)$ shifting. glide mirror- z transformation is a symmetry operation of the magnetic phase.

It is worth noting that, in the non-magnetic phase, the $(1/2, 1/2, 1/2)$ translation is also a symmetry operation, meaning that there is no nonsymmorphic symmetry in this phase. The magnetic order breaks both the $(1/2, 1/2, 1/2)$ translational symmetry and the mirror- z symmetry but preserves the glide mirror- z symmetry $M_z|1/2, 1/2, 1/2$.

2. Nodal line in the Kondo phase

We demonstrate that, in the AFM Kondo phase, the glide mirror- z symmetry protects the nodal line at $k_z = 1/2$ plane. Acting on c and f electrons, we have

$$\begin{aligned} hc_{\mathbf{R},a,i,\sigma}h^{-1} &= \sum_{b,j,\sigma'} U_{ai\sigma,bj\sigma'}^h c_{h(\mathbf{R}+\mathbf{r}_a)-\mathbf{r}_b,b,j,\sigma'} \\ hf_{\mathbf{R},a,i,\sigma}h^{-1} &= \sum_{b,j,\sigma'} U_{ai\sigma,bj\sigma'}^{h,f} f_{h(\mathbf{R}+\mathbf{r}_a)-\mathbf{r}_b,b,j,\sigma'}. \end{aligned} \quad (\text{S11.2})$$

$U_{ai\sigma,bj\sigma'}^h, U_{ai\sigma,bj\sigma'}^{h,f}$ are unitary matrices characterize the glide mirror z transformation. In the momentum space, we have

$$\begin{aligned} hc_{\mathbf{k},a,i,\sigma}h^{-1} &= \frac{1}{\sqrt{N}} \sum_{\mathbf{R},j,\sigma'} U_{ai\sigma,bj\sigma'}^h c_{h(\mathbf{R}+\mathbf{r}_a)-\mathbf{r}_b,b,j,\sigma'} e^{-i2\pi\mathbf{k}\cdot(\mathbf{R}+\mathbf{r}_a)} \\ &= \frac{1}{N} \sum_{\mathbf{R},\mathbf{k}',b,j,\sigma'} U_{ai\sigma,bj\sigma'}^h c_{\mathbf{k}',b,j} e^{i2\pi\mathbf{k}'\cdot(h(\mathbf{R}+\mathbf{r}_a))} e^{-i2\pi\mathbf{k}\cdot(\mathbf{R}+\mathbf{r}_a)} \\ &= \sum_{b,j,\sigma'} U_{ai\sigma,bj\sigma'}^h c_{M_z\mathbf{k},b,j,\sigma'} e^{i2\pi M_z\mathbf{k}\cdot\Delta\mathbf{r}} \\ hf_{\mathbf{k},a,i,\sigma}h^{-1} &= \sum_{b,j,\sigma'} U_{ai\sigma,bj\sigma'}^{h,f} f_{M_z\mathbf{k},b,j,\sigma'} e^{i2\pi M_z\mathbf{k}\cdot\Delta\mathbf{r}} \end{aligned} \quad (\text{S11.3})$$

where $\Delta\mathbf{r} = (1/2, 1/2, 1/2)$.

We now show the transformation matrix (defined in Eq. S11.2) for each orbital. For the $d@Co$ orbitals, we have

$$U_{ai\sigma,bj\sigma'}^{h,Co} = \begin{bmatrix} 0 & 1 \\ 1 & 0 \\ & 0 & 1 \\ & 1 & 0 \end{bmatrix}_{a,b} \otimes \begin{bmatrix} 1 & & & \\ & -1 & & \\ & & -1 & \\ & & & 1 \end{bmatrix}_{i,j} \otimes \begin{bmatrix} i \\ -i \end{bmatrix}_{\sigma,\sigma'} \quad (\text{S11.4})$$

where indices a, b denote four Co atoms, i, j denote five d -orbitals ($d_{z^2}, d_{xz}, d_{yz}, d_{x^2-y^2}, d_{xy}$), and σ, σ' denote the spin indices (\uparrow, \downarrow). The transformation matrix for the $p@P$ orbitals are

$$U_{ai\sigma,bj\sigma'}^{h,P} = \begin{bmatrix} 0 & 1 \\ 1 & 0 \\ & 0 & 1 \\ & 1 & 0 \end{bmatrix}_{a,b} \otimes \begin{bmatrix} -1 & & \\ & 1 & \\ & & 1 \end{bmatrix}_{i,j} \otimes \begin{bmatrix} i & \\ & -i \end{bmatrix}_{\sigma,\sigma'} \quad (\text{S11.5})$$

where indices a, b denote four P atoms, i, j denote three p -orbitals (p_z, p_x, p_y), and σ, σ' denote the spin indices (\uparrow, \downarrow). The transformation matrix for the $d@Ce$ are

$$U_{ai\sigma,bj\sigma'}^{h,d@Ce} = \begin{bmatrix} & 1 \\ 1 & \end{bmatrix}_{a,b} \begin{bmatrix} 1 & & \\ & -1 & \\ & & -1 & \\ & & & 1 & \\ & & & & 1 \end{bmatrix}_{i,j} \otimes \begin{bmatrix} i & \\ & -i \end{bmatrix}_{\sigma,\sigma'} \quad (\text{S11.6})$$

where indices a, b denote two Ce atoms, i, j denote five d -orbitals ($d_{z^2}, d_{xz}, d_{yz}, d_{x^2-y^2}, d_{xy}$), and σ, σ' denote the spin indices (\uparrow, \downarrow). The transformation for the $d@Ce$ are

$$U_{ai\sigma,bj\sigma'}^{h,f} = \begin{bmatrix} & 1 \\ 1 & \end{bmatrix}_{a,b} \begin{bmatrix} -1 & & & & \\ & 1 & & & \\ & & 1 & & \\ & & & -1 & \\ & & & & -1 & \\ & & & & & 1 & \\ & & & & & & 1 \end{bmatrix}_{i,j} \otimes \begin{bmatrix} i & \\ & -i \end{bmatrix}_{\sigma,\sigma'} \quad (\text{S11.7})$$

where indices a, b denote two Ce atoms, i, j denote seven f -orbitals ($f_{z^3}, f_{xz^2}, f_{yz^2}, f_{z(x^2-y^2)}, f_{xyz}, f_{x(x^2-3y^2)}, f_{y(3x^2-y^2)}$), and σ, σ' denote the spin indices (\uparrow, \downarrow).

There are two mirror- z invariant planes labeled by $\{(k_x, k_y, 1/2)\}_{k_x, k_y}$ and $\{(k_x, k_y, 0)\}_{k_x, k_y}$. At the mirror- z -invariant planes, we have

$$\begin{aligned} hc_{(k_x, k_y, 1/2), a, i, \sigma} h^{-1} &= \sum_{b, j, \sigma'} U_{ai\sigma, bj\sigma'}^h c_{(k_x, k_y, 1/2), b, j, \sigma'} e^{i2\pi(k_x, k_y, -1/2) \cdot (\Delta\mathbf{r}) + i2\pi(0, 0, 1) \cdot \mathbf{r}_b} \\ hc_{(k_x, k_y, 0), a, i, \sigma} h^{-1} &= \sum_{b, j, \sigma'} U_{ai\sigma, bj\sigma'}^h c_{(k_x, k_y, 0), b, j, \sigma'} e^{i2\pi(k_x, k_y, 0) \cdot (\Delta\mathbf{r})} \\ hf_{(k_x, k_y, 1/2), a, i, \sigma} h^{-1} &= \sum_{b, j, \sigma'} U_{ai\sigma, bj\sigma'}^{h,f} f_{(k_x, k_y, 1/2), b, j, \sigma'} e^{i2\pi(k_x, k_y, -1/2) \cdot (\Delta\mathbf{r}) + i2\pi(0, 0, 1) \cdot \mathbf{r}_b} \\ hf_{(k_x, k_y, 0), a, i, \sigma} h^{-1} &= \sum_{b, j, \sigma'} U_{ai\sigma, bj\sigma'}^{h,f} f_{(k_x, k_y, 0), b, j, \sigma'} e^{i2\pi(k_x, k_y, 0) \cdot (\Delta\mathbf{r})} \end{aligned} \quad (\text{S11.8})$$

Here, we focus on the $k_z = 1/2$ plane, where we observe the formation of the nodal line. On the $k_z = 1/2$ plane, we can introduce the electron operators which correspond to the eigenvectors of the glide mirror- z symmetry (Eq. S11.8). The operators that form the eigenbasis of glide mirror- z transformation (h) are given in Tab. S2.

From Tab. S2, we conclude that bands at $k_z = 1/2$ plane have either $+ie^{i\pi(k_x+k_y)}$ or $-ie^{i\pi(k_x+k_y)}$ eigenvalue under glide mirror- z transformations (h). Moreover, due to the $P \cdot \mathcal{T}$ symmetry, the bands are also two-fold degenerate at each momentum. We now discuss the h -eigenvalues of two electrons that are connected by $P \cdot \mathcal{T}$ symmetry. We note

$$\begin{aligned} (P \cdot \mathcal{T})c_{\mathbf{R}, a, i, \sigma} (P \cdot \mathcal{T})^{-1} &= \sum_{b, j, \sigma'} U_{ai\sigma, bj\sigma'}^{P \cdot \mathcal{T}} c_{P(\mathbf{R}+\mathbf{r}_a)-\mathbf{r}_b, b, j, \sigma'} \\ (P \cdot \mathcal{T})f_{\mathbf{R}, a, i, \sigma} (P \cdot \mathcal{T})^{-1} &= \sum_{b, j, \sigma'} U_{ai\sigma, bj\sigma'}^{P \cdot \mathcal{T}, f} f_{P(\mathbf{R}+\mathbf{r}_a)-\mathbf{r}_b, b, j, \sigma'} \\ (P \cdot \mathcal{T})i(P \cdot \mathcal{T})^{-1} &= -i \end{aligned} \quad (\text{S11.9})$$

Operator	Eigenvalue
$\frac{1}{\sqrt{2}}(C(k_x, k_y, 1/2), C_{o_1, i, \sigma} + C(k_x, k_y, 1/2), C_{o_2, i, \sigma})$	$i s_{d,i}^{M_z} \sigma e^{i\pi(k_x+k_y)}$
$\frac{1}{\sqrt{2}}(C(k_x, k_y, 1/2), C_{o_1, i, \sigma} - C(k_x, k_y, 1/2), C_{o_2, i, \sigma})$	$-i s_{d,i}^{M_z} \sigma e^{i\pi(k_x+k_y)}$
$\frac{1}{\sqrt{2}}(C(k_x, k_y, 1/2), C_{o_3, i, \sigma} + C(k_x, k_y, 1/2), C_{o_4, i, \sigma})$	$-i s_{d,i}^{M_z} \sigma e^{i\pi(k_x+k_y)}$
$\frac{1}{\sqrt{2}}(C(k_x, k_y, 1/2), C_{o_3, i, \sigma} - C(k_x, k_y, 1/2), C_{o_4, i, \sigma})$	$i s_{d,i}^{M_z} \sigma e^{i\pi(k_x+k_y)}$
$\frac{1}{\sqrt{2}}(-i e^{i2\pi z} C(k_x, k_y, 1/2), P_{1, i, \sigma} + C(k_x, k_y, 1/2), P_{2, i, \sigma})$	$s_{p,i}^{M_z} e^{i\pi(k_x+k_y)} \sigma$
$\frac{1}{\sqrt{2}}(i e^{i2\pi z} C(k_x, k_y, 1/2), P_{1, i, \sigma} + C(k_x, k_y, 1/2), P_{2, i, \sigma})$	$-i s_{p,i}^{M_z} e^{i\pi(k_x+k_y)} \sigma$
$\frac{1}{\sqrt{2}}(i e^{i2\pi z} C(k_x, k_y, 1/2), P_{3, i, \sigma} + C(k_x, k_y, 1/2), P_{4, i, \sigma})$	$i s_{p,i}^{M_z} \sigma e^{i\pi(k_x+k_y)}$
$\frac{1}{\sqrt{2}}(-i e^{i2\pi z} C(k_x, k_y, 1/2), P_{3, i, \sigma} + C(k_x, k_y, 1/2), P_{4, i, \sigma})$	$-i s_{p,i}^{M_z} \sigma e^{i\pi(k_x+k_y)}$
$\frac{1}{\sqrt{2}}(C(k_x, k_y, 1/2), C_{e_1, i, \sigma} + i C(k_x, k_y, 1/2), C_{e_2, i, \sigma})$	$i s_{d,i}^{M_z} \sigma e^{i\pi(k_x+k_y)}$
$\frac{1}{\sqrt{2}}(C(k_x, k_y, 1/2), C_{e_1, i, \sigma} - i C(k_x, k_y, 1/2), C_{e_2, i, \sigma})$	$-i s_{d,i}^{M_z} \sigma e^{i\pi(k_x+k_y)}$
$\frac{1}{\sqrt{2}}(f(k_x, k_y, 1/2), C_{e_1, i, \sigma} + i f(k_x, k_y, 1/2), C_{e_2, i, \sigma})$	$i s_{f,i}^{M_z} \sigma e^{i\pi(k_x+k_y)}$
$\frac{1}{\sqrt{2}}(f(k_x, k_y, 1/2), C_{e_1, i, \sigma} - i f(k_x, k_y, 1/2), C_{e_2, i, \sigma})$	$-i s_{f,i}^{M_z} \sigma e^{i\pi(k_x+k_y)}$

Table S2. Eigenbasis of glide mirror z transformation (h). We have also introduced the mirror- z eigenvalues for the spinless orbitals. Specifically, $s_{d,i}^{M_z} = 1, -1, -1, 1, 1$ for $i = 1, 2, 3, 4, 5$ respectively, $s_{p,i}^{M_z} = -1, 1, 1$ for $i = 1, 2, 3$ respectively, and $s_{f,i}^{M_z} = -1, 1, 1, -1, -1, -1, 1, 1$ for $i = 1, 2, 3, 4, 5, 6, 7$ respectively.

where $U^{P \cdot \mathcal{T}}, U^{P \cdot \mathcal{T}, f}$ are transformation matrices. For $d@Co$ orbitals, we have

$$U_{ai\sigma, bj\sigma'}^{P \cdot \mathcal{T}, Co} = \begin{bmatrix} 0 & 0 & 0 & 1 \\ 0 & 0 & 1 & 0 \\ 0 & 1 & 0 & 0 \\ 1 & 0 & 0 & 0 \end{bmatrix}_{a,b} \oplus \mathbb{I}_{i,j} \oplus [i\sigma^y]_{\sigma, \sigma'} \quad (\text{S11.10})$$

For $p@P$ orbitals, we have

$$U_{ai\sigma, bj\sigma'}^{P \cdot \mathcal{T}, P} = \begin{bmatrix} 0 & 0 & 0 & 1 \\ 0 & 0 & 1 & 0 \\ 0 & 1 & 0 & 0 \\ 1 & 0 & 0 & 0 \end{bmatrix}_{a,b} \oplus [-\mathbb{I}]_{i,j} \oplus [i\sigma^y]_{\sigma, \sigma'} \quad (\text{S11.11})$$

For $d@Ce$ orbitals, we have

$$U_{ai\sigma, bj\sigma'}^{P \cdot \mathcal{T}, d@Co} = \begin{bmatrix} 1 & 0 \\ 0 & 1 \end{bmatrix}_{a,b} \oplus \mathbb{I}_{i,j} \oplus [i\sigma^y]_{\sigma, \sigma'} \quad (\text{S11.12})$$

For $f@Ce$ orbitals, we have

$$U_{ai\sigma, bj\sigma'}^{P \cdot \mathcal{T}, f} = \begin{bmatrix} 1 & 0 \\ 0 & 1 \end{bmatrix}_{a,b} \oplus [-\mathbb{I}]_{i,j} \oplus [i\sigma^y]_{\sigma, \sigma'} \quad (\text{S11.13})$$

We then investigate the $P \cdot \mathcal{T}$ transformations using the eigenbasis of glide mirror- z transformation (Tab. S2). The results are shown in Tab. S3. We note that, at $k_z = 1/2$ plane, two electron operators connected by $P \cdot \mathcal{T}$ always have the same glide mirror- z eigenvalues.

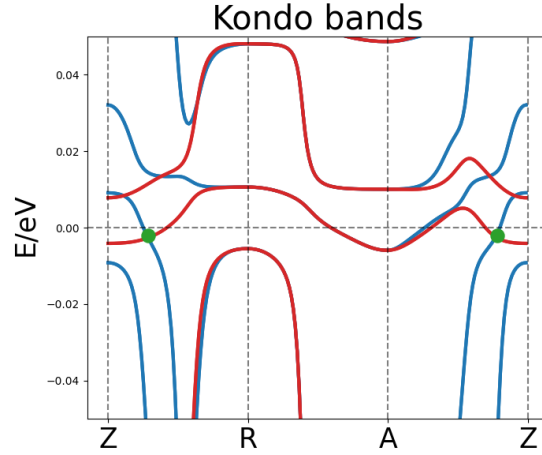
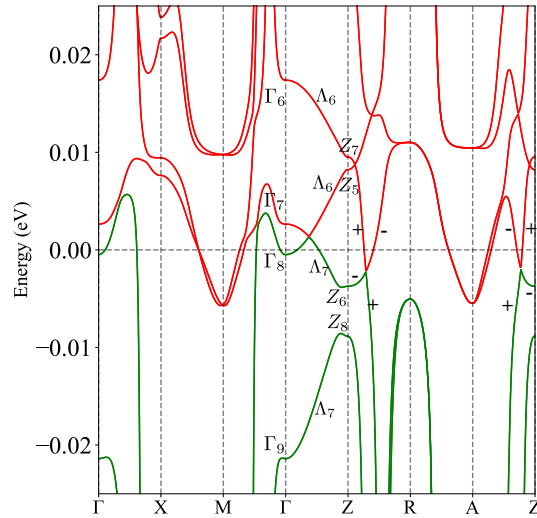
Therefore, when two bands with different glide mirror- z eigenvalues form nodes at $k_z = 1/2$ plane, the nodes will be symmetry protected. As we show in Fig. S23, there is a nodal line near Fermi energy formed by two bands with different glide mirror- z eigenvalues.

3. Irreducible representation of the Kondo bands

To further understand the topology of the Kondo phase, we investigate the irreducible representation of the bands [91, 92, 121]. The results are shown in Fig. S24. We observe that, besides the nodal line, there is also a C_{4z} -protected Dirac node near the Fermi energy (from two bands with irreducible representation Λ_6 and Λ_7) along Γ - Z line as shown in Fig. S24.

Finally, we discuss various possibilities of removing the node and nodal line by breaking symmetries or fine-tuning the bands.

Operator: γ	Operator after transformation: $(P \cdot T)\gamma(P \cdot T)^{-1}$
$\frac{1}{\sqrt{2}}(C(k_x, k_y, 1/2), Co_{1, i, \sigma} + C(k_x, k_y, 1/2), Co_{2, i, \sigma})$	$\frac{\sigma}{\sqrt{2}}(C(k_x, k_y, 1/2), Co_{4, i, -\sigma} + C(k_x, k_y, 1/2), Co_{3, i, -\sigma})$
$\frac{1}{\sqrt{2}}(C(k_x, k_y, 1/2), Co_{1, i, \sigma} - C(k_x, k_y, 1/2), Co_{2, i, \sigma})$	$\frac{\sigma}{\sqrt{2}}(C(k_x, k_y, 1/2), Co_{4, i, -\sigma} - C(k_x, k_y, 1/2), Co_{3, i, -\sigma})$
$\frac{1}{\sqrt{2}}(C(k_x, k_y, 1/2), Co_{3, i, \sigma} + C(k_x, k_y, 1/2), Co_{4, i, \sigma})$	$\frac{\sigma}{\sqrt{2}}(C(k_x, k_y, 1/2), Co_{2, i, -\sigma} + C(k_x, k_y, 1/2), Co_{1, i, -\sigma})$
$\frac{1}{\sqrt{2}}(C(k_x, k_y, 1/2), Co_{3, i, \sigma} - C(k_x, k_y, 1/2), Co_{4, i, \sigma})$	$\frac{\sigma}{\sqrt{2}}(C(k_x, k_y, 1/2), Co_{2, i, -\sigma} - C(k_x, k_y, 1/2), Co_{1, i, -\sigma})$
$\frac{1}{\sqrt{2}}(-ie^{i2\pi z} C(k_x, k_y, 1/2), P_{1, i, \sigma} + C(k_x, k_y, 1/2), P_{2, i, \sigma})$	$\frac{\sigma}{\sqrt{2}}(ie^{-i2\pi z} C(k_x, k_y, 1/2), P_{4, i, -\sigma} + C(k_x, k_y, 1/2), P_{3, i, -\sigma})$
$\frac{1}{\sqrt{2}}(ie^{i2\pi z} C(k_x, k_y, 1/2), P_{1, i, \sigma} + C(k_x, k_y, 1/2), P_{2, i, \sigma})$	$\frac{\sigma}{\sqrt{2}}(-ie^{-i2\pi z} C(k_x, k_y, 1/2), P_{4, i, -\sigma} + C(k_x, k_y, 1/2), P_{3, i, -\sigma})$
$\frac{1}{\sqrt{2}}(ie^{i2\pi z} C(k_x, k_y, 1/2), P_{3, i, \sigma} + C(k_x, k_y, 1/2), P_{4, i, \sigma})$	$\frac{\sigma}{\sqrt{2}}(-ie^{-i2\pi z} C(k_x, k_y, 1/2), P_{2, i, -\sigma} + C(k_x, k_y, 1/2), P_{1, i, -\sigma})$
$\frac{1}{\sqrt{2}}(-ie^{i2\pi z} C(k_x, k_y, 1/2), P_{3, i, \sigma} + C(k_x, k_y, 1/2), P_{4, i, \sigma})$	$\frac{\sigma}{\sqrt{2}}(ie^{-i2\pi z} C(k_x, k_y, 1/2), P_{2, i, -\sigma} + C(k_x, k_y, 1/2), P_{1, i, -\sigma})$
$\frac{1}{\sqrt{2}}(C(k_x, k_y, 1/2), Ce_{1, i, \sigma} + iC(k_x, k_y, 1/2), Ce_{2, i, \sigma})$	$\frac{\sigma}{\sqrt{2}}(C(k_x, k_y, 1/2), Ce_{1, i, -\sigma} - iC(k_x, k_y, 1/2), Ce_{2, i, -\sigma})$
$\frac{1}{\sqrt{2}}(C(k_x, k_y, 1/2), Ce_{1, i, \sigma} - iC(k_x, k_y, 1/2), Ce_{2, i, \sigma})$	$\frac{\sigma}{\sqrt{2}}(C(k_x, k_y, 1/2), Ce_{1, i, -\sigma} + iC(k_x, k_y, 1/2), Ce_{2, i, -\sigma})$
$\frac{1}{\sqrt{2}}(f(k_x, k_y, 1/2), Ce_{1, i, \sigma} + if(k_x, k_y, 1/2), Ce_{2, i, \sigma})$	$\frac{\sigma}{\sqrt{2}}(f(k_x, k_y, 1/2), Ce_{1, i, -\sigma} - if(k_x, k_y, 1/2), Ce_{2, i, -\sigma})$
$\frac{1}{\sqrt{2}}(f(k_x, k_y, 1/2), Ce_{1, i, \sigma} - if(k_x, k_y, 1/2), Ce_{2, i, \sigma})$	$\frac{\sigma}{\sqrt{2}}(f(k_x, k_y, 1/2), Ce_{1, i, -\sigma} + if(k_x, k_y, 1/2), Ce_{2, i, -\sigma})$

Table S3. Transformation properties of the glide-mirror- z eigenstates.Figure S23. Band structure of the Kondo phase ($T = 10^{-4}$ eV) in a narrow energy window. The same band structure has also been shown in Fig. S19 in a larger energy window. Blue and red mark the bands with glide mirror- z eigenvalues $\pm ie^{i\pi(k_x+k_y)}$ respectively. Green dots mark the positions of the nodal line that appears near Fermi energy.Figure S24. Band structure of the Kondo phase ($T = 10^{-4}$ eV). The same band structure with different energy windows has also been shown in Fig. S19 and Fig. S23. We have also labeled the irreducible representation of bands at high-symmetry point Γ , Z , and along high-symmetry line Γ - Z .

- We can realize an insulator state by breaking the glide mirror- z and C_{4z} symmetries which will gap out both the Dirac node and the nodal line. The resulting state is a trivial insulator. We remark that $P \cdot \mathcal{T}$ symmetry alone cannot protect non-trivial topological states in magnetic space groups, while P and $\mathcal{T} \cdot \tau$ (where τ denotes translational transformation) can[5, 122].
- We could remove the Dirac node by switching the Γ_7 state and Γ_8 state at Γ point. In this case, if we further break glide mirror- z symmetry and gap out the nodal line, we realize an axion insulator [8, 123, 124] (protected by the inversion symmetry) with a non-trivial Z_4 index which equals to 2.
- We could remove the nodal line by switching Z_7 state with Z_6 state at Z point. In this case, the Dirac node has also been removed (note that Z_7 state can connect to Γ_8 state along $\Gamma - Z$ line via Λ_6 state). We then realize an obstructed atomic insulator [87, 125] with obstructed positions at $8f$ (at the middle of two nearest-neighbor Co atoms):

$$\left(\pm\frac{1}{4}, \pm\frac{1}{4}, \pm\frac{1}{4}\right) \quad (\text{S11.14})$$

Appendix XII: Surface state

In this appendix, we discuss the surface states of the system.

1. Symmetry properties

For a given single-particle Hamiltonian with hopping matrix $h_{\mathbf{k}, i\bar{\sigma}, j\sigma'}$ where i, j are orbital indices and σ, σ' is the spin index. For fixed k_x, k_y , we can treat the system as an effective 1D system along z direction with Hamiltonian

$$h_{k_z, i\bar{\sigma}, j\sigma'}^{1D, (k_x, k_y)} = h_{(k_x, k_y, k_z), i\bar{\sigma}, j\sigma'} \quad (\text{S12.1})$$

Hence, we can examine the symmetry properties and the corresponding surface states of the 1D system with k_x and k_y lying within the nodal line (near the Γ point), as well as outside the nodal line. We also comment that, here we are mainly focus on the surface state obtained from the effective 1D system. The 2D topology could potentially also produce surface states. However, as we will show later, the surface states can be merged into the gap, we do not expect the 2D topology to give an in-gap state.

In general, the relevant symmetries of the effective 1D system at a generic k_x, k_y point are $\{M_z | 1/2, 1/2, 1/2\}, P \cdot \mathcal{T}$. We also remark that, if we focus on the effective 1D system, $\{M_z | \frac{1}{2}, \frac{1}{2}, \frac{1}{2}\}$ is no longer a nonsymmorphic symmetry for this 1D system. For the effective 1D system, the only maximal Wyckoff positions (2a) are

$$R_z = 1/4, \quad R_z = 3/4. \quad (\text{S12.2})$$

The non-maximal Wyckoff positions (4b) are

$$R_z = 0 + z, \quad R_z = 0 - z, \quad R_z = 1/2 + z, \quad R_z = 1/2 - z \quad (\text{S12.3})$$

Co atoms are located at the maximal Wyckoff positions (2a). Ce atoms are located at the non-maximal Wyckoff positions with $z = 0$. In general, we have three situations as shown in Table S4, where we have also provided the corresponding irreducible representations at $k_z = 0, 1/2$.

EBR	Wyckoff position	Orbital	Irreps at $k_z = 0$	Irreps at $k_z = 1/2$
EBR_+	2a	$s \uparrow @ \frac{1}{4}, s \downarrow @ \frac{3}{4}$	$i, -i$	$i\lambda_{k_x, k_y}, i\lambda_{k_x, k_y}$
EBR_-	2a	$s \downarrow @ \frac{1}{4}, s \uparrow @ \frac{3}{4}$	$i, -i$	$-i\lambda_{k_x, k_y}, -i\lambda_{k_x, k_y}$
$EBR_+ \oplus EBR_-$	4b	$s \uparrow @ z, s \downarrow @ (-z)$ $s \uparrow @ (1/2 + z), s \downarrow @ (1/2 - z)$	$i, -i, i, -i$	$i\lambda_{k_x, k_y}, -i\lambda_{k_x, k_y}, i\lambda_{k_x, k_y}, -i\lambda_{k_x, k_y}$

Table S4. Symmetry properties of the effective 1D system. $s\sigma$ suggest the corresponding orbital has the same symmetry property as s orbital with spin σ , and $\lambda_{k_x, k_y} = e^{i\pi(k_x + k_y)}$.

There are two types of elementary band representations (EBRs), denoted by EBR_+, EBR_- , induced by two different types of orbitals at 2a positions as shown in Tab. S4. Electrons at non-maximal Wyckoff positions can be decomposed into $EBR_+ \oplus EBR_-$. We can therefore define the following quantities to characterize the ground states

$$C = N_+ - N_- \quad (\text{S12.4})$$

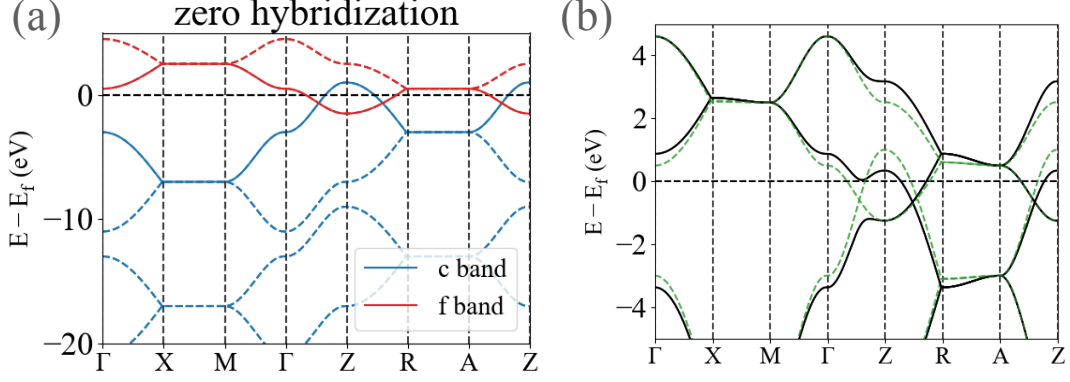


Figure S25. (a) Band structures of the fd -orbital model in the limit of zero hybridization between f and d orbitals (Eq. (S12.7) and Eq. (S12.10)). The parameters are $\epsilon_d = -10$, $M = 5$, $\epsilon_f = 1.5$, $t_{d,z} = t_d = -1$, $t_f = t_{f,z} = 0.5$. (b) Zoom-in view of the band structures near the Fermi energy with finite hybridization (Eq. (S12.13)). Green dashed lines show the band structure with C_{4z} symmetry where the system develops a Dirac node along Γ - Z line and a nodal line at $k_z = 1/2$ plane. Black solid lines show the band structure with a C_{4z} symmetry-breaking term, where the Dirac node has been gapped out. The corresponding parameters are $-t_{fc,1} = t_{fc,C4} = 0.3$.

where

$$\begin{aligned} 2N_+ &= \text{number of filled bands with eigenvalues } i\lambda_{k_x, k_y} \text{ at } k_z = 1/2 \\ 2N_- &= \text{number of filled bands with eigenvalues } -i\lambda_{k_x, k_y} \text{ at } k_z = 1/2. \end{aligned} \quad (\text{S12.5})$$

N_{\pm} corresponds to the number of EBR_{\pm} . The additional factor 2 comes from the $P \cdot \mathcal{T}$ -protected two-fold degeneracy of each band.

2. Effective model of nodal line

We now discuss the nodal-line and the related surface states. To simplify the problem, we take an effective fd -orbital model with only $d_{x^2-y^2}$ -orbital at the Co atom and f_{xyz} -orbital at the Ce atom, where both orbitals appear near the Fermi energy, to understand the surface states. As we will show later, this simplified model reproduces the correct nodal line as we observed in our mean-field solutions (Fig. S23). The advantage of this simplified model is that we can remove other bands that do not contribute to the nodal line. The full Hamiltonian takes the form of

$$H = H_c + H_f + H_{fc} \quad (\text{S12.6})$$

where H_c, H_f are the hopping terms of c and f electrons respectively, and H_{fc} denote the fc hybridization term. We now discuss each term of the Hamiltonian.

The Hamiltonian of the c -block can be written as

$$H_c = \sum_{\mathbf{k}, ij, \sigma} \psi_{c, \mathbf{k}, i, \sigma}^\dagger \psi_{c, \mathbf{k}, j, \sigma} h_{\mathbf{k}, ij, \sigma}^c, \quad \psi_{c, \mathbf{k}, j, \sigma} = [c_{\mathbf{k}, Co1, d_{x^2-y^2}, \sigma} \quad c_{\mathbf{k}, Co2, d_{x^2-y^2}, \sigma} \quad c_{\mathbf{k}, Co3, d_{x^2-y^2}, \sigma} \quad c_{\mathbf{k}, Co4, d_{x^2-y^2}, \sigma}]_j^T$$

$$h_{\mathbf{k}, ij, \sigma}^c = \begin{bmatrix} \epsilon_d - M\sigma + 2t_{d,z} \cos(2\pi k_z) & 4t_d \cos\left(\frac{2\pi k_x}{2}\right) \cos\left(\frac{2\pi k_y}{2}\right) & & \\ 4t_d \cos\left(\frac{2\pi k_x}{2}\right) \cos\left(\frac{2\pi k_y}{2}\right) & \epsilon_d - M\sigma + 2t_{d,z} \cos(2\pi k_z) & & \\ & & \epsilon_d + M\sigma + 2t_{d,z} \cos(2\pi k_z) & 4t_d \cos\left(\frac{2\pi k_x}{2}\right) \cos\left(\frac{2\pi k_y}{2}\right) \\ & & 4t_d \cos\left(\frac{2\pi k_x}{2}\right) \cos\left(\frac{2\pi k_y}{2}\right) & \epsilon_d + M\sigma + 2t_{d,z} \cos(2\pi k_z) \end{bmatrix}_{ij} \quad (\text{S12.7})$$

where ϵ_d denotes the on-site energy term, t_d denotes the in-plane hopping, $t_{d,z}$ denotes the z -direction hopping and M characterizes the splitting induced by the magnetic order. We can diagonalize the $h_{\mathbf{k}, ij, \sigma}^c$ which gives the following eigenvalues and eigenstates

$$E_{c, \mathbf{k}, 1/2, \sigma} = \epsilon_d - M\sigma + 2t_{d,z} \cos(2\pi k_z) \pm 4t_d \cos(2\pi k_x/2) \cos(2\pi k_y/2)$$

$$\begin{aligned}
\gamma_{c,\mathbf{k},1/2,\sigma} &= \frac{1}{\sqrt{2}}(c_{\mathbf{k},Co1,d_{x^2-y^2},\sigma} \pm c_{\mathbf{k},Co2,d_{x^2-y^2},\sigma}) \\
E_{\mathbf{k},3/4,\sigma} &= \epsilon_d + M\sigma + 2t_{d,z} \cos(2\pi k_z) \pm 4t_d \cos(2\pi k_x/2) \cos(2\pi k_y/2) \\
\gamma_{c,\mathbf{k},3/4,\sigma} &= \frac{1}{\sqrt{2}}(c_{\mathbf{k},Co3,d_{x^2-y^2},\sigma} \pm c_{\mathbf{k},Co4,d_{x^2-y^2},\sigma})
\end{aligned} \tag{S12.8}$$

Without loss of generality, we take $M > 0, t_d < 0, t_{d,z} < 0$. This leads to $P \cdot \mathcal{T}$ -protected two-fold degenerate states with energy $E_{c,\mathbf{k},4,\uparrow}, E_{c,\mathbf{k},2,\downarrow}$ near Fermi energy. These states at $k_z = 1/2$ have glide mirror- z eigenvalues $e^{i\pi(k_x+k_y)}$. We show the band structures in Fig. S25 (a), where the two-fold degenerate bands described by $\gamma_{c,\mathbf{k},4,\uparrow}, \gamma_{c,\mathbf{k},2,\downarrow}$ are characterized by solid blue line. To simplify the problem, we could also drop $c_{\mathbf{k},Co1,d_{x^2-y^2},\uparrow}, c_{\mathbf{k},Co2,d_{x^2-y^2},\uparrow}, c_{\mathbf{k},Co3,d_{x^2-y^2},\downarrow}, c_{\mathbf{k},Co4,d_{x^2-y^2},\downarrow}$ electron. These electrons form high-energy bands near $E \sim -15\text{eV}$ in Fig. S25 (a). We can also adiabatically shift the energy of these bands to negative infinity by gradually increasing the strength of magnetic ordering M . We therefore obtain the following new Hamiltonian for c electrons

$$\begin{aligned}
H'_c &= \sum_{\mathbf{k},ij,\sigma} \psi_{c,\mathbf{k},i,\sigma}^\dagger \psi'_{c,\mathbf{k},j,\sigma} h_{\mathbf{k},ij,\sigma}^c \\
\psi'_{c,\mathbf{k},j,\uparrow} &= [c_{\mathbf{k},Co1,d_{x^2-y^2},\downarrow} \quad c_{\mathbf{k},Co2,d_{x^2-y^2},\downarrow}]_j^T, \quad \psi'_{c,\mathbf{k},j,\downarrow} = [c_{\mathbf{k},Co3,d_{x^2-y^2},\uparrow} \quad c_{\mathbf{k},Co4,d_{x^2-y^2},\uparrow}]_j^T \\
h_{\mathbf{k},ij,\sigma}^c &= \begin{bmatrix} \epsilon_d + M + 2t_{d,z} \cos(2\pi k_z) & 4t_d \cos(2\pi k_x/2) \cos(2\pi k_y/2) \\ 4t_d \cos(2\pi k_x/2) \cos(2\pi k_y/2) & \epsilon_d + M + 2t_{d,z} \cos(2\pi k_z) \end{bmatrix}_{ij}
\end{aligned} \tag{S12.9}$$

The Hamiltonian of f block reads

$$\begin{aligned}
H_f &= \sum_{\mathbf{k},ij,\sigma} \psi_{f,\mathbf{k},i,\sigma}^\dagger \psi_{f,\mathbf{k},j,\sigma} h_{\mathbf{k},ij,\sigma}^f, \quad \psi_{f,\mathbf{k},j,\sigma} = [f_{\mathbf{k},Ce1,f_{xyz},\sigma} \quad f_{\mathbf{k},Ce2,f_{xyz},\sigma}]_j^T \\
h_{\mathbf{k},ij,\sigma}^f &= \begin{bmatrix} \epsilon_f + 2t_{f,z} \cos(2\pi k_z) & -4e^{i\sigma 2\pi k_z/2} t_f \cos(2\pi k_x/2) \cos(2\pi k_y/2) \\ -4e^{-i\sigma 2\pi k_z/2} t_f \cos(2\pi k_x/2) \cos(2\pi k_y/2) & \epsilon_f + 2t_{f,z} \cos(2\pi k_z) \end{bmatrix}_{ij}
\end{aligned} \tag{S12.10}$$

where ϵ_f is the on-site energy of f electrons, $t_{f,z}$ and t_f are symmetry-allowed hopping of f electrons. We can diagonalize $H_{\mathbf{k},ij,\sigma}^f$. The corresponding eigenvalues and eigenvectors are

$$\begin{aligned}
E_{f,\mathbf{k},1/2,\sigma} &= \epsilon_f + 2t_{f,z} \cos(2\pi k_z) \pm 4t_f \cos(2\pi k_x/2) \cos(2\pi k_y/2) \\
\gamma_{f,\mathbf{k},1/2,\sigma} &= \frac{1}{\sqrt{2}} \left(\mp e^{-i2\pi k_z \sigma/2} f_{\mathbf{k},Ce1,f_{xyz},\sigma} + f_{\mathbf{k},Ce2,f_{xyz},\sigma} \right)
\end{aligned} \tag{S12.11}$$

We take $t_f > 0$ such that we have a two-fold degenerate state ($E_{f,\mathbf{k},2,\sigma}$) near the Fermi energy. These states also have glide mirror- z eigenvalues $-e^{i\pi(k_x+k_y)}$ at $k_z = -1/2$. We show the band structures in Fig. S25 (a), where the two-fold degenerate bands described by $\gamma_{f,\mathbf{k},2,\uparrow}, \gamma_{f,\mathbf{k},2,\downarrow}$ are characterized by the solid red line. Here, we comment that the parameters are fine-tuned aiming to reproduce the band structures of the the mean-field calculations (Section X3). In addition, we have also taken relatively large hopping parameters of f -electrons (large $t_{f,c}, t_f$). The large $t_{f,z}$ will cause the f -bands at the $k_z = 0$ plane to be shifted away from the Fermi energy. The large t_f will cause the upper f bands ($E_{f,\mathbf{k},1,\sigma}$, the red dashed line of Fig. S25 (a)) at $k_z = 1/2$ plane to be shifted away from the Fermi energy. This adjustment will not change the topological properties, such as nodal lines, of the band structure. However, it will simplify the analysis by shifting irrelevant bands away from the Fermi energy.

We now summarize the band structure of the systems in the zero fc hybridization limit (Fig. S25 (a)). First, for the c blocks, we have in total 8 bands. Due to the magnetic ordering M , half of the bands will be shifted away from the Fermi energy and can be ignored. In addition, the interlayer hopping t_d will split the remaining four bands into two two-fold-degenerate groups. One group has $\{M_z | \frac{1}{2}, \frac{1}{2}, \frac{1}{2}\}$ eigenvalue $e^{i\pi(k_x+k_y)}$ at $k_z = 1/2$ plane and appear near the Fermi energy (blue solid line in Fig. S25 (a)). The other group has $\{M_z | \frac{1}{2}, \frac{1}{2}, \frac{1}{2}\}$ eigenvalue $-e^{i\pi(k_x+k_y)}$ at $k_z = 1/2$ plane and has been shifted away from the Fermi energy. As for the f block, the hopping term t_f will split 4 f bands into two two-fold-degenerate groups. One group has $\{M_z | \frac{1}{2}, \frac{1}{2}, \frac{1}{2}\}$ eigenvalue $e^{i\pi(k_x+k_y)}$ at $k_z = \pi$ plane and appear near the Fermi energy (red solid line in Fig. S25 (a)). The other group has $\{M_z | \frac{1}{2}, \frac{1}{2}, \frac{1}{2}\}$ eigenvalue $-e^{i\pi(k_x+k_y)}$ at $k_z = \pi$ plane and has been shifted away from the Fermi energy by the t_f term. Therefore, in the zero-hybridization limit, c electrons create a two-fold degenerate band near Fermi energy with $\{M_z | \frac{1}{2}, \frac{1}{2}, \frac{1}{2}\}$ eigenvalue $e^{i\pi(k_x+k_y)}$ at $k_z = 1/2$ plane, and f electrons create a two-fold degenerate band near Fermi energy with $\{M_z | \frac{1}{2}, \frac{1}{2}, \frac{1}{2}\}$ eigenvalue $-e^{i\pi(k_x+k_y)}$ at $k_z = 1/2$ plane. These two bands possess different $\{M_z | \frac{1}{2}, \frac{1}{2}, \frac{1}{2}\}$ eigenvalues, resulting in a nodal line at the $k_z = 1/2$ plane. This nodal line persists even after the introduction of fc hybridization due to the glide-mirror- z symmetry. Finally, we comment that the nodal-line here differs from the hourglass fermion [126].

We now introduce the fc hybridization term. We consider the following symmetry-allowed fc hybridization term

$$\begin{aligned}
H_{fc} &= \sum_{\mathbf{k}, ij, \sigma} \psi'_{c, \mathbf{k}, i, \sigma} \psi_{f, \mathbf{k}, j, \sigma} h_{\mathbf{k}, ij, \sigma}^{cf} + \text{h.c.} \\
h_{\mathbf{k}, ij, \uparrow}^{cf} &= \begin{bmatrix} -2e^{i\frac{k_z}{4}}(t_{fc,1} + t_{fc,C4}) \cos(k_x/2) & -2e^{-i\frac{k_z}{4}}(-t_{fc,1} + t_{fc,C4}) \cos(k_y/2) \\ 2(t_{fc,C4} - t_{fc,1})e^{i\frac{k_z}{4}} \cos(k_y/2) & 2(t_{fc,C4} + t_{fc,1})e^{-i\frac{k_z}{4}} \cos(k_x/2) \end{bmatrix}_{ij} \\
h_{\mathbf{k}, ij, \downarrow}^{fc} &= \begin{bmatrix} -2(t_{fc,C4} - t_{fc,1})e^{-i\frac{k_z}{4}} \cos(k_y/2) & -2(t_{fc,C4} + t_{fc,1})e^{i\frac{k_z}{4}} \cos(k_x/2) \\ 2t(t_{fc,C4} + t_{fc,1})e^{-i\frac{k_z}{4}} \cos(k_x/2) & 2(t_{fc,C4} - t_{fc,1})e^{i\frac{k_z}{4}} \cos(k_y/2) \end{bmatrix}_{ij}
\end{aligned} \tag{S12.12}$$

where we have introduced an additional term ($t_{fc,C4}$) that breaks C_{4z} symmetry. As we show later, this additional term could gap out the Dirac crossing along Γ - Z line, but will not affect the formation of the nodal line. This allows us to avoid the effect of the Dirac node when we study the surface states of the nodal line.

Therefore, the full Hamiltonian can be defined as

$$\begin{aligned}
H &= H'_c + H_f + H_{fc} = \sum_{\mathbf{k}, ij, \sigma} h_{\mathbf{k}, ij, \sigma} \psi_{\mathbf{k}, i, \sigma}^\dagger \psi_{\mathbf{k}, j, \sigma} \\
\psi_{\mathbf{k}, i, \uparrow} &= [c_{\mathbf{k}, C_{03}, d_{x^2-y^2}, \uparrow} \quad c_{\mathbf{k}, C_{04}, d_{x^2-y^2}, \uparrow} \quad f_{\mathbf{k}, Ce_1, f_{xyz}, \uparrow} \quad f_{\mathbf{k}, Ce_2, f_{xyz}, \uparrow}]_i^T \\
\psi_{\mathbf{k}, i, \downarrow} &= [c_{\mathbf{k}, C_{01}, d_{x^2-y^2}, \downarrow} \quad c_{\mathbf{k}, C_{02}, d_{x^2-y^2}, \downarrow} \quad f_{\mathbf{k}, Ce_1, f_{xyz}, \downarrow} \quad f_{\mathbf{k}, Ce_2, f_{xyz}, \downarrow}]_i^T \\
h_{\mathbf{k}, ij, \sigma} &= \begin{bmatrix} h'_{\mathbf{k}, \sigma} & h_{\mathbf{k}, \sigma}^{cf} \\ h_{\mathbf{k}, \sigma}^{fc, \dagger} & h_{\mathbf{k}, \sigma}^f \end{bmatrix}
\end{aligned} \tag{S12.13}$$

The band structures are shown in Fig. S25 (b), where we can observe the formation of nodal lines at $k_z = 1/2$ plane. Without C_{4z} symmetry breaking, the system also develops a Dirac node along $\Gamma - Z$ line. To simplify the analysis of the surface states, we consider a non-zero C_{4z} symmetry-breaking term to gap out this Dirac node.

3. Surface states

We now discuss the surface states of the fd model we introduced in Eq. (S12.13). For given k_x, k_y points, we can treat the system as an effective 1D system with the hopping matrix

$$h_{k_z, i\sigma, j\sigma'}^{1D, (k_x, k_y)} = h_{\mathbf{k}, i\sigma, j\sigma'} \tag{S12.14}$$

We now calculate the quantities we introduced in Eq. (S12.4). For the k_x, k_y outside the nodal line (near M point), we have $C = 0$ ($N_+ = 1, N_- = 1$). The ground state of the effective 1D system is adiabatically connected to the atomic insulators where all the c orbitals are filled. Therefore, we do not expect any non-trivial surface state for the momentum points outside the nodal line.

Inside the nodal line, we have $C = -2$ with $N_+ = 0$, and $N_- = 2$. Since $N_- = 2$, the filled bands can be decomposed into

$$\text{filled bands} \sim EBR_- \oplus EBR_- \tag{S12.15}$$

However, the EBR induced by $\psi'_{c, \mathbf{k}}$ electrons are

$$\psi'_{c, \mathbf{k}} \sim EBR_- \oplus EBR_+ \tag{S12.16}$$

The EBR induced by $\psi_{f, \mathbf{k}}$ electrons are (see Tab. S4)

$$\psi_{f, \mathbf{k}} \sim EBR_- \oplus EBR_+ \tag{S12.17}$$

Therefore, one of the EBR_- formed by the filled bands must come from the f orbitals. f -orbital is located at non-maximal Wyckoff positions $4b$ and EBR_- corresponds to the Wannier states at maximal Wyckoff positions $2a$. Therefore, we could conclude that f orbitals develop molecular orbitals located at positions distinct from the Ce atoms.

The formation of the molecular orbitals for the k_x, k_y inside the nodal line could then introduce surface states. To gain a better understanding of the surface state, we investigate the low-energy effective Hamiltonian of the 1D system. The relevant

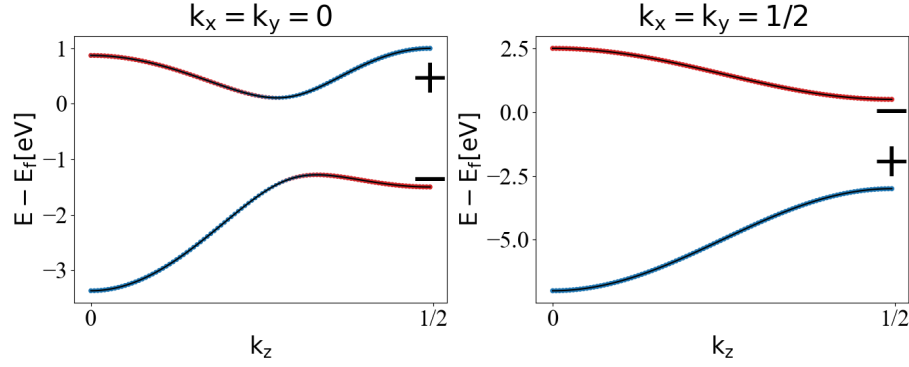


Figure S26. Dispersions of the effective 1D model in Eq. (S12.13) at $k_x = k_y = 0$ (inside the nodal line) and $k_x = k_y = 1/2$ (outside the nodal line). Each band is two-fold degenerate due to $P \cdot \mathcal{T}$ symmetry. Red and blue mark the orbital weights of f and c electrons respectively. $+$, $-$ label the $\{M_z | \frac{1}{2}, \frac{1}{2}, \frac{1}{2}\}$ eigenvalues of the bands at $k_z = 1/2$.

low-energy degrees of freedom (electrons that appear near Fermi energy) are $\gamma_{c,k,4,\uparrow}$, $\gamma_{c,k,2,\downarrow}$ (solid blue lines in Fig. S25 (a)), and $\gamma_{f,k,2,\sigma}$ (solid red lines in Fig. S25 (a)). Transforming to the real space, we find

$$\begin{aligned}
 \gamma_{c,(k_x,k_y,R_z),4,\uparrow} &= \frac{1}{\sqrt{2}} \left(c_{(k_x,k_y,R_z),Co_3,d_{x^2-y^2},\uparrow} - c_{(k_x,k_y,R_z),Co_4,d_{x^2-y^2},\uparrow} \right) \\
 \gamma_{f,(k_x,k_y,R_z),2,\uparrow} &= \frac{1}{\sqrt{2}} \left(f_{(k_x,k_y,R_z),Ce_1,f_{xy},\uparrow} + f_{(k_x,k_y,R_z),Ce_2,f_{xy},\uparrow} \right) \\
 \gamma_{c,(k_x,k_y,R_z),2,\downarrow} &= \frac{1}{\sqrt{2}} \left(c_{(k_x,k_y,R_z),Co_1,d_{x^2-y^2},\downarrow} - c_{(k_x,k_y,R_z),Co_2,d_{x^2-y^2},\downarrow} \right) \\
 \gamma_{f,(k_x,k_y,R_z),2,\downarrow} &= \frac{1}{\sqrt{2}} \left(f_{(k_x,k_y,R_z),Ce_1,f_{xy},\downarrow} + f_{(k_x,k_y,R_z-1),Ce_2,f_{xy},\downarrow} \right)
 \end{aligned} \tag{S12.18}$$

For the effective 1D system, $\gamma_{c,(k_x,k_y,R_z),4,\uparrow}^\dagger$ creates an electron at $R_z = 3/4$, since it is formed by the d orbitals of Co_3, Co_4 . $\gamma_{f,(k_x,k_y,R_z),2,\uparrow}$ creates an electron at $1/4$ since it corresponds to the bonding state of $f_{(k_x,k_y,R_z),Ce_1,f_{xy},\uparrow}$ and $f_{(k_x,k_y,R_z),Ce_2,f_{xy},\uparrow}$. $\gamma_{c,(k_x,k_y,R_z),2,\uparrow}^\dagger$ creates an electron at $R_z = 1/4$, since it is formed by the d orbitals of Co_1, Co_2 . $\gamma_{f,(k_x,k_y,R_z),2,\downarrow}$ creates an electron at $3/4$ since it corresponds to the bonding state of $f_{(k_x,k_y,R_z),Ce_1,f_{xy},\downarrow}$ and $f_{(k_x,k_y,R_z-1),Ce_2,f_{xy},\downarrow}$. The Wannier center of the electron operator can also be obtained by calculating the corresponding Berry phase. We can already observe that $\gamma_{f,(k_x,k_y,R_z),2,\sigma}$ denotes the molecular orbital formed by f electrons. Furthermore, we show the band structures and also the orbital weights for the effective 1D system in Fig. S26. We find that, outside the nodal line, f orbitals are fully empty and thus are irrelevant. This indicates the absence of the surface states.

We now discuss the surface states. Analyzing the 1D band structures shown in Fig. S26 (left panel), we observe a band inversion between the f -molecular orbital and the c orbital. This inversion suggests that the occupied band exhibits orbital contributions from both f and c orbitals. Consequently, a surface state could potentially emerge if the boundary cut through either the molecular f orbital or the bond formed between the f and c orbitals.

We next consider the open boundaries as illustrated in Fig. S27, where the real-space positions of the relevant orbitals are also marked. Generally, there are two types of open boundaries, each distinguished by different colors in Fig. S27. Both types of boundaries cut through the molecular orbitals ($\gamma_{f,(k_x,k_y,R_z),2,\uparrow}$) of f electrons in the spin \uparrow sector. For the spin \downarrow sector, both boundary types slice through the bonds linking the f and c orbitals.

Furthermore, we could consider a boundary that cuts through the molecular f orbitals in the spin \downarrow sector and the f - c bonds in the spin \uparrow sector. However, these boundary configurations can be derived by applying a $P \cdot \mathcal{T}$ transformation to our current boundaries, rendering them equivalent.

In conclusion, we expect two surface states to emerge (each spin sector gives one surface state). This expectation has been confirmed by numerical calculations (Fig. S28) using the Hamiltonian given by Eq. (S12.13). To confirm our previous analysis, we now show that we can merge the surface states to the bulk spectrum by adding additional boundary terms.

We first consider the spin \uparrow sector. Boundary I (green boundary in Fig. S27) cuts through the f molecular orbitals, and then we have an f operator located at the boundary $f_{(k_x,k_y,0),Ce_2,f_{xy},\uparrow}$. This f operator could still hybridize with $\gamma_{c,(k_x,k_y,R_z=0),4,\uparrow}$ operator nearby which leads to a surface state. Therefore, we can consider the following boundary term

$$m_1 \left(f_{(k_x,k_y,0),Ce_2,f_{xy},\uparrow}^\dagger f_{(k_x,k_y,0),Ce_2,f_{xy},\uparrow} + c_{(k_x,k_y,0),Co_4,d_{x^2-y^2},\uparrow}^\dagger c_{(k_x,k_y,0),Co_4,d_{x^2-y^2},\uparrow} \right) \tag{S12.19}$$

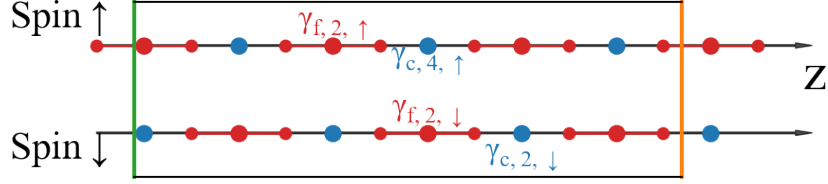


Figure S27. Position of the electron orbitals for the effective 1D system for spin \uparrow and spin \downarrow sector. $\gamma_{f,(k_x,k_y,R_z),2,\uparrow/dn}$ is located at $n \pm 1/4$ with $n \in \mathbb{Z}$ (big red dots). $\gamma_{c,(k_x,k_y,R_z),4,\uparrow}$ ($\gamma_{c,(k_x,k_y,R_z),2,\downarrow}$) is located at $n + 3/4$ ($n + 1/4$), marked by blue dots in the upper (lower) axis. However, from Eq. (S12.18), $\gamma_{f,(k_x,k_y,R_z),2,\sigma}$ is a molecular orbital. $\gamma_{f,(k_x,k_y,R_z),2,\uparrow}$ is formed by the superposition of $f_{(k_x,k_y,R_z),Ce_1,f_{xyz},\uparrow}$ at $n + 0$ and $f_{(k_x,k_y,R_z),Ce_2,f_{xyz},\uparrow}$ at $n + 1/2$ (small red dots in the upper axis). $\gamma_{f,(k_x,k_y,R_z),2,\downarrow}$ is formed by the superposition of $f_{(k_x,k_y,R_z-1),Ce_2,f_{xyz},\downarrow}$ at $n - 1/2$ and $f_{(k_x,k_y,R_z),Ce_1,f_{xyz},\downarrow}$ at n (small red dots in the lower axis). The solid line represents the slab geometry along z direction, where green denotes the first type of boundary (Boundary I, left) and orange denotes the second type of boundary (Boundary II, right).

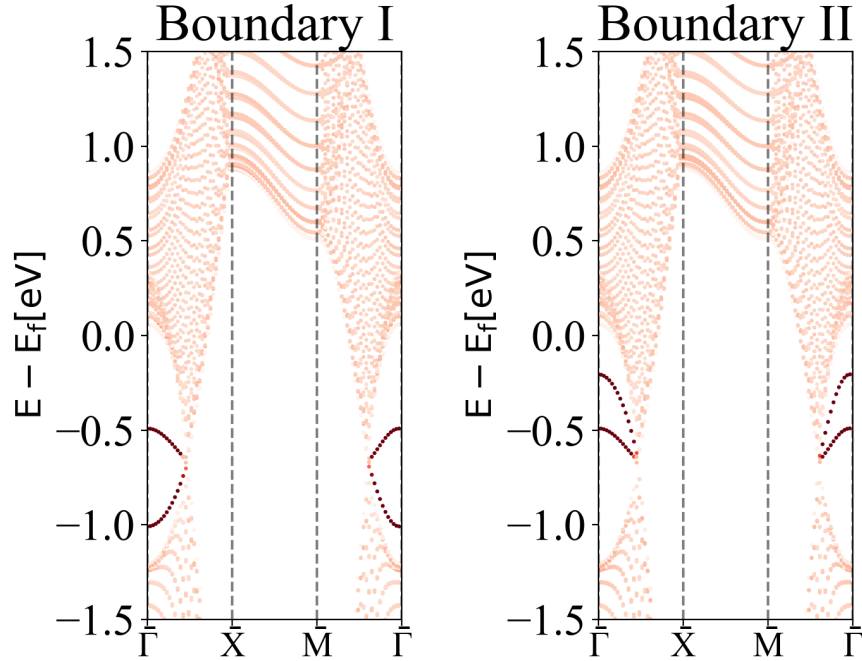


Figure S28. Surface bands calculated via Hamiltonian given by Eq. (S12.13) with open boundary along z directions. Two types of boundaries are illustrated in Fig. S27 by solid and dashed lines. The color denotes the weights of the bands on the surfaces. We can observe two surface states inside the nodal lines.

to shift the energy of the corresponding surface states.

Boundary II (orange boundary Fig. S27) cuts through the f molecular molecular in the spin \uparrow sector, and then we have an f operator located at the boundary $f_{(k_x,k_y,R_n),Ce_1,f_{xyz},\uparrow}$ (where R_n denotes the corresponding unit cell at the boundary). It will hybridize with the nearby c electron $c_{(k_x,k_y,R_n-1),Co_4,dx^2-y^2,\uparrow}$ and creates a surface state. We can consider the following

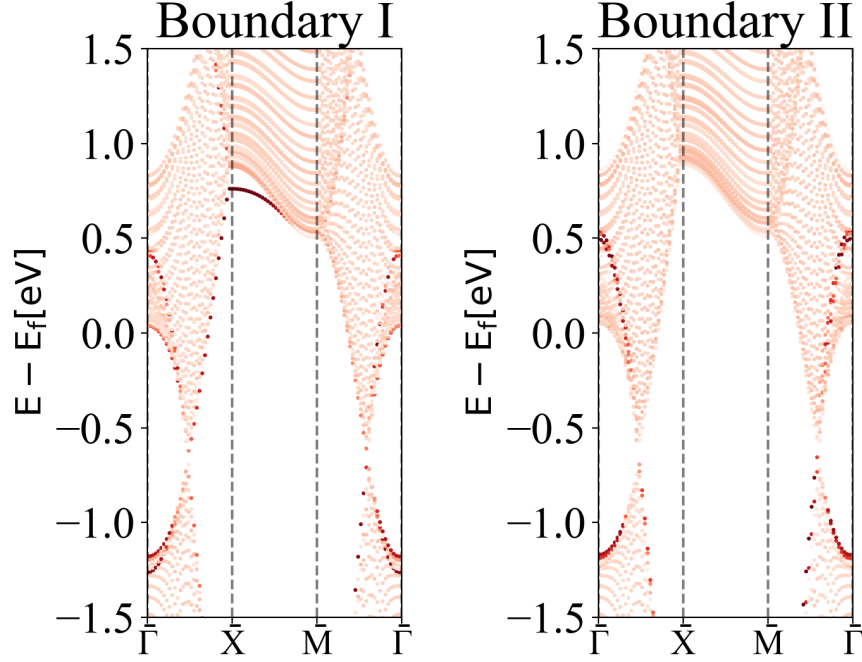


Figure S29. Surface bands with open boundary along z directions. Additional boundary terms defined in Eqs. (S12.19) to (S12.22) have been introduced with $m_1 = 1.5$, $m_2 = 1.3$, $m_3 = -1.0$, $m_4 = 0.4$. We can observe the surface states merge into the bulk spectrum.

boundary term

$$m_2 (c_{(k_x, k_y, R_n - 1), C_{O_4, dx^2 - y^2, \uparrow}}^\dagger c_{(k_x, k_y, R_n - 1), C_{O_4, dx^2 - y^2, \uparrow}} + f_{(k_x, k_y, R_n), C_{e_1, f_{xyz, \uparrow}}}^\dagger f_{(k_x, k_y, R_n), C_{e_1, f_{xyz, \uparrow}}}) \quad (\text{S12.20})$$

to shift the energy of the corresponding surface states.

We next consider the spin \downarrow sector. Boundary I cuts through the bonds formed by $f_{(k_x, k_y, -1), C_{e_2, f_{xyz, \downarrow}}}$ and $c_{(k_x, k_y, 0), C_{O_2, dx^2 - y^2, \downarrow}}$. Then we have a $c_{(k_x, k_y, 0), C_{O_2, dx^2 - y^2, \downarrow}}$ operator located at the boundary which gives a surface state. We can consider the following boundary term

$$m_3 (c_{(k_x, k_y, 0), C_{O_2, dx^2 - y^2, \downarrow}}^\dagger c_{(k_x, k_y, 0), C_{O_2, dx^2 - y^2, \downarrow}}) \quad (\text{S12.21})$$

to shift the energy of the corresponding surface states.

Boundary II cuts through the bonds formed by $f_{(k_x, k_y, R_n), C_{e_2, f_{xyz, \downarrow}}}$ and $c_{(k_x, k_y, R_n + 1), C_{O_2, dx^2 - y^2, \downarrow}}$ in the spin \downarrow sector. Then we have $f_{(k_x, k_y, R_n), C_{e_2, f_{xyz, \downarrow}}}$ operator located at the boundary which gives a surface state. We can consider the following boundary term

$$m_4 (f_{(k_x, k_y, R_n), C_{e_2, f_{xyz, \downarrow}}}^\dagger f_{(k_x, k_y, R_n), C_{e_2, f_{xyz, \downarrow}}}) \quad (\text{S12.22})$$

to shift the energy of the corresponding surface states.

In Fig. S29, we show the surface states with boundary terms defined in Eqs. (S12.19) to (S12.22). We can observe the additional boundary terms have shifted the energy of the surface states and the surface states have merged into the bulk spectrum.

Finally, we discuss the surface states of the realistic model obtained from the mean-field calculations (Section X 3). For the realistic model, there are more than one d orbitals per Co, more than one f orbitals per Ce and we also have p orbitals from P atoms. Therefore, we cannot use N_+ , N_- to conclude whether f forms obstructed orbitals or not. We take an open boundary along z directions and plot the surface bands in Fig. S30. We observe multiple surface states emerge. Here, we provide several possible origins of the surface states.

From the previous simple model, we observe that there are two mechanisms that can generate surface states

- f orbitals form molecular orbitals.

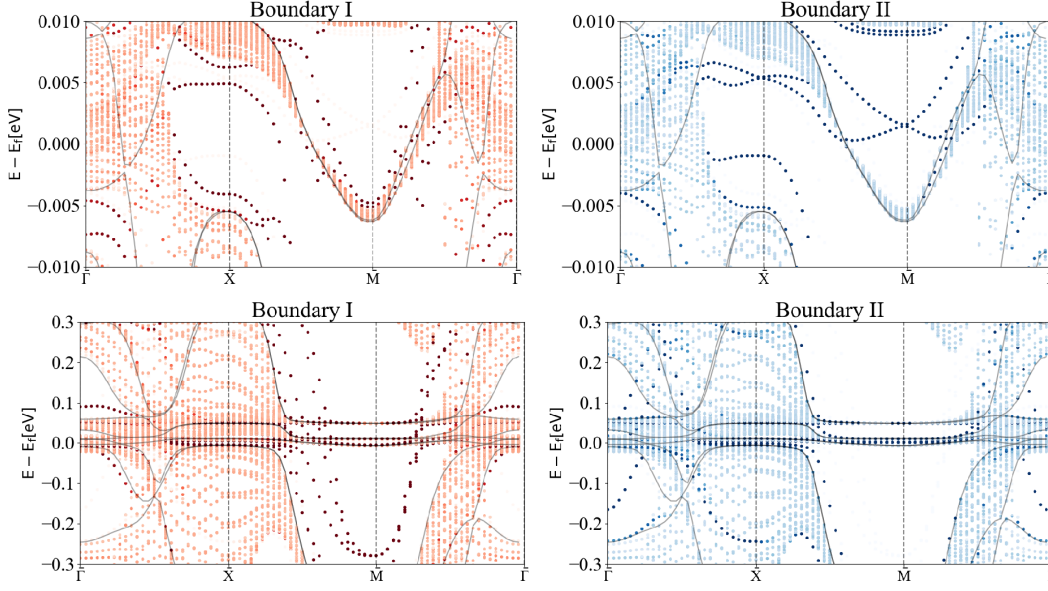


Figure S30. Surface states calculation with open boundary along z directions. Bands marked by dark red and dark blue denote the bands with large weights on the surface. The upper and lower panels represent the same surface spectrum, each displayed within distinct energy windows. In the bottom figures, we can observe several narrow surface bands that are related to the narrow bandwidth of the f electrons.

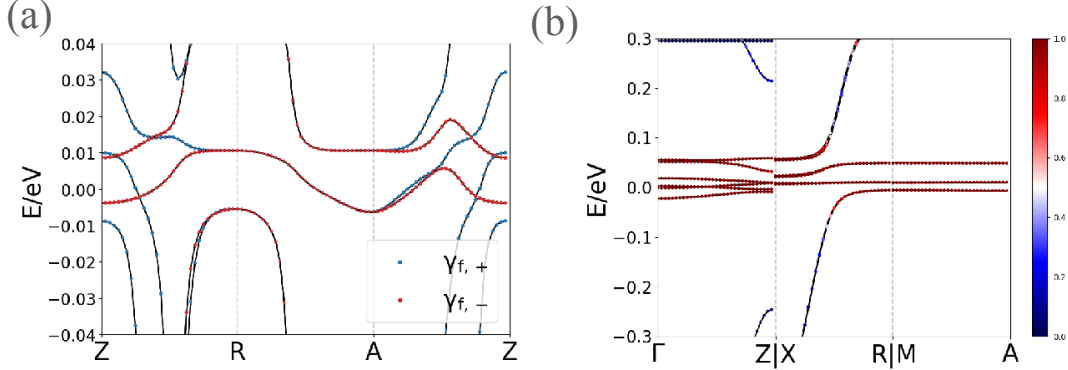


Figure S31. Band structures of the Kondo phase obtained from mean-field calculations (Section X3). (a) Red and blue denote the orbital weights of two molecular orbitals of f electrons (Eq. (S12.23)). (b) Red and blue denote the orbital weights of f and c electrons respectively, where we can observe a band inversion happens along X - R .

- Band inversion between f electrons and c electrons.

These two mechanisms may also produce surface states in the realistic model. However, the details of the surface states are different since the simple model does not include all the orbitals.

We first show the obstructed nature of f bands in the realistic model. We introduce the following molecular orbitals (for the effective 1D system) in a similar manner in Eq. (S12.18)

$$\begin{aligned}\gamma_{f,\pm,\alpha,(k_x,k_y,R_z),\uparrow} &= \frac{1}{\sqrt{2}} \left(\mp s_\alpha f(k_x,k_y,R_z), C e_{1,\alpha,\uparrow} + f(k_x,k_y,R_z), C e_{2,\alpha,\uparrow} \right) \\ \gamma_{f,\pm,\alpha,(k_x,k_y,R_z),\downarrow} &= \frac{1}{\sqrt{2}} \left(\pm s_\alpha f(k_x,k_y,R_z), C e_{1,\alpha,\downarrow} + f(k_x,k_y,R_z-1), C e_{2,\alpha,\downarrow} \right)\end{aligned}\quad (\text{S12.23})$$

where

$$\alpha = f_z^3, f_{xz^2}, f_{yz^2}, f_z(x^2-y^2), f_{xyz}, f_x(x^2-3y^2), f_y(3x^2-y^2)$$

$$S_{f_z^3, f_{x^2z}, f_{yz^2}, f_{z(x^2-y^2)}, f_{xyz}, f_{x(x^2-3y^2)}, f_{y(3x^2-y^2)}} = -1, 1, 1, -1, -1, 1, 1 \quad (\text{S12.24})$$

For the effective 1D system $\gamma_{f,\pm,\alpha,(k_x,k_y,R_z),\sigma}$ is equivalent to an s -orbital with spin $\mp\sigma$ at $R_z = 1/4$, and $\gamma_{f,\pm,\alpha,(k_x,k_y,R_z),\sigma}$ is equivalent to an s -orbital with spin $\pm\sigma$ at $R_z = 3/4$. If there is a large enough energy splitting between $\gamma_{f,+\alpha,(k_x,k_y,R_z),\sigma}$ and $\gamma_{f,-\alpha,(k_x,k_y,R_z),\sigma}$ states, we could conclude there is a formation of molecular orbitals.

In Fig. S31 (a), we plot the orbital weights of $\gamma_{f,+\alpha,(k_x,k_y,R_z),\sigma}$ and $\gamma_{f,-\alpha,(k_x,k_y,R_z),\sigma}$. We can observe the splitting between $\gamma_{f,+\alpha,(k_x,k_y,R_z),\sigma}$ bands and $\gamma_{f,-\alpha,(k_x,k_y,R_z),\sigma}$ bands near $k_x = k_y = 0$, which indicates the f -electrons tend to form molecular orbitals in the ground state. However, the corresponding surface states may merge into the bulk spectrum.

Secondly, as we show in Fig. S31 (b), a band inversion between f and c electrons also appears in the realistic model. However, in the realistic model, the band inversion appears at $k_x = 0, k_y = 1/2$ (X - R), but is absent at $k_x = k_y = 0$. This is because our simple model overestimates the z -direction hopping of $d_{x^2-y^2}$ orbitals which creates the band inversion at $k_x = k_y = 0$ in the simple model, and has ignored the d_{xz}, d_{yz} orbitals which creates the band inversion at $k_x = 0, k_y = 1/2$ in the realistic model.

Finally, there are also strong bonds formed by p_z orbitals of P atoms (as we have also discussed in Section VII, see also Fig. S14). Cutting p_z bonds could also create surface states.

In conclusion, our study demonstrates that various mechanisms can create surface states in this system. However, it is important to note that the existence of these surface states is not protected by symmetries, allowing them to potentially merge into the bulk spectrum. Moreover, it is worth mentioning that, due to the narrow bandwidth and correlation effects of f -electron systems, DFT calculations may not accurately capture all the details of the band structures. Despite the complexity of real materials, our research outlines several potential mechanisms for the generation of surface states observed in experiments, and shows there is not a topological reason for their appearances.

Appendix XIII: Schrieffer-Wolff transformation

In this section, we discuss the Schrieffer-Wolff (SW) transformation [76, 78] of generic many-body systems. In Sec. IX, we use the Schrieffer-Wolff transformation to obtain the Kondo lattice model from the periodic Anderson model. In Sec. XIV, we also use the Schrieffer-Wolff transformation to demonstrate the flat bands could induce a type-A antiferromagnetic order.

We consider an unperturbed Hamiltonian

$$H_0 = \sum_{L,i} E_{L,i} |L, i\rangle \langle L, i| + \sum_{H,i} E_{H,i} |H, i\rangle \langle H, i| \quad (\text{S13.1})$$

where $|L, i\rangle$ and $|H, i\rangle$ denote the eigenstate in the low-energy and high-energy subspaces. These eigenvalues and eigenvectors are obtained by directly diagonalizing H_0 . We then introduce the following projection operators

$$P_L = \sum_i |L, i\rangle \langle L, i|, \quad P_H = \sum_i |H, i\rangle \langle H, i| \quad (\text{S13.2})$$

We then introduce the perturbation term

$$H_1 = \sum_{ij} V_{ij} |L, i\rangle \langle H, j| + \text{h.c.} \quad (\text{S13.3})$$

The perturbation term maps a low-energy state to a high-energy state or a high-energy state to a low-energy state. We then find

$$\begin{aligned} P_L H_1 P_H &= \sum_{ij} V_{ij} |L, i\rangle \langle H, j| \\ P_H H_1 P_L &= \sum_{ij} V_{ij}^* |H, j\rangle \langle L, i| \end{aligned} \quad (\text{S13.4})$$

We next aim to obtain an effective Hamiltonian defined in the low-energy subspace that takes into account the effects of the high-energy subspace in perturbation theory.

We consider the following operators

$$S = \sum_{i,j} V_{ij} \frac{|L, i\rangle \langle H, j|}{E_{L,i} - E_{H,j}} - \sum_{i,j} V_{ij}^* \frac{|H, j\rangle \langle L, i|}{E_{L,i} - E_{H,j}} \quad (\text{S13.5})$$

We perform a unitary transformation correspondingly

$$H' = e^S (H_0 + H_1) e^{-S} = H_0 + H_1 + [S, H_0] + [S, H_1] + \frac{1}{2}[S, [S, H_0]] + \dots \quad (\text{S13.6})$$

We note that

$$\begin{aligned}
& [S, H_0] \\
&= \sum_{i,j} V_{ij} E_{H,j} \frac{|L, i\rangle \langle H, j| H, j\rangle \langle H, j|}{E_{L,i} - E_{H,j}} - \sum_{i,j} V_{ij} E_{L,i} \frac{|L, i\rangle \langle L, i| L, i\rangle \langle H, j|}{E_{L,i} - E_{H,j}} \\
&\quad - \sum_{i,j} V_{ij}^* E_{L,i} \frac{|H, j\rangle \langle L, i| L, i\rangle \langle L, i|}{E_{L,i} - E_{H,j}} + \sum_{i,j} V_{ij}^* E_{H,j} \frac{|H, j\rangle \langle H, j| H, j\rangle \langle L, i|}{E_{L,i} - E_{H,j}} \\
&= \sum_{i,j} -V_{ij} |L, i\rangle \langle H, j| - \sum_{i,j} -V_{ij}^* |H, j\rangle \langle L, i| \\
&= -H_1
\end{aligned} \tag{S13.7}$$

Therefore, the new effective Hamiltonian now becomes

$$H' \approx H_0 + H_1 - H_1 + [S, H_1] - \frac{1}{2}[S, H_1] = H_0 + \frac{1}{2}[S, H_1] \tag{S13.8}$$

We note that

$$\begin{aligned}
& [S, H_1] \\
&= \sum_{i,i',j} V_{ij} \frac{|L, i\rangle \langle H, j|}{E_{L,i} - E_{H,j}} V_{i'j}^* |H, j\rangle \langle L, i'| - \sum_{i,j,j'} V_{ij}^* \frac{|H, j\rangle \langle L, i|}{E_{L,i} - E_{H,j}} V_{ij'} |L, i\rangle \langle H, j'| \\
&\quad - \sum_{i,i',j} V_{ij} |L, i\rangle \langle H, j| (-V_{i'j}^*) \frac{|H, j\rangle \langle L, i'|}{E_{L,i'} - E_{H,j}} - \sum_{i,j,j'} V_{ij}^* |H, j\rangle \langle L, i| V_{ij'} \frac{|L, i\rangle \langle H, j'|}{E_{L,i} - E_{H,j'}} \\
&= \sum_{i,i',j} V_{ij} V_{i'j}^* \left(\frac{1}{E_{L,i} - E_{H,j}} + \frac{1}{E_{L,i'} - E_{H,j}} \right) |L, i\rangle \langle L, i'| + \sum_{i,j,j'} V_{ij}^* V_{ij'} \left(\frac{-1}{E_{L,i} - E_{H,j}} + \frac{-1}{E_{L,i} - E_{H,j'}} \right) |H, j\rangle \langle H, j'|
\end{aligned} \tag{S13.9}$$

Using Eq. S13.6, we obtain

$$\begin{aligned}
& H' \\
&\approx \sum_{L,i} E_{L,i} |L, i\rangle \langle L, i| + \sum_{H,i} E_{H,i} |H, i\rangle \langle H, i| \\
&\quad + \frac{1}{2} \sum_{i,i',j} V_{ij} V_{i'j}^* \left(\frac{1}{E_{L,i} - E_{H,j}} + \frac{1}{E_{L,i'} - E_{H,j}} \right) |L, i\rangle \langle L, i'| + \frac{1}{2} \sum_{i,j,j'} V_{ij}^* V_{ij'} \left(\frac{-1}{E_{L,i} - E_{H,j}} + \frac{-1}{E_{L,i} - E_{H,j'}} \right) |H, j\rangle \langle H, j'|
\end{aligned} \tag{S13.10}$$

Finally, we only keep the term in the low-energy subspace, which gives

$$\begin{aligned}
H_{eff} &= P_L H' P_L = H'_0 + H_{SW} \\
H'_0 &= P_L H_0 P_L = \sum_i E_{L,i} |L, i\rangle \langle L, i| \\
H_{SW} &= \frac{1}{2} \sum_{i,j,m} V_{im} V_{jm}^* \left(\frac{1}{E_{L,i} - E_{H,m}} + \frac{1}{E_{L,j} - E_{H,m}} \right) |L, i\rangle \langle L, j|
\end{aligned} \tag{S13.11}$$

H'_0 denotes the contribution from the original unperturbed Hamiltonian and H_{SW} denotes the additional contribution generated from the Schrieffer-Wolff transformation. In practice, the additional term H_{SW} describes the following virtual process

$$|L, j\rangle \xrightarrow{V_{jm}^* |H, m\rangle \langle L, j|} |H, m\rangle \xrightarrow{V_{im} |L, i\rangle \langle H, m|} |L, i\rangle \tag{S13.12}$$

where H_1 maps a low-energy state $|L, j\rangle$ to a high-energy state $|H, m\rangle$ and then map the high-energy state $|H, m\rangle$ back to a low-energy state $|L, i\rangle$

Appendix XIV: Flat-band ferromagnetism/anti-ferromagnetism

In this section, we demonstrate that a relatively flat band that is atomic along z direction and non-atomic along x, y directions leads to a type-A antiferromagnetism (in-plane magnetism and out-of-plane antiferromagnetism).

Several comments are in order:

- In this section, we will pick a toy model to demonstrate the ferromagnetism/antiferromagnetism tendency induced by flat bands.
- We will consider the case of a half-filled single flat band to simplify the considerations.
- We will ignore the contributions of the other dispersive bands. The flat band, when it appears near Fermi energy, induces a large density of states. We expect the leading-order instability to be generated by flat bands instead of dispersive bands.
- We comment that the real materials are more complicated, in which the flat bands are not perfectly flat and the dispersive bands could also make contributions. However, based on the toy model we considered in this appendix and the more realistic DFT model we discussed in Appendix VI, we could conclude that flat bands (atomic along z direction and non-atomic along xy direction) indeed favor the type-A antiferromagnetism.

In Sec. XIV 1, we will show that a 2D flat band which is non-atomic along xy directions leads to an in-plane ferromagnetism. In Sec. XIV 2, we show that, a weak hopping along z directions leads to an antiferromagnetic coupling along z direction and stabilizes a type-A antiferromagnetism.

1. Ferromagnetism from 2D non-atomic flat band

In this section, we provide more understanding of the ferromagnetism induced by flat bands, based on a single-flat-band toy model. We use $d_{\mathbf{k},\alpha,\sigma}$ to denote the electron operators with momentum \mathbf{k} , orbital α and spin σ .

We assume a flat band (with two-fold degeneracy due to $SU(2)$ spin symmetry) can be described by the following electron operators in the band basis

$$\gamma_{\mathbf{k},\sigma} = \sum_{\alpha} V_{\alpha}^*(\mathbf{k}) d_{\mathbf{k},\alpha,\sigma} \quad (\text{S14.1})$$

$V_{\alpha}(\mathbf{k})$ describes the wavefunction of the flat band. We assume $V_{\alpha}(\mathbf{k})$ is k_z -independent since the flat band is atomic along z direction.

We first consider perfect flat bands with the kinetic term in the band basis taken to be

$$H_0 = \sum_{\mathbf{k},\sigma} E_0 \gamma_{\mathbf{k},\sigma}^{\dagger} \gamma_{\mathbf{k},\sigma} \quad (\text{S14.2})$$

To simplify the calculations, we consider the case where the flat band is half-filled at the non-interacting limit with $E_0 = 0$. We next consider the interaction term. We take the following density-density interactions characterized by interaction matrix $U_{\alpha\gamma}$ with $U_{\alpha\gamma} = U_{\gamma\alpha} > 0$ (we also drop the Hund's coupling term here, since it is usually small compared to the density-density interactions)

$$H_U = \sum_{\alpha,\mathbf{R},\sigma,\sigma'} \frac{U_{\alpha\gamma}}{2} \left(P : d_{\mathbf{R},\alpha,\sigma}^{\dagger} d_{\mathbf{R},\alpha,\sigma} : P \right) \left(P : d_{\mathbf{R},\gamma,\sigma'}^{\dagger} d_{\mathbf{R},\gamma,\sigma'} : P \right) \quad (\text{S14.3})$$

where P is the projection operator that projects the electron operator to the band basis

$$P d_{\mathbf{k},\alpha,\sigma} P = V_{\alpha}(\mathbf{k}) \gamma_{\mathbf{k},\sigma} \quad (\text{S14.4})$$

and $::$ denotes normal ordering. We consider the case of $E_0 = 0$. Then we have $\langle \gamma_{\mathbf{k},\alpha,\sigma}^{\dagger} \gamma_{\mathbf{k}+\mathbf{q},\gamma,\sigma} \rangle_0 = \delta_{\mathbf{q},0} \delta_{\alpha,\gamma}$ which corresponds to the half-filling of flat bands. The projected density operators can then be written as

$$\begin{aligned} & : P d_{\mathbf{R},\alpha,\sigma}^{\dagger} d_{\mathbf{R},\alpha,\sigma} P : \\ &= \sum_{\mathbf{k},\mathbf{q}} \frac{e^{+i\mathbf{q}\cdot(\mathbf{R}+\mathbf{r}_{\alpha})}}{N} V_{\alpha}^*(\mathbf{k}) V_{\alpha}(\mathbf{k}+\mathbf{q}) \gamma_{\mathbf{k},\alpha,\sigma}^{\dagger} \gamma_{\mathbf{k}+\mathbf{q},\alpha,\sigma} - \left\langle \sum_{\mathbf{k},\mathbf{q}} \frac{e^{+i\mathbf{q}\cdot(\mathbf{R}+\mathbf{r}_{\alpha})}}{N} V_{\alpha}^*(\mathbf{k}) V_{\alpha}(\mathbf{k}+\mathbf{q}) \gamma_{\mathbf{k},\alpha,\sigma}^{\dagger} \gamma_{\mathbf{k}+\mathbf{q},\alpha,\sigma} \right\rangle_0 \end{aligned}$$

$$= \sum_{\mathbf{k}, \mathbf{q}} \frac{e^{+i\mathbf{q} \cdot (\mathbf{R} + \mathbf{r}_\alpha)}}{N} V_\alpha^*(\mathbf{k}) V_\alpha(\mathbf{k} + \mathbf{q}) \left(\gamma_{\mathbf{k}, \alpha, \sigma}^\dagger \gamma_{\mathbf{k} + \mathbf{q}, \alpha, \sigma} - \frac{1}{2} \delta_{\mathbf{q}, 0} \right) \quad (\text{S14.5})$$

The interaction term can be written as

$$H_U = \sum_{\alpha, \gamma, \mathbf{k}, \mathbf{k}', \mathbf{q}, \sigma, \sigma'} \frac{U_{\alpha\gamma}}{2N} V_\alpha^*(\mathbf{k}) V_\alpha(\mathbf{k} + \mathbf{q}) V_\gamma^*(\mathbf{k}' + \mathbf{q}) V_\gamma(\mathbf{k}') \left(\gamma_{\mathbf{k}, \sigma}^\dagger \gamma_{\mathbf{k} + \mathbf{q}, \sigma} - \frac{\delta_{\mathbf{q}, 0}}{2} \right) \left(\gamma_{\mathbf{k}' + \mathbf{q}, \sigma'}^\dagger \gamma_{\mathbf{k}', \sigma'} - \frac{\delta_{\mathbf{q}, 0}}{2} \right) \quad (\text{S14.6})$$

The total Hamiltonian is

$$\begin{aligned} H &= H_0 + H_U \\ &= \sum_{\alpha, \gamma, \mathbf{k}, \mathbf{k}', \mathbf{q}, \sigma, \sigma'} \frac{U_{\alpha\gamma}}{2N} V_\alpha^*(\mathbf{k}) V_\alpha(\mathbf{k} + \mathbf{q}) V_\gamma^*(\mathbf{k}' + \mathbf{q}) V_\gamma(\mathbf{k}') \left(\gamma_{\mathbf{k}, \sigma}^\dagger \gamma_{\mathbf{k} + \mathbf{q}, \sigma} - \frac{\delta_{\mathbf{q}, 0}}{2} \right) \left(\gamma_{\mathbf{k}' + \mathbf{q}, \sigma'}^\dagger \gamma_{\mathbf{k}', \sigma'} - \frac{\delta_{\mathbf{q}, 0}}{2} \right) \end{aligned} \quad (\text{S14.7})$$

where we take $E_0 = 0$.

We now aim to rewrite the Hamiltonian in a more compact formula. We can perform an eigen-decomposition of the interaction matrix $U_{\alpha\gamma}$

$$U_{\alpha\gamma} = \sum_{n=1, \dots, n_{orb}} u_n v_{\alpha n} v_{\gamma n}^* \quad (\text{S14.8})$$

with u_n and $v_{\alpha n}$ are eigenvalues and eigenvectors of $U_{\alpha\gamma}$ matrix. n_{orb} denotes the number of orbitals. The Hamiltonian now becomes (using Eq. S14.7, and Eq. S14.8)

$$H = \sum_{n, \mathbf{q}} \frac{u_n}{2N} \left[\sum_{\mathbf{k}, \sigma, \alpha} v_{\alpha n} V_\alpha^*(\mathbf{k}) V_\alpha(\mathbf{k} + \mathbf{q}) \left(\gamma_{\mathbf{k}, \sigma}^\dagger \gamma_{\mathbf{k} + \mathbf{q}, \sigma} - \frac{\delta_{\mathbf{q}, 0}}{2} \right) \right] \left[\sum_{\mathbf{k}', \sigma', \gamma} v_{\gamma n}^* V_\gamma(\mathbf{k}') V_\gamma^*(\mathbf{k}' + \mathbf{q}) \left(\gamma_{\mathbf{k}' + \mathbf{q}, \sigma'}^\dagger \gamma_{\mathbf{k}', \sigma'} - \frac{\delta_{\mathbf{q}, 0}}{2} \right) \right] \quad (\text{S14.9})$$

Therefore, we find

$$H = \sum_{n, \mathbf{q}} \frac{u_n}{2} O_{n, \mathbf{q}} O_{n, \mathbf{q}}^\dagger \quad (\text{S14.10})$$

with

$$O_{n, \mathbf{q}} = \frac{1}{\sqrt{N}} \sum_{\mathbf{k}, \sigma, \alpha} v_{\alpha n} V_\alpha^*(\mathbf{k}) V_\alpha(\mathbf{k} + \mathbf{q}) \left(\gamma_{\mathbf{k}, \sigma}^\dagger \gamma_{\mathbf{k} + \mathbf{q}, \sigma} - \frac{\delta_{\mathbf{q}, 0}}{2} \right) \quad (\text{S14.11})$$

We now discuss the values of v_n which are the eigenvalues of $U_{\alpha\gamma}$. In general, we expect v_n to be positive. The negative v_n indicates an attractive interaction in certain channels. This could then lead to additional instability such as orbital ordering. To observe this, we take a two-orbital case as an example. The interaction matrix of a two-orbital model can be written as

$$U_{\alpha\gamma} = \begin{bmatrix} U_1 & U_2 \\ U_2 & U_1 \end{bmatrix}_{\alpha\gamma} \quad (\text{S14.12})$$

where U_1, U_2 denotes intra and inter-orbital interactions. Obviously, the eigenvalues of the interaction matrix are $U_1 + U_2, U_1 - U_2$. If $U_2 > U_1$, one of the eigenvalues becomes negative. To observe its consequence, we could write the interaction term via density operators as

$$\sum_{\mathbf{R}} \left[\frac{U_1}{2} (\nu_{\mathbf{R}, 1}^2 + \nu_{\mathbf{R}, 2}^2) + U_2 \nu_{\mathbf{R}, 1} \nu_{\mathbf{R}, 2} \right] = \sum_{\mathbf{R}} \left[\frac{U_1 + U_2}{4} (\nu_{\mathbf{R}, 1} + \nu_{\mathbf{R}, 2})^2 + \frac{U_1 - U_2}{4} (\nu_{\mathbf{R}, 1} - \nu_{\mathbf{R}, 2})^2 \right] \quad (\text{S14.13})$$

with the density operator defined as

$$\nu_{\mathbf{R}, \alpha} = \sum_{\sigma} : d_{\mathbf{R}, \alpha \sigma}^\dagger d_{\mathbf{R}, \alpha \sigma} : \quad (\text{S14.14})$$

We note that, if $U_1 - U_2 < 0$, the system minimizes the energy by only filling one of the two orbitals (maximizing $|\nu_{\mathbf{R}, 1} - \nu_{\mathbf{R}, 2}|$), which could induce an orbital ordering.

However, for the generic system, the diagonal components of $U_{\alpha\gamma}$ (which corresponds to the intra-orbital repulsion) are usually stronger than the off-diagonal components (which correspond to the inter-orbital repulsion). The strong enough diagonal components of $U_{\alpha\gamma}$ matrix could make all the eigenvalues positive $u_n > 0$. In the current case, since we are mostly interested in the formation of magnetism (instead of orbital ordering), we will assume $u_n \geq 0$ for all n .

When $u_n > 0$,

$$H = \sum_{n,q} \frac{u_n}{2} O_{n,\mathbf{q}} O_{n,\mathbf{q}}^\dagger \quad (\text{S14.15})$$

becomes a positive semi-definite Hamiltonian. The state $|\phi\rangle$ that satisfy

$$O_{n,\mathbf{q}}^\dagger |\phi\rangle = 0, \quad \forall n, \mathbf{q} \quad (\text{S14.16})$$

would be the ground state [127].

Since we assume the system is an effective 2D system where $V_\alpha(\mathbf{k})$ is k_z independent, we treat xy directions and z direction separately. We use $\mathbf{k}^{xy}, \mathbf{q}^{xy}$ to denote the in-plane components of the vector with $\mathbf{k}^{xy} = (k_x, k_y), \mathbf{q}^{xy} = (q_x, q_y)$. Therefore, we can rewrite $O_{n,\mathbf{q}}^\dagger$ as

$$O_{n,\mathbf{q}}^\dagger = \frac{1}{\sqrt{N}} \sum_{\mathbf{k}^{xy}, \alpha, \sigma} v_{\alpha n}^* V_\alpha^*(\mathbf{k}^{xy} + \mathbf{q}^{xy}) V_\alpha(\mathbf{k}^{xy}) \sum_{k_z} (\gamma_{(\mathbf{k}^{xy} + \mathbf{q}^{xy}, k_z + q^z), \sigma}^\dagger \gamma_{(\mathbf{k}^{xy}, k^z), \sigma} - \frac{\delta_{\mathbf{q}^{xy}, 0} \delta_{q^z, 0}}{2}) \quad (\text{S14.17})$$

Since the system is atomic along z direction, we can perform Fourier transformation along z direction with

$$\gamma_{(\mathbf{k}^{xy}, R_z), \sigma} = \frac{1}{\sqrt{L_z}} \sum_{\mathbf{R}} \gamma_{(\mathbf{k}^{xy}, k_z), \sigma} e^{ik_z R_z} \quad (\text{S14.18})$$

where L_α is the system size along α direction with the total number of unit cells $N = L_x L_y L_z$. Then we find

$$\begin{aligned} O_{n,(\mathbf{q}^{xy}, R_z)}^\dagger &= \frac{1}{\sqrt{L_z}} \sum_{q_z} O_{n,(\mathbf{q}^{xy}, q^z)}^\dagger e^{-iq_z R_z} \\ &= \frac{1}{\sqrt{N_{xy}}} \sum_{\mathbf{k}^{xy}, \alpha, \sigma} v_{\alpha n}^* V_\alpha^*(\mathbf{k}^{xy} + \mathbf{q}^{xy}) V_\alpha(\mathbf{k}) (\gamma_{(\mathbf{k}^{xy} + \mathbf{q}^{xy}, R_z), \sigma}^\dagger \gamma_{(\mathbf{k}^{xy}, R_z), \sigma} - \frac{\delta_{\mathbf{q}^{xy}, 0}}{2}) \end{aligned} \quad (\text{S14.19})$$

where $N_{xy} = L_x L_y$. The Hamiltonian now can be written as

$$H_0 + H_U = \sum_{n, \mathbf{q}^{xy}, R_z} \frac{u_n}{2} O_{n,(\mathbf{q}^{xy}, R_z)} O_{n,(\mathbf{q}^{xy}, R_z)}^\dagger \quad (\text{S14.20})$$

where we can observe that the Hamiltonian of each layer is decoupled. We now solve the positive semidefinite Hamiltonian of each R_z layer

$$H_{R_z} = \sum_{n, \mathbf{q}^{xy}} \frac{u_n}{2} O_{\alpha,(\mathbf{q}^{xy}, R_z)} O_{\alpha,(\mathbf{q}^{xy}, R_z)}^\dagger \quad (\text{S14.21})$$

We now prove that the following states are the ground states of H_{R_z}

$$|R_z\rangle = \prod_{\mathbf{k}^{xy}} \gamma_{(\mathbf{k}^{xy}, R_z), \uparrow}^\dagger |0\rangle \quad (\text{S14.22})$$

where $|0\rangle$ is the vacuum state. We prove it by showing

$$O_{\alpha,(\mathbf{q}^{xy}, R_z)}^\dagger |R_z\rangle = 0 \quad (\text{S14.23})$$

Written explicitly, we have

$$\begin{aligned} &O_{n,(\mathbf{q}^{xy}, R_z)}^\dagger |R_z\rangle \\ &= \frac{1}{\sqrt{N_{xy}}} \sum_{\mathbf{k}^{xy}, \alpha, \sigma} v_{\alpha n}^* V_\alpha^*(\mathbf{k}^{xy} + \mathbf{q}^{xy}) V_\alpha(\mathbf{k}) (\gamma_{(\mathbf{k}^{xy} + \mathbf{q}^{xy}, R_z), \sigma}^\dagger \gamma_{(\mathbf{k}^{xy}, R_z), \sigma} - \frac{1}{2} \delta_{\mathbf{q}^{xy}, 0}) \prod_{\mathbf{k}^{xy}} \gamma_{(\mathbf{k}^{xy}, R_z), \uparrow}^\dagger |0\rangle \end{aligned}$$

$$\begin{aligned}
&= \frac{1}{\sqrt{N_{xy}}} \sum_{\mathbf{k}^{xy}, \alpha} v_{\alpha n}^* V_{\alpha}^*(\mathbf{k}^{xy} + \mathbf{q}^{xy}) V_{\alpha}(\mathbf{k}) \left(\frac{\delta_{\mathbf{q}^{xy}, 0}}{2} - \gamma_{(\mathbf{k}^{xy}, R_z), \uparrow} \gamma_{(\mathbf{k}^{xy} + \mathbf{q}^{xy}, R_z), \uparrow}^{\dagger} \right) \prod_{\mathbf{k}^{xy}} \gamma_{(\mathbf{k}^{xy}, R_z), \uparrow}^{\dagger} |0\rangle \\
&\quad + \frac{1}{\sqrt{N_{xy}}} \sum_{\mathbf{k}^{xy}, \alpha, \sigma = \downarrow} v_{\alpha n}^* V_{\alpha}^*(\mathbf{k}^{xy} + \mathbf{q}^{xy}) V_{\alpha}(\mathbf{k}) \left(-\frac{\delta_{\mathbf{q}^{xy}, 0}}{2} \right) \prod_{\mathbf{k}^{xy}} \gamma_{(\mathbf{k}^{xy}, R_z), \uparrow}^{\dagger} |0\rangle \\
&= 0
\end{aligned} \tag{S14.24}$$

Therefore, $|R_z\rangle$ is the ground states of H_{R_z} . The ground state in Eq. S14.22 defines a state where the spin \uparrow flavor of the flat band is fully filled. Due to the $SU(2)$ rotation symmetry, all the other states obtained by acting $SU(2)$ symmetry on the $|R_z\rangle$ are also ground states. The states obtained by $SU(2)$ transformation can be written as

$$|R_z, \theta(R_z), \phi(R_z)\rangle = \hat{R}_{R_z}(\theta(R_z), \phi(R_z)) |R_z\rangle \tag{S14.25}$$

where $\hat{R}_{R_z}(\theta, \phi)$ describes the following $SU(2)$ symmetry transformation

$$\hat{R}_{R_z}(\theta, \phi) \gamma_{\mathbf{k}^{xy}, R_z, \uparrow}^{\dagger} \hat{R}_{R_z}^{\dagger}(\theta, \phi) = \cos(\theta) e^{i\phi} \gamma_{\mathbf{k}^{xy}, R_z, \uparrow}^{\dagger} + \sin(\theta) \gamma_{\mathbf{k}^{xy}, R_z, \downarrow}^{\dagger} \tag{S14.26}$$

Therefore a generic ground state of the whole system can be obtained by taking the tensor product of the ground state of each layer

$$|\theta, \phi\rangle = \bigotimes_{R_z} |R_z, \theta(R_z), \phi(R_z)\rangle \tag{S14.27}$$

where θ, ϕ are functions of R_z that characterize the $SU(2)$ rotation of each layer. Since the system is decoupled along z direction (in the case of zero z -direction hopping), we observe the relative spin directions of different layers can be arbitrary. In other words, there is no z direction magnetic order.

a. Orthonormal basis

The ground states of the Hamiltonian characterized by

$$|\theta, \phi\rangle = \bigotimes_{R_z} |R_z, \theta(R_z), \phi(R_z)\rangle \tag{S14.28}$$

have a large degeneracy. Moreover, the set of ground states, $\{|\theta, \phi\rangle | \theta \in [0, \pi), \phi \in [0, 2\pi)\}$, does not form an orthonormal basis of the ground-state manifold.

For future convenience, we now aim to find the orthonormal basis of the ground-state manifold. For layer R_z , the ground state is characterized by

$$|R_z, \theta(R_z), \phi(R_z)\rangle \tag{S14.29}$$

The Hamiltonian has a $SU(2)$ symmetry for each layer. The generators of $SU(2)$ group (or the spin operators) are

$$S_{R_z}^{x,y,z} = \sum_{\mathbf{k}^{xy}, \sigma, \sigma'} \gamma_{(\mathbf{k}^{xy}, R_z), \sigma}^{\dagger} \frac{\sigma_{\sigma\sigma'}^{x,y,z}}{2} \gamma_{(\mathbf{k}^{xy}, R_z), \sigma'} \tag{S14.30}$$

where $\sigma^{x,y,z}$ are Pauli matrices. We find the ground states of layer R_z which are characterized by $\{|R_z, \theta(R_z), \phi(R_z)\rangle\}_{\theta(R_z), \phi(R_z)}$ form a spin $S = (N_{xy}/2)$ representation of the $SU(2)$ group, where N_{xy} denotes number of unit cells for each layer. The spin $S = (N_{xy}/2)$ representation corresponds to the ferromagnetic state where all the filled flat-band electrons have the same spin direction. To show the ground states indeed form $S = (N_{xy}/2)$ representation, we calculate

$$\begin{aligned}
&\sum_{\mu} (S_{R_z}^{\mu})^2 |R_z, \theta(R_z), \phi(R_z)\rangle = \sum_{\mu} (S_{R_z}^{\mu})^2 \hat{R}_{R_z}(\theta(R_z), \phi(R_z)) |R_z, 0, 0\rangle = \hat{R}_{R_z}(\theta(R_z), \phi(R_z)) \sum_{\mu} (S_{R_z}^{\mu})^2 |R_z, 0, 0\rangle \\
&= S(S+1) \hat{R}_{R_z}(\theta(R_z), \phi(R_z)) |R_z, 0, 0\rangle = S(S+1) |R_z, \theta(R_z), \phi(R_z)\rangle
\end{aligned} \tag{S14.31}$$

where we use the fact that the Casimir operator $\sum_{\mu} (S_{R_z}^{\mu})^2$ commutes with the $SU(2)$ rotation operator $\hat{R}_{R_z}(\theta(R_z), \phi(R_z))$. From Eq. S14.31, we conclude the ground states form $S = (N_{xy}/2)$ representation.

Since the degenerate ground states form an $S = (N_{xy}/2)$ representation, we can then use the eigenstates of $S_{R_z}^z$ operator and the ladder operators to build the orthonormal basis of the ground-state manifolds. We introduce the following orthonormal states to characterize the ground-state manifolds

$$\begin{aligned} & \{|R_z, M\rangle\}_{M=-S}^{M=S} \\ & S_{R_z}^z |R_z, M\rangle = M |R_z, M\rangle, \quad \sum_{\mu} (S_{R_z}^{\mu})^2 |R_z, M\rangle = S(S+1) |R_z, M\rangle \end{aligned} \quad (\text{S14.32})$$

The above orthonormal basis can be obtained by acting ladder operators on the $|R_z, \theta(R_z) = 0, \phi(R_z) = 0\rangle$. In other words, we can let

$$\begin{aligned} |R_z, M = S\rangle &= |R_z, \theta(R_z) = 0, \phi(R_z) = 0\rangle \\ |R_z, M - 1\rangle &= \frac{S_{R_z}^-}{\sqrt{S(S+1) - M(M-1)}} |R_z, M\rangle \end{aligned} \quad (\text{S14.33})$$

where $S_{R_z}^- = S_{R_z}^+ - iS_{R_z}^-$ is the spin ladder operator.

We now prove we can indeed construct $|R_z, M\rangle$ via Eq. S14.33. We first prove that $|R_z, \theta(R_z) = 0, \phi(R_z) = 0\rangle$ is the eigenstate of $S_{R_z}^z$ operator with eigenvalue S :

$$\begin{aligned} S_{R_z}^z |R_z, \theta(R_z) = 0, \phi(R_z) = 0\rangle &= \frac{1}{2} \sum_{\mathbf{k}^{xy}, \sigma} \sigma \gamma_{(\mathbf{k}^{xy}, R_z), \sigma}^{\dagger} \gamma_{(\mathbf{k}^{xy}, R_z), \sigma} \prod_{\mathbf{q}^{xy}} \gamma_{(\mathbf{q}^{xy}, R_z), \uparrow}^{\dagger} |0\rangle = \frac{N_{xy}}{2} \prod_{\mathbf{q}^{xy}} \gamma_{(\mathbf{q}^{xy}, R_z), \uparrow}^{\dagger} |0\rangle \\ &= S |R_z, \theta(R_z) = 0, \phi(R_z) = 0\rangle \end{aligned} \quad (\text{S14.34})$$

Therefore, $|R_z, \theta(R_z) = 0, \phi(R_z) = 0\rangle = |R_z, M = S\rangle$.

We next show that, for a given $|R_z, M\rangle$, we can generate $|R_z, M - 1\rangle$ by acting spin ladder operator ($S_{R_z}^- = S_{R_z}^+ - iS_{R_z}^-$) on $|R_z, M\rangle$. Via spin commutation relation, we find

$$\begin{aligned} S_{R_z}^z \left(\frac{S_{R_z}^-}{\sqrt{S(S+1) - M(M-1)}} |R_z, M\rangle \right) &= \left(S_{R_z}^- S_{R_z}^z - S_{R_z}^- \right) \frac{1}{\sqrt{S(S+1) - M(M-1)}} |R_z, M\rangle \\ &= \left(\frac{S_{R_z}^-}{\sqrt{S(S+1) - M(M-1)}} (M-1) |R_z, M\rangle \right) \\ &= (M-1) \left(\frac{S_{R_z}^-}{\sqrt{S(S+1) - M(M-1)}} |R_z, M\rangle \right) \end{aligned} \quad (\text{S14.35})$$

where the additional $\frac{1}{\sqrt{S(S+1) - M(M-1)}}$ factor ensures the normalization condition $\langle R_z, M | R_z, M \rangle = 1$. Therefore, we prove that, we can construct $|R_z, M - 1\rangle$ state from $|R_z, M\rangle$ state via Eq. S14.33 (second line).

We can also rewrite Eq. S14.33 as following

$$\begin{aligned} |R_z, M\rangle &= \alpha_{S, M} (S_{R_z}^-)^{S-M} |R_z, S\rangle \\ \alpha_{S, S} &= 1 \\ \alpha_{S, M} &= \left(\prod_{i=M}^{S-1} \frac{1}{\sqrt{S(S+1) - i(i+1)}} \right), \quad \text{for } M < S \end{aligned} \quad (\text{S14.36})$$

where $\alpha_{S, M}$ is the normalization factor to ensure $\langle R_z, M | R_z, M \rangle = 1$.

Taking the tensor product of the states from different layers, we can introduce the following orthogonal basis for the ground-state manifold

$$\{|m\rangle\}, \quad |m\rangle = \bigotimes_{R_z} |R_z, m(R_z)\rangle \quad (\text{S14.37})$$

where we have defined m as a function of R_z with $m(R_z)$ characterizes the states of layer R_z .

b. Charge ± 1 excitation state

After finding the ground states, we can also calculate the charge ± 1 excitation. The charge ± 1 excitation will be useful when we study the z -direction correlation induced by weak z -direction hopping via perturbation theory.

Since different layers are decoupled, we could treat each layer separately. The charge -1 excitation state with in-plane momentum \mathbf{k}^{xy} , layer index R_z and spin σ can be described by

$$\gamma_{(\mathbf{k}^{xy}, R_z), \sigma} |R_z, m(R_z)\rangle \quad (\text{S14.38})$$

We now show that the state in Eq. S14.38 is an eigenstate of the interaction Hamiltonian by proving

$$[(H_0 + H_U), \gamma_{(\mathbf{k}^{xy}, R_z), \sigma}] |R_z, m(R_z)\rangle = E_{\mathbf{k}^{xy}, R_z}^{hole} \gamma_{(\mathbf{k}^{xy}, R_z), \sigma} |R_z, m(R_z)\rangle \quad (\text{S14.39})$$

with $E_{\mathbf{k}^{xy}}^{hole}$ the corresponding energy of the excitation state.

We first calculate

$$[H_U + H_0, \gamma_{\mathbf{k}^{xy}, R_z, \sigma}] \quad (\text{S14.40})$$

We note that

$$\begin{aligned} & [O_{n, (\mathbf{q}^{xy}, R_z)}^\dagger, \gamma_{\mathbf{p}^{xy}, R'_z, \sigma''}] \\ &= \frac{1}{\sqrt{N_{xy}}} \sum_{\mathbf{k}^{xy}, \alpha, \sigma} v_{\alpha n}^* V_\alpha^*(\mathbf{k}^{xy} + \mathbf{q}^{xy}) V_\alpha(\mathbf{k}) [\gamma_{(\mathbf{k}^{xy} + \mathbf{q}^{xy}, R_z), \sigma}^\dagger \gamma_{(\mathbf{k}^{xy}, R_z), \sigma} \gamma_{(\mathbf{p}^{xy}, R'_z), \sigma''}] \\ &= \delta_{R_z, R'_z} \frac{1}{\sqrt{N_{xy}}} \sum_{\alpha} v_{\alpha n}^* V_\alpha^*(\mathbf{p}^{xy}) V_\alpha(\mathbf{p}^{xy} - \mathbf{q}^{xy}) (-\gamma_{(\mathbf{p}^{xy} - \mathbf{q}^{xy}, R_z), \sigma''}) \end{aligned} \quad (\text{S14.41})$$

and then

$$\begin{aligned} & [O_{n, (\mathbf{q}^{xy}, R_z)} O_{n, (\mathbf{q}^{xy}, R_z)}^\dagger, \gamma_{\mathbf{p}^{xy}, R'_z, \sigma''}] \\ &= \delta_{R_z, R'_z} \frac{1}{N_{xy}} \sum_{\alpha, \gamma} v_{\alpha n}^* v_{\gamma n} \sum_{\mathbf{k}} V_\alpha^*(\mathbf{p}^{xy}) V_\alpha(\mathbf{p}^{xy} - \mathbf{q}^{xy}) V_\gamma(\mathbf{k}^{xy} + \mathbf{q}^{xy}) V_\gamma^*(\mathbf{k}^{xy}) \\ & \quad [\gamma_{(\mathbf{k}^{xy}, R_z), \sigma}^\dagger \gamma_{(\mathbf{k}^{xy} + \mathbf{q}^{xy}, R_z), \sigma} (-\gamma_{(\mathbf{p}^{xy} - \mathbf{q}^{xy}, R_z), \sigma''})] \\ &= \delta_{R_z, R'_z} \frac{1}{N_{xy}} \sum_{\alpha, \gamma} v_{\alpha n}^* v_{\gamma n} V_\alpha^*(\mathbf{p}^{xy}) V_\alpha(\mathbf{p}^{xy} - \mathbf{q}^{xy}) V_\gamma(\mathbf{p}^{xy}) V_\gamma^*(\mathbf{p}^{xy} - \mathbf{q}^{xy}) \gamma_{(\mathbf{p}^{xy}, R_z), \sigma''} \end{aligned} \quad (\text{S14.42})$$

Then we have

$$\begin{aligned} & [H_U + H_0, \gamma_{\mathbf{p}^{xy}, R_z, \sigma}] \\ &= \sum_{\mathbf{q}^{xy}, n} \frac{u_n}{2N_{xy}} \sum_{\alpha, \gamma} v_{\alpha n}^* v_{\gamma n} V_\alpha^*(\mathbf{p}^{xy}) V_\alpha(\mathbf{p}^{xy} - \mathbf{q}^{xy}) V_\gamma(\mathbf{p}^{xy}) V_\gamma^*(\mathbf{p}^{xy} - \mathbf{q}^{xy}) \gamma_{(\mathbf{p}^{xy}, R_z), \sigma} \\ &= E_{\mathbf{p}^{xy}, R_z}^{hole} \gamma_{(\mathbf{p}^{xy}, R_z), \sigma} \end{aligned} \quad (\text{S14.43})$$

where

$$E_{\mathbf{p}^{xy}}^{hole} = \sum_{\mathbf{q}^{xy}, n} \frac{u_n}{2N_{xy}} \sum_{\alpha, \gamma} v_{\alpha n}^* v_{\gamma n} V_\alpha^*(\mathbf{p}^{xy}) V_\alpha(\mathbf{p}^{xy} - \mathbf{q}^{xy}) V_\gamma(\mathbf{p}^{xy}) V_\gamma^*(\mathbf{p}^{xy} - \mathbf{q}^{xy}) \quad (\text{S14.44})$$

Therefore, we have proved that

$$[(H_0 + H_U), \gamma_{(\mathbf{k}^{xy}, R_z), \sigma}] |R_z, m(R_z)\rangle = E_{\mathbf{k}^{xy}}^{hole} \gamma_{(\mathbf{k}^{xy}, R_z), \sigma} |R_z, m(R_z)\rangle \quad (\text{S14.45})$$

This indicates, as long as,

$$\gamma_{(\mathbf{k}^{xy}, R_z), \sigma'} |R_z, m(R_z)\rangle \neq 0 \quad (\text{S14.46})$$

$\gamma_{(\mathbf{k}^{xy}, R_z), \sigma'} |R_z, m(R_z)\rangle$ describes a charge -1 excitation state with energy $E_{\mathbf{k}^{xy}}^{hole}$.

We now aim to find the situation where Eq. S14.46 holds. We evaluate the following equations explicitly

$$\gamma_{(\mathbf{k}^{xy}, R_z), \sigma'} |R_z, m(R_z)\rangle \quad (\text{S14.47})$$

We first note the following commutation relations

$$\begin{aligned} [\gamma_{(\mathbf{k}^{xy}, R_z), \uparrow}^\dagger, S_{R_z}^-] &= -\gamma_{(\mathbf{k}^{xy}, R_z), \downarrow}^\dagger, \quad [\gamma_{(\mathbf{k}^{xy}, R_z), \uparrow}, S_{R_z}^-] = 0 \\ [\gamma_{(\mathbf{k}^{xy}, R_z), \downarrow}^\dagger, S_{R_z}^-] &= 0, \quad [\gamma_{(\mathbf{k}^{xy}, R_z), \downarrow}, S_{R_z}^-] = \gamma_{(\mathbf{k}^{xy}, R_z), \uparrow} \end{aligned} \quad (\text{S14.48})$$

and

$$\begin{aligned} [(S_{R_z}^-)^n, H] &= 0 \\ [\gamma_{(\mathbf{k}^{xy}, R_z), \uparrow}^\dagger, (S_{R_z}^-)^n] &= -n(S_{R_z}^-)^{n-1} \gamma_{(\mathbf{k}^{xy}, R_z), \downarrow}^\dagger, \quad [\gamma_{(\mathbf{k}^{xy}, R_z), \uparrow}, (S_{R_z}^-)^n] = 0 \\ [\gamma_{(\mathbf{k}^{xy}, R_z), \downarrow}^\dagger, (S_{R_z}^-)^n] &= 0, \quad [\gamma_{(\mathbf{k}^{xy}, R_z), \downarrow}, (S_{R_z}^-)^n] = n(S_{R_z}^-)^{n-1} \gamma_{(\mathbf{k}^{xy}, R_z), \uparrow} \end{aligned} \quad (\text{S14.49})$$

Combining Eq. S14.36 and Eq. S14.49, we find

$$\begin{aligned} \gamma_{(\mathbf{k}^{xy}, R_z), \uparrow} |R_z, m(R_z)\rangle &= \alpha_{S, m(R_z)} \left(1 - \delta_{m(R_z), -S}\right) \gamma_{(\mathbf{k}^{xy}, R_z), \uparrow} (S_{R_z}^-)^{S-m(R_z)} |R_z, S\rangle \\ &= \alpha_{S, m(R_z)} \left(1 - \delta_{m(R_z), -S}\right) (S_{R_z}^-)^{S-m(R_z)} \gamma_{(\mathbf{k}^{xy}, R_z), \uparrow} |R_z, S\rangle \\ \gamma_{(\mathbf{k}^{xy}, R_z), \downarrow} |R_z, m(R_z)\rangle &= \alpha_{S, m(R_z)} \left(1 - \delta_{m(R_z), S}\right) \gamma_{(\mathbf{k}^{xy}, R_z), \downarrow} (S_{R_z}^-)^{S-m(R_z)} |R_z, S\rangle \\ &= \alpha_{S, m(R_z)} \left(1 - \delta_{m(R_z), S}\right) (S_{R_z}^-)^{S-m(R_z)} \gamma_{(\mathbf{k}^{xy}, R_z), \downarrow} |R_z, S\rangle \\ &\quad + \alpha_{S, m(R_z)} (S - m(R_z)) \left(1 - \delta_{m(R_z), S}\right) (S_{R_z}^-)^{S-m(R_z)-1} \gamma_{(\mathbf{k}^{xy}, R_z), \uparrow} |R_z, S\rangle \\ &= \alpha_{S, m(R_z)} (S - m(R_z)) (S_{R_z}^-)^{S-m(R_z)-1} \gamma_{(\mathbf{k}^{xy}, R_z), \uparrow} |R_z, S\rangle \end{aligned} \quad (\text{S14.50})$$

Since

$$|R_z, S\rangle = \prod_{\mathbf{k}} \gamma_{(\mathbf{k}^{xy}, R_z), \uparrow}^\dagger |0\rangle \quad (\text{S14.51})$$

then

$$\gamma_{(\mathbf{k}^{xy}, R_z), \uparrow} |R_z, S\rangle \neq 0 \quad (\text{S14.52})$$

We thus conclude the following states give the charge -1 excitation state

$$\begin{aligned} \gamma_{\mathbf{k}^{xy}, R_z, \uparrow} |R_z, m(R_z)\rangle &\neq 0, \quad \text{with } m(R_z) \neq -S \\ \gamma_{\mathbf{k}^{xy}, R_z, \downarrow} |R_z, m(R_z)\rangle &\neq 0, \quad \text{with } m(R_z) \neq S \end{aligned} \quad (\text{S14.53})$$

We next discuss the charge $+1$ excitation. Similarly, we show that the following state describes the charge $+1$ excitation

$$\gamma_{(\mathbf{k}^{xy}, R_z), \sigma}^\dagger |R_z, m(R_z)\rangle \quad (\text{S14.54})$$

by proving that

$$[(H_0 + H_U), \gamma_{(\mathbf{k}^{xy}, R_z), \sigma}^\dagger] |R_z, m(R_z)\rangle = E_{\mathbf{k}^{xy}}^{ele} \gamma_{(\mathbf{k}^{xy}, R_z), \sigma}^\dagger |R_z, m(R_z)\rangle \quad (\text{S14.55})$$

with $E_{\mathbf{k}^{xy}}^{ele}$ the energy of the excitation state.

We now calculate

$$[H_U + H_0, \gamma_{\mathbf{k}^{xy}, R_z, \sigma}^\dagger] \quad (\text{S14.56})$$

We first show

$$\begin{aligned}
& [O_{n,(\mathbf{q}^{xy}, R_z)}^\dagger, \gamma_{\mathbf{p}^{xy}, R'_z, \sigma''}^\dagger] \\
&= \frac{1}{\sqrt{N_{xy}}} \sum_{\mathbf{k}^{xy}, \alpha, \sigma} v_{\alpha n}^* V_\alpha^*(\mathbf{k}^{xy} + \mathbf{q}^{xy}) V_\alpha(\mathbf{k}) [\gamma_{(\mathbf{k}^{xy} + \mathbf{q}^{xy}, R_z), \sigma}^\dagger \gamma_{(\mathbf{k}^{xy}, R_z), \sigma} \gamma_{(\mathbf{p}^{xy}, R'_z), \sigma''}^\dagger] \\
&= \delta_{R_z, R'_z} \frac{1}{\sqrt{N_{xy}}} \sum_{\alpha} v_{\alpha n}^* V_\alpha^*(\mathbf{p}^{xy} + \mathbf{q}^{xy}) V_\alpha(\mathbf{p}^{xy}) \gamma_{(\mathbf{p}^{xy} + \mathbf{q}^{xy}, R_z), \sigma''}
\end{aligned} \tag{S14.57}$$

and then

$$\begin{aligned}
& [O_{n,(\mathbf{q}^{xy}, R_z)}^\dagger O_{n,(\mathbf{q}^{xy}, R_z)}^\dagger, \gamma_{\mathbf{p}^{xy}, R'_z, \sigma''}^\dagger] \\
&= \delta_{R_z, R'_z} \frac{1}{N_{xy}} \sum_{\alpha, \gamma} v_{\alpha n}^* v_{\gamma n} \sum_{\mathbf{k}} V_\alpha^*(\mathbf{p}^{xy} + \mathbf{q}^{xy}) V_\alpha(\mathbf{p}^{xy}) V_\gamma(\mathbf{k}^{xy} + \mathbf{q}^{xy}) V_\gamma^*(\mathbf{k}_{xy}) \\
& \quad [\gamma_{(\mathbf{k}^{xy}, R_z), \sigma}^\dagger \gamma_{(\mathbf{k}^{xy} + \mathbf{q}^{xy}, R_z), \sigma} \gamma_{(\mathbf{p}^{xy} + \mathbf{q}^{xy}, R_z), \sigma''}^\dagger] \\
&= \delta_{R_z, R'_z} \frac{1}{N_{xy}} \sum_{\alpha, \gamma} v_{\alpha n}^* v_{\gamma n} V_\alpha^*(\mathbf{p}^{xy} + \mathbf{q}^{xy}) V_\alpha(\mathbf{p}^{xy}) V_\gamma(\mathbf{p}^{xy} + \mathbf{q}^{xy}) V_\gamma^*(\mathbf{p}_{xy}) \gamma_{(\mathbf{p}^{xy}, R_z), \sigma''}^\dagger
\end{aligned} \tag{S14.58}$$

Then we have

$$[H_U + H_0, \gamma_{\mathbf{p}^{xy}, R'_z, \sigma''}^\dagger] |R_z, m(R_z)\rangle = E_{\mathbf{p}^{xy}}^{ele} \gamma_{\mathbf{p}^{xy}, R'_z, \sigma''}^\dagger |R_z, m(R_z)\rangle \tag{S14.59}$$

where the energy function is

$$E_{\mathbf{p}^{xy}}^{ele} = \sum_{\mathbf{q}^{xy}, n} \frac{u_n}{2N_{xy}} \sum_{\alpha, \gamma, n} v_{\alpha n}^* v_{\gamma n} V_\alpha^*(\mathbf{p}^{xy} + \mathbf{q}^{xy}) V_\alpha(\mathbf{p}^{xy}) V_\gamma(\mathbf{p}^{xy} + \mathbf{q}^{xy}) V_\gamma^*(\mathbf{p}_{xy}). \tag{S14.60}$$

Therefore, we prove $\gamma_{\mathbf{p}^{xy}, R'_z, \sigma''}^\dagger |R_z, m(R_z)\rangle$ describes a charge +1 excitation state.

We note that a valid electron excitation needs to satisfy

$$\gamma_{\mathbf{p}^{xy}, R'_z, \sigma}^\dagger |R_z, m(R_z)\rangle \neq 0 \tag{S14.61}$$

We now find the condition in which Eq. S14.61 holds by evaluating

$$\gamma_{\mathbf{p}^{xy}, R'_z, \sigma}^\dagger |R_z, m(R_z)\rangle \tag{S14.62}$$

Using the commutation relation in Eq. S14.49 and the definition of $|R_z, m(R_z)\rangle$ in Eq. S14.36, we find

$$\begin{aligned}
\gamma_{\mathbf{k}^{xy}, R_z, \uparrow}^\dagger |R_z, m(R_z)\rangle &= -\alpha_{S, m(R_z)} (S - m(R_z)) (S_{R_z}^-)^{S - m(R_z) - 1} \gamma_{\mathbf{k}^{xy}, R_z, \downarrow}^\dagger |R_z, S\rangle \\
\gamma_{\mathbf{k}^{xy}, R_z, \downarrow}^\dagger |R_z, m(R_z)\rangle &= \alpha_{S, m(R_z)} \left(1 - \delta_{m(R_z), -S}\right) (S_{R_z}^-)^{S - m(R_z)} \gamma_{\mathbf{k}^{xy}, R_z, \downarrow}^\dagger |R_z, S\rangle
\end{aligned} \tag{S14.63}$$

Since

$$|R_z, S\rangle = \prod_{\mathbf{k}} \gamma_{(\mathbf{k}^{xy}, R_z), \uparrow}^\dagger |0\rangle \tag{S14.64}$$

then

$$\gamma_{(\mathbf{k}^{xy}, R_z), \downarrow}^\dagger |R_z, S\rangle \neq 0 \tag{S14.65}$$

We thus conclude the following states give the charge +1 excitation state

$$\begin{aligned}
\gamma_{\mathbf{k}^{xy}, R_z, \uparrow}^\dagger |R_z, m(R_z)\rangle &\neq 0, \quad \text{with } m(R_z) \neq S \\
\gamma_{\mathbf{k}^{xy}, R_z, \downarrow}^\dagger |R_z, m(R_z)\rangle &\neq 0, \quad \text{with } m(R_z) \neq -S
\end{aligned} \tag{S14.66}$$

From Eq. S14.50 and Eq. S14.63, we can introduce the following charge ± 1 excitation state

$$\begin{aligned} |m(R_z), \mathbf{k}^{xy}, R_z, h\rangle &= (S_{R_z}^-)^{S-m(R_z)} \gamma_{\mathbf{k}^{xy}, R_z, \uparrow} |R_z, S\rangle, \quad m(R_z) \in \{-S, -S+1, \dots, S-1\} \\ |m(R_z), \mathbf{k}^{xy}, R_z, e\rangle &= (S_{R_z}^-)^{S-m(R_z)} \gamma_{\mathbf{k}^{xy}, R_z, \downarrow}^\dagger |R_z, S\rangle, \quad m(R_z) \in \{-S+1, \dots, S-1, S\} \end{aligned} \quad (\text{S14.67})$$

with

$$\begin{aligned} \gamma_{(\mathbf{k}^{xy}, R_z), \uparrow} |R_z, m(R_z)\rangle &= \alpha_{S, m(R_z)} \left(1 - \delta_{m(R_z), -S}\right) |m(R_z), \mathbf{k}^{xy}, R_z, h\rangle \\ \gamma_{(\mathbf{k}^{xy}, R_z), \downarrow} |R_z, m(R_z)\rangle &= \alpha_{S, m(R_z)} (S - m(R_z)) |m(R_z) + 1, \mathbf{k}^{xy}, R_z, h\rangle \\ \gamma_{\mathbf{k}^{xy}, R_z, \uparrow}^\dagger |R_z, m(R_z)\rangle &= -\alpha_{S, m(R_z)} (S - m(R_z)) |m(R_z) + 1, \mathbf{k}^{xy}, R_z, e\rangle \\ \gamma_{\mathbf{k}^{xy}, R_z, \downarrow}^\dagger |R_z, m(R_z)\rangle &= \alpha_{S, m(R_z)} \left(1 - \delta_{m(R_z), -S}\right) |m(R_z), \mathbf{k}^{xy}, R_z, e\rangle \end{aligned} \quad (\text{S14.68})$$

where $\alpha_{S, m}$ has been introduced in Eq. S14.36.

We also comment that $|m(R_z), \mathbf{k}^{xy}, R_z, h/e\rangle$ is not normalized state. We now calculate the norm of $|m(R_z), \mathbf{k}^{xy}, R_z, h\rangle$

$$\begin{aligned} \langle m(R_z), \mathbf{k}^{xy}, R_z, h | m(R_z), \mathbf{k}^{xy}, R_z, h \rangle &= \langle R_z, S | \gamma_{\mathbf{k}^{xy}, R_z, \uparrow}^\dagger (S_{R_z}^+)^{S-m(R_z)} (S_{R_z}^-)^{S-m(R_z)} \gamma_{\mathbf{k}^{xy}, R_z, \uparrow} |R_z, S\rangle \\ &= \langle R_z, S | \gamma_{\mathbf{k}^{xy}, R_z, \uparrow}^\dagger (S_{R_z}^+)^{S-m(R_z)-1} (2S_{R_z}^z) (S_{R_z}^-)^{S-m(R_z)-1} \gamma_{\mathbf{k}^{xy}, R_z, \uparrow} |R_z, S\rangle \\ &\quad + \langle R_z, S | \gamma_{\mathbf{k}^{xy}, R_z, \uparrow}^\dagger (S_{R_z}^+)^{S-m(R_z)-1} S_{R_z}^- S_{R_z}^+ (S_{R_z}^-)^{S-m(R_z)-1} \gamma_{\mathbf{k}^{xy}, R_z, \uparrow} |R_z, S\rangle \\ &= \langle R_z, S | \gamma_{\mathbf{k}^{xy}, R_z, \uparrow}^\dagger (S_{R_z}^+)^{S-m(R_z)-1} (2S_{R_z}^z) (S_{R_z}^-)^{S-m(R_z)-1} \gamma_{\mathbf{k}^{xy}, R_z, \uparrow} |R_z, S\rangle \\ &\quad + \langle R_z, S | \gamma_{\mathbf{k}^{xy}, R_z, \uparrow}^\dagger (S_{R_z}^+)^{S-m(R_z)-2} (2S_{R_z}^z) S_{R_z}^+ (S_{R_z}^-)^{S-m(R_z)-1} \gamma_{\mathbf{k}^{xy}, R_z, \uparrow} |R_z, S\rangle \\ &\quad + \langle R_z, S | \gamma_{\mathbf{k}^{xy}, R_z, \uparrow}^\dagger (S_{R_z}^+)^{S-m(R_z)-2} (S_{R_z}^-) (S_{R_z}^+)^2 (S_{R_z}^-)^{S-m(R_z)-1} \gamma_{\mathbf{k}^{xy}, R_z, \uparrow} |R_z, S\rangle \\ &= \sum_{m=1}^{S-m(R_z)} \langle R_z, S | \gamma_{\mathbf{k}^{xy}, R_z, \uparrow}^\dagger (S_{R_z}^+)^{S-m(R_z)-m} 2(S_{R_z}^z) (S_{R_z}^+)^{m-1} (S_{R_z}^-)^{S-m(R_z)-1} \gamma_{\mathbf{k}^{xy}, R_z, \uparrow} |R_z, S\rangle \\ &\quad + \langle R_z, S | \gamma_{\mathbf{k}^{xy}, R_z, \uparrow}^\dagger S_{R_z}^- (S_{R_z}^+)^{S-m(R_z)} (S_{R_z}^-)^{S-m(R_z)-1} \gamma_{\mathbf{k}^{xy}, R_z, \uparrow} |R_z, S\rangle \\ &= \sum_{m=1}^{S-m(R_z)} (2m(R_z) + 2m - 1) \langle m(R_z) + 1, \mathbf{k}^{xy}, R_z, h | m(R_z) + 1, \mathbf{k}^{xy}, R_z, h \rangle \\ &= (S^2 - m(R_z)^2) \langle m(R_z) + 1, \mathbf{k}^{xy}, R_z, h | m(R_z) + 1, \mathbf{k}^{xy}, R_z, h \rangle \end{aligned} \quad (\text{S14.69})$$

We note that

$$\langle S, \mathbf{k}^{xy}, R_z, h | S, \mathbf{k}^{xy}, R_z, h \rangle = \langle R_z, S | \gamma_{\mathbf{k}^{xy}, R_z, \uparrow}^\dagger \gamma_{\mathbf{k}^{xy}, R_z, \uparrow} |R_z, S\rangle = 1 \quad (\text{S14.70})$$

Thus, we define the norm as

$$\begin{aligned} \beta_{m(R_z)} &= \langle m(R_z), \mathbf{k}^{xy}, R_z, h | m(R_z), \mathbf{k}^{xy}, R_z, h \rangle = \prod_{m=m(R_z)}^{S-1} (S^2 - m^2), \quad m(R_z) < S \\ \beta_S &= 1 \end{aligned} \quad (\text{S14.71})$$

We then calculate the norm of $|M, \mathbf{k}^{xy}, R_z, e\rangle$

$$\begin{aligned} \langle m(R_z), \mathbf{k}^{xy}, R_z, e | m(R_z), \mathbf{k}^{xy}, R_z, e \rangle &= \langle R_z, S | \gamma_{\mathbf{k}^{xy}, R_z, \downarrow} (S_{R_z}^+)^{S-m(R_z)} (S_{R_z}^-)^{S-m(R_z)} \gamma_{\mathbf{k}^{xy}, R_z, \downarrow}^\dagger |R_z, S\rangle \\ &= \sum_{m=1}^{S-m(R_z)} \langle R_z, S | \gamma_{\mathbf{k}^{xy}, R_z, \downarrow} (S_{R_z}^+)^{S-m(R_z)-m} 2(S_{R_z}^z) (S_{R_z}^+)^{m-1} (S_{R_z}^-)^{S-m(R_z)-1} \gamma_{\mathbf{k}^{xy}, R_z, \downarrow}^\dagger |R_z, S\rangle \\ &\quad + \langle R_z, S | \gamma_{\mathbf{k}^{xy}, R_z, \downarrow} S_{R_z}^- (S_{R_z}^+)^{S-m(R_z)} (S_{R_z}^-)^{S-m(R_z)-1} \gamma_{\mathbf{k}^{xy}, R_z, \downarrow}^\dagger |R_z, S\rangle \\ &= \sum_{m=1}^{S-m(R_z)} (2m(R_z) + 2m - 1) \langle m(R_z) + 1, \mathbf{k}^{xy}, R_z, e | m(R_z) + 1, \mathbf{k}^{xy}, R_z, e \rangle \end{aligned}$$

$$=(S^2 - m(R_z)^2)\langle m(R_z) + 1, \mathbf{k}^{xy}, R_z, e | m(R_z) + 1, \mathbf{k}^{xy}, R_z, e \rangle \quad (\text{S14.72})$$

Since

$$\langle S, \mathbf{k}^{xy}, R_z, e | S, \mathbf{k}^{xy}, R_z, e \rangle = \langle R_z, S | \gamma_{\mathbf{k}^{xy}, R_z, \downarrow} \gamma_{\mathbf{k}^{xy}, R_z, \downarrow}^\dagger | R_z, S \rangle = 1 \quad (\text{S14.73})$$

we have

$$\langle m(R_z), \mathbf{k}^{xy}, R_z, e | m(R_z), \mathbf{k}^{xy}, R_z, e \rangle = \beta_{m(R_z)} \quad (\text{S14.74})$$

For future reference, we also note that by acting $S_{R_z}^+$, we could generate $|m(R_z) + 1, \mathbf{k}^{xy}, R_z, e/h\rangle$ state from $|m(R_z), \mathbf{k}^{xy}, R_z, e/h\rangle$ state. To observe this, we show

$$\begin{aligned} S_{R_z}^+ |m(R_z), \mathbf{k}^{xy}, R_z, h\rangle &= S_{R_z}^+ (S_{R_z}^-)^{S-m(R_z)} \gamma_{\mathbf{k}^{xy}, R_z, \uparrow} |R_z, S\rangle \\ &= \left(2S_{R_z}^z (S_{R_z}^-)^{S-m(R_z)-1} + (S_{R_z}^-)^1 S_{R_z}^+ (S_{R_z}^-)^{S-m(R_z)-1} \right) \gamma_{\mathbf{k}^{xy}, R_z, \uparrow} |R_z, S\rangle \\ &= \sum_{m=1}^{S-m(R_z)} 2(m(R_z) + m - \frac{1}{2}) (S_{R_z}^-)^{S-m(R_z)-1} \gamma_{\mathbf{k}^{xy}, R_z, \uparrow} |R_z, S\rangle + (S_{R_z}^-)^{S-m(R_z)} S_{R_z}^+ \gamma_{\mathbf{k}^{xy}, R_z, \uparrow} |R_z, S\rangle \\ &= (S^2 - m(R_z)^2) |m(R_z) + 1, \mathbf{k}^{xy}, R_z, h\rangle \end{aligned} \quad (\text{S14.75})$$

Similarly,

$$\begin{aligned} S_{R_z}^+ |m(R_z), \mathbf{k}^{xy}, R_z, e\rangle &= S_{R_z}^+ (S_{R_z}^-)^{S-m(R_z)} \gamma_{\mathbf{k}^{xy}, R_z, \downarrow}^\dagger |R_z, S\rangle \\ &= \sum_{m=1}^{S-m(R_z)} 2(m(R_z) + m - \frac{1}{2}) (S_{R_z}^-)^{S-m(R_z)-1} \gamma_{\mathbf{k}^{xy}, R_z, \downarrow}^\dagger |R_z, S\rangle + (S_{R_z}^-)^{S-m(R_z)} S_{R_z}^+ \gamma_{\mathbf{k}^{xy}, R_z, \downarrow}^\dagger |R_z, S\rangle \\ &= (S^2 - m(R_z)^2) |m(R_z) + 1, \mathbf{k}^{xy}, R_z, e\rangle \end{aligned} \quad (\text{S14.76})$$

In summary, we have

$$\begin{aligned} |m(R_z) + 1, \mathbf{k}^{xy}, R_z, h\rangle &= \frac{1}{S^2 - m(R_z)^2} S_{R_z}^+ |m(R_z), \mathbf{k}^{xy}, R_z, h\rangle \\ |m(R_z) + 1, \mathbf{k}^{xy}, R_z, e\rangle &= \frac{1}{S^2 - m(R_z)^2} S_{R_z}^+ |m(R_z), \mathbf{k}^{xy}, R_z, e\rangle \end{aligned} \quad (\text{S14.77})$$

2. z direction hopping and out-of-plane antiferromagnetism

In the previous section, we discuss the 2D flat bands and the resulting in-plane ferromagnetic state. In the real system, even though the flat band is atomic along z direction, there could still be a weak hopping along z direction which will then generate out-of-plane antiferromagnetism.

We now introduce a weak z -direction hopping to the flat bands, such that different layers of the system are no longer decoupled. The additional z direction hopping we introduced (written in the original basis d) is

$$H_z = \sum_{\langle \mathbf{R}, \mathbf{R}' \rangle_z, \sigma} t_{z, \alpha\gamma} d_{\mathbf{R}, \alpha, \sigma}^\dagger d_{\mathbf{R}', \gamma, \sigma} = \sum_{\mathbf{k}, \sigma} t_{z, \alpha\gamma} \cos(k_z) d_{\mathbf{k}, \alpha, \sigma}^\dagger d_{\mathbf{k}, \gamma, \sigma} \quad (\text{S14.78})$$

where $\langle \mathbf{R}, \mathbf{R}' \rangle_z$ denotes nearest neighbors along z directions and $t_{z, \alpha\gamma}$ is the hopping strength.

Transforming to band basis and projecting to the flat bands, we have

$$\begin{aligned} H_{z, \gamma} &= P H_z P \\ &= \sum_{\mathbf{k}} \left[\sum_{\alpha\gamma} t_{z, \alpha\gamma} V_\alpha^*(\mathbf{k}^{xy}) V_\gamma(\mathbf{k}^{xy}) \right] \cos(k_z) \gamma_{\mathbf{k}, \sigma}^\dagger \gamma_{\mathbf{k}, \sigma} \\ &= \sum_{\mathbf{k}} f_{z, \mathbf{k}^{xy}} \cos(k_z) \gamma_{\mathbf{k}, \sigma}^\dagger \gamma_{\mathbf{k}, \sigma} \end{aligned} \quad (\text{S14.79})$$

where we utilize the fact that the wavefunction of flat bands V_α^* only depends on \mathbf{k}^{xy} and introduce

$$f_{z,\mathbf{k}^{xy}} = \sum_{\alpha\gamma} t_{z,\alpha\gamma} V_\alpha^*(\mathbf{k}^{xy}) V_\gamma(\mathbf{k}^{xy}) \quad (\text{S14.80})$$

We next treat the model with Schrieffer-Wolff transformation. We take

$$\begin{aligned} H &= h_0 + h_1 \\ h_0 &= \sum_{R_z} H_{R_z} = \sum_{R_z} \sum_{n,\mathbf{q}^{xy}} \frac{u_n}{2} O_{n,(\mathbf{q}^{xy},R_z)} O_{n,(\mathbf{q}^{xy},R_z)}^\dagger \\ h_1 &= h_{HL} + h_{LH} \\ h_{HL} &= P_H \left[\sum_{\mathbf{k}^{xy},\langle R_z,R'_z \rangle} f_{z,\mathbf{k}^{xy}} \gamma_{\mathbf{k}^{xy},R_z,\sigma}^\dagger \gamma_{\mathbf{k}^{xy},R'_z,\sigma} \right] P_L \\ h_{LH} &= P_L \left[\sum_{\mathbf{k}^{xy},\langle R_z,R'_z \rangle} f_{z,\mathbf{k}^{xy}} \gamma_{\mathbf{k}^{xy},R_z,\sigma}^\dagger \gamma_{\mathbf{k}^{xy},R'_z,\sigma} \right] P_H \end{aligned} \quad (\text{S14.81})$$

with h_0 is the unperturbed Hamiltonian and h_1 is the perturbation (Eq. S14.79). We have also separated the perturbation term into two parts: h_{HL} and h_{LH} (similarly as Eq. S13.4). The projection operators are defined as

$$\begin{aligned} P_L &= \sum_{\{m\}} |m\rangle \langle m| \\ P_H &= \mathbb{I} - P_L \end{aligned} \quad (\text{S14.82})$$

where P_L is the projection operator of the low-energy space formed by the ground states $|m\rangle$ of h_0 (Eq. S14.37) and P_H is the projection operator of the high-energy states (excitation states of h_0 , Eq. S14.68). Via Schrieffer-Wolff transformation, we will show that, the additional hopping along z direction (h_1) lifts the degeneracy of the ground states (Eq. S14.37) of the original Hamiltonian h_0 .

In practice, we note that the z -direction hopping h_1 could map a low-energy state to a high-energy state by creating an electron excitation at layer R_z and a hole excitation at layer R'_z . h_1 could also map a high-energy state to a low-energy state by reversing this procedure. To observe the effect of h_1 , we consider each term of h_1 separately

$$\begin{aligned} h_{\mathbf{k}^{xy},R_z,R'_z,\sigma} &= f_{z,\mathbf{k}^{xy}} \gamma_{\mathbf{k}^{xy},R_z,\sigma}^\dagger \gamma_{\mathbf{k}^{xy},R'_z,\sigma} \\ h_1 &= \sum_{\mathbf{k}^{xy},\langle R_z,R'_z \rangle} h_{\mathbf{k}^{xy},R_z,R'_z,\sigma} \end{aligned} \quad (\text{S14.83})$$

We mention that, for each layer, h_1 effectively created a charge ± 1 excitation. More specifically, acting h_1 on the ground state will create a charge -1 state at one layer and a charge $+1$ state at another layer. We comment that h_1 will not create a Goldstone excitation. A Goldstone excitation for the in-plane ferromagnetic state requires the particle-hole excitation at the same layer which takes the form of $\gamma_{\mathbf{k}^{xy},R_z,\sigma}^\dagger \gamma_{\mathbf{k}^{xy},R_z,\sigma'}$. Such types of excitation will not be created by simply acting h_1 on the ground states.

Since we focus on the case of nearest-neighbor hopping along z direction, we have $R_z = R'_z \pm 1$. We first consider the case with $R_z = R'_z + 1$. By acting $h_{\mathbf{k}^{xy},R_z,R_z+1,\sigma}$ on the ground state and using Eq. S14.68, we could obtain

$$\begin{aligned} & h_{\mathbf{k}^{xy},R_z,R_z+1,\uparrow} |m\rangle \\ &= \bigotimes_{R'_z=1}^{R_z-1} |R'_z, m(R'_z)\rangle \left[f_{z,\mathbf{k}^{xy}} \gamma_{\mathbf{k}^{xy},R_z,\uparrow}^\dagger \gamma_{\mathbf{k}^{xy},R_z+1,\uparrow} |R_z, m(R_z)\rangle |R_z+1, m(R_z+1)\rangle \right] \bigotimes_{R'_z=R_z+2}^{L_z} |R'_z, m(R'_z)\rangle \\ &= \bigotimes_{R'_z=1}^{R_z-1} |R'_z, M(R'_z)\rangle \left[-\alpha_{S,m(R_z)} \alpha_{S,m(R_z+1)} (-1)^{N_{xy}} f_{z,\mathbf{k}^{xy}} (1 - \delta_{m(R_z+1),-S}) (S - m(R_z)) \right] \\ & \quad \left(|m(R_z) + 1, R_z, \mathbf{k}^{xy}, e\rangle |m(R_z + 1), R_z + 1, \mathbf{k}^{xy}, h\rangle \right) \bigotimes_{R'_z=R_z+2}^{L_z} |R'_z, M(R'_z)\rangle |\Phi_a\rangle \\ & h_{\mathbf{k}^{xy},R_z,R_z+1,\downarrow} |m\rangle \end{aligned}$$

$$\begin{aligned}
&= \bigotimes_{R'_z=1}^{R_z-1} |R''_z, m(R''_z)\rangle \left[f_{z, \mathbf{k}^{xy}} \gamma_{\mathbf{k}^{xy}, R_z, \downarrow}^\dagger \gamma_{\mathbf{k}^{xy}, R_z+1, \downarrow} |R_z, m(R_z)\rangle |R_z+1, m(R_z+1)\rangle \right] \bigotimes_{R'_z=R_z+2}^{L_z} |R''_z, m(R''_z)\rangle \\
&= \bigotimes_{R'_z=1}^{R_z-1} |R''_z, m(R''_z)\rangle \left[\alpha_{S, m(R_z)} \alpha_{S, m(R_z+1)} (-1)^{N_{xy}} f_{z, \mathbf{k}^{xy}} (S - m(R_z+1)) (1 - \delta_{m(R_z), -S}) \right] \\
&\quad \left(|m(R_z), R_z, \mathbf{k}^{xy}, e\rangle |m(R_z+1)+1, R_z+1, \mathbf{k}^{xy}, h\rangle \right) \bigotimes_{R'_z=R_z+2}^{L_z} |R''_z, m(R''_z)\rangle |\Phi_a\rangle
\end{aligned} \tag{S14.84}$$

where the additional $(-1)^{N_{xy}}$ factor comes from the fermion anticommutation relation. Similarly, for the case of $R_z = R'_z - 1$

$$\begin{aligned}
&h_{\mathbf{k}^{xy}, R_z, R_z-1, \uparrow} |m\rangle \\
&= \bigotimes_{R'_z=1}^{R_z-1} |R''_z, m(R''_z)\rangle \left[-\alpha_{S, m(R_z)} \alpha_{S, m(R_z-1)} (-1)^{N_{xy}+1} f_{z, \mathbf{k}^{xy}} (1 - \delta_{m(R'_z), -S}) (S - m(R_z)) \right] \\
&\quad \left(|m(R_z-1), R_z-1, \mathbf{k}^{xy}, h\rangle |m(R_z)+1, R_z, \mathbf{k}^{xy}, e\rangle \right) \bigotimes_{R'_z=R_z+1}^{L_z} |R''_z, M(R''_z)\rangle |\Phi_a\rangle \\
&h_{\mathbf{k}^{xy}, R_z, R_z-1, \downarrow} |m\rangle \\
&= \bigotimes_{R'_z=1}^{R_z-2} |R''_z, M(R''_z)\rangle \left[\alpha_{S, m(R_z)} \alpha_{S, m(R_z-1)} (-1)^{N_{xy}+1} f_{z, \mathbf{k}^{xy}} (S - m(R_z-1)) (1 - \delta_{m(R_z), -S}) \right] \\
&\quad \left(|m(R_z-1)+1, R_z-1, \mathbf{k}^{xy}, h\rangle |m(R_z), R_z, \mathbf{k}^{xy}, e\rangle \right) \\
&\quad \bigotimes_{R'_z=R_z+1}^{L_z} |R''_z, m(R''_z)\rangle |\Phi_a\rangle
\end{aligned} \tag{S14.85}$$

where the additional $(-1)^{N_{xy}+1}$ factor comes from the fermion anticommutation relation. We can rewrite Eq. S14.84 and Eq. S14.84 in a simpler formula by introducing

$$\begin{aligned}
|m, \mathbf{k}^{xy}, R_z, R_z+1\rangle &= \bigotimes_{R'_z=1}^{R_z-1} |R''_z, m(R''_z)\rangle \left(|m(R_z), R_z, \mathbf{k}^{xy}, e\rangle |m(R_z+1), R_z+1, \mathbf{k}^{xy}, h\rangle \right) \bigotimes_{R'_z=R_z+2}^{L_z} |R''_z, m(R''_z)\rangle \\
|m, \mathbf{k}^{xy}, R_z, R_z-1\rangle &= \bigotimes_{R'_z=1}^{R_z-2} |R''_z, m(R''_z)\rangle \left(|m(R_z-1), R_z-1, \mathbf{k}^{xy}, h\rangle |m(R_z), R_z, \mathbf{k}^{xy}, e\rangle \right) \bigotimes_{R'_z=R_z+1}^{L_z} |R''_z, m(R''_z)\rangle
\end{aligned} \tag{S14.86}$$

where $|m, \mathbf{k}^{xy}, R_z, R'_z\rangle$ denotes the states obtained by creating a charge +1 excitation with momentum \mathbf{k}^{xy} at layer R_z and a charge -1 excitation with momentum \mathbf{k}^{xy} at layer R'_z on top of the ground state $|m\rangle$.

Then we have

$$\begin{aligned}
h_{\mathbf{k}^{xy}, R_z, R_z+1, \uparrow} |m\rangle &= -\alpha_{S, m(R_z)} \alpha_{S, m(R_z+1)} (-1)^{N_{xy}} f_{z, \mathbf{k}^{xy}} (1 - \delta_{m(R_z+1), -S}) (S - m(R_z)) \\
&\quad \frac{S_{R_z}^+}{S^2 - m(R_z)^2} |m, \mathbf{k}^{xy}, R_z, R_z+1\rangle \\
h_{\mathbf{k}^{xy}, R_z, R_z+1, \downarrow} |m\rangle &= \alpha_{S, m(R_z)} \alpha_{S, m(R_z+1)} (-1)^{N_{xy}} f_{z, \mathbf{k}^{xy}} (S - m(R_z+1)) (1 - \delta_{m(R_z), -S}) \\
&\quad \frac{S_{R_z+1}^+}{S^2 - m(R_z+1)^2} |m, \mathbf{k}^{xy}, R_z, R_z+1\rangle \\
h_{\mathbf{k}^{xy}, R_z, R_z-1, \uparrow} |m\rangle &= -\alpha_{S, m(R_z)} \alpha_{S, m(R_z-1)} (-1)^{N_{xy}+1} f_{z, \mathbf{k}^{xy}} (1 - \delta_{m(R_z-1), -S}) (S - m(R_z)) \\
&\quad \frac{S_{R_z}^+}{S^2 - m(R_z)^2} |m, \mathbf{k}^{xy}, R_z, R_z-1\rangle
\end{aligned}$$

$$h_{\mathbf{k}^{xy}, R_z, R_z-1, \downarrow} |m\rangle = \alpha_{S, m(R_z)} \alpha_{S, m(R_z-1)} (-1)^{N_{xy}+1} f_{z, \mathbf{k}^{xy}} (S - m(R_z - 1)) (1 - \delta_{m(R_z), -S}) \frac{S_{R_z-1}^+}{S^2 - m(R_z - 1)^2} |m, \mathbf{k}^{xy}, R_z, R_z - 1\rangle \quad (\text{S14.87})$$

where we have used the relation given in Eq. S14.77.

We then use the projection operator defined in Eq. S14.82 and find (from Eq. S14.83 and Eq. S14.87)

$$\begin{aligned} P_H h_1 P_L = \sum_{\mathbf{k}^{xy}, M, R_z} \left\{ -\alpha_{S, m(R_z)} \alpha_{S, m(R_z+1)} (-1)^{N_{xy}} f_{z, \mathbf{k}^{xy}} (1 - \delta_{m(R_z+1), -S}) (S - M(R_z)) \frac{S_{R_z}^+}{S^2 - m(R_z)^2} |m, \mathbf{k}^{xy}, R_z, R_z + 1\rangle \langle m| \right. \\ + \alpha_{S, m(R_z)} \alpha_{S, m(R_z+1)} (-1)^{N_{xy}} f_{z, \mathbf{k}^{xy}} (S - m(R_z + 1)) (1 - \delta_{M(R_z), -S}) \frac{S_{R_z+1}^+}{S^2 - m(R_z + 1)^2} |m, \mathbf{k}^{xy}, R_z, R_z + 1\rangle \langle m| \\ - \alpha_{S, m(R_z)} \alpha_{S, m(R_z-1)} (-1)^{N_{xy}+1} f_{z, \mathbf{k}^{xy}} (1 - \delta_{m(R_z-1), -S}) (S - m(R_z)) \frac{S_{R_z}^+}{S^2 - m(R_z)^2} |m, \mathbf{k}^{xy}, R_z, R_z - 1\rangle \langle m| \\ \left. + \alpha_{S, m(R_z)} \alpha_{S, m(R_z-1)} (-1)^{N_{xy}+1} f_{z, \mathbf{k}^{xy}} (S - m(R_z - 1)) (1 - \delta_{m(R_z), -S}) \frac{S_{R_z-1}^+}{S^2 - m(R_z - 1)^2} |m, \mathbf{k}^{xy}, R_z, R_z - 1\rangle \langle m| \right\} \quad (\text{S14.88}) \end{aligned}$$

We can also find $P_H h_1 P_L$ via Hermitian conjugation

$$P_L h_1 P_H = (P_H h_1 P_L)^\dagger \quad (\text{S14.89})$$

Therefore, we have rewritten the perturbation term in a similar form as Eq. S13.3

$$P_H h_1 P_L + P_L h_1 P_H = \sum_{ij} V_{ij} |L, i\rangle \langle H, j| + \text{h.c.} \quad (\text{S14.90})$$

where $|L, i\rangle$ denotes the ground states of h_0 , and $|H, j\rangle$ denotes the excitation state

$$\begin{aligned} |L, i\rangle &\sim |m\rangle \\ |H, j\rangle &\sim S_{R_z}^+ |m, \mathbf{k}^{xy}, R_z, R_z \pm 1\rangle, \quad S_{R_z \pm 1}^+ |m, \mathbf{k}^{xy}, R_z, R_z \pm 1\rangle \end{aligned} \quad (\text{S14.91})$$

The coefficient V_{ij} in Eq. S14.90 can be obtained from Eq. S14.88.

To perform the Schrieffer-Wolff transformation, we also need to obtain the energy of excitation state $|H, j\rangle$. We find

$$\begin{aligned} h_0 S_{R_z}^+ |m, \mathbf{k}^{xy}, R_z, R_z + 1\rangle &= \bigotimes_{R_z''=1}^{R_z-1} |R_z'', m(R_z'')\rangle \left(H_{R_z} S_{R_z}^+ |m(R_z), R_z, \mathbf{k}^{xy}, e\rangle |m(R_z + 1), R_z + 1, \mathbf{k}^{xy}, h\rangle \right. \\ &\quad \left. + S_{R_z}^+ |m(R_z), R_z, \mathbf{k}^{xy}, e\rangle H_{R_z+1} |m(R_z + 1), R_z + 1, \mathbf{k}^{xy}, h\rangle \right) \bigotimes_{R_z''=R_z+2}^{L_z} |R_z'', m(R_z'')\rangle \\ &= (E_{\mathbf{k}^{xy}}^{\text{hole}} + E_{\mathbf{k}^{xy}}^{\text{ele}}) S_{R_z}^+ |m, \mathbf{k}^{xy}, R_z, R_z + 1\rangle \\ h_0 S_{R_z}^+ |m, \mathbf{k}^{xy}, R_z, R_z - 1\rangle &= \bigotimes_{R_z''=1}^{R_z-2} |R_z'', m(R_z'')\rangle \left(H_{R_z-1} |m(R_z - 1), R_z - 1, \mathbf{k}^{xy}, h\rangle S_{R_z}^+ |m(R_z), R_z, \mathbf{k}^{xy}, e\rangle \right. \\ &\quad \left. + |m(R_z - 1), R_z - 1, \mathbf{k}^{xy}, h\rangle H_{R_z} S_{R_z}^+ |m(R_z), R_z, \mathbf{k}^{xy}, e\rangle \right) \bigotimes_{R_z''=R_z+1}^{L_z} |R_z'', m(R_z'')\rangle \sum_{R_z} H_{R_z} \\ &= (E_{\mathbf{k}^{xy}}^{\text{hole}} + E_{\mathbf{k}^{xy}}^{\text{ele}}) S_{R_z}^+ |m, \mathbf{k}^{xy}, R_z, R_z - 1\rangle \\ h_0 S_{R_z+1}^+ |m, \mathbf{k}^{xy}, R_z, R_z + 1\rangle &= \bigotimes_{R_z''=1}^{R_z-1} |R_z'', m(R_z'')\rangle \left(H_{R_z} |m(R_z), R_z, \mathbf{k}^{xy}, e\rangle S_{R_z+1}^+ |m(R_z + 1), R_z + 1, \mathbf{k}^{xy}, h\rangle \right. \\ &\quad \left. + |m(R_z), R_z, \mathbf{k}^{xy}, e\rangle H_{R_z+1} S_{R_z+1}^+ |m(R_z + 1), R_z + 1, \mathbf{k}^{xy}, h\rangle \right) \bigotimes_{R_z''=R_z+2}^{L_z} |R_z'', m(R_z'')\rangle \end{aligned}$$

$$\begin{aligned}
&= (E_{\mathbf{k}^{xy}}^{hole} + E_{\mathbf{k}^{xy}}^{ele}) S_{R_z+1}^+ |m, \mathbf{k}^{xy}, R_z, R_z + 1\rangle \\
h_0 S_{R_z-1}^+ |m, \mathbf{k}^{xy}, R_z, R_z - 1\rangle &= \bigotimes_{R_z''=1}^{R_z-2} |R_z'', m(R_z'')\rangle \left(H_{R_z-1} S_{R_z-1}^+ |m(R_z-1), R_z-1, \mathbf{k}^{xy}, h\rangle |m(R_z), R_z, \mathbf{k}^{xy}, e\rangle \right. \\
&\quad \left. + S_{R_z-1}^+ |m(R_z-1), R_z-1, \mathbf{k}^{xy}, h\rangle H_{R_z} |m(R_z), R_z, \mathbf{k}^{xy}, e\rangle \right) \bigotimes_{R_z''=R_z+1}^{L_z} |R_z'', m(R_z'')\rangle \sum_{R_z} H_{R_z} \\
&= (E_{\mathbf{k}^{xy}}^{hole} + E_{\mathbf{k}^{xy}}^{ele}) S_{R_z-1}^+ |m, \mathbf{k}^{xy}, R_z, R_z - 1\rangle
\end{aligned} \tag{S14.92}$$

where the charge ± 1 excitation energy is introduced in Eq. S14.44 and Eq. S14.60.

In summary, in the current problems, the high-energy states created by acting h_1 on the ground states of h_0 are

$$\begin{aligned}
&S_{R_z}^+ |m, \mathbf{k}^{xy}, R_z, R_z + 1\rangle, \quad S_{R_z+1}^+ |m, \mathbf{k}^{xy}, R_z, R_z + 1\rangle \\
&S_{R_z}^+ |m, \mathbf{k}^{xy}, R_z, R_z - 1\rangle, \quad S_{R_z-1}^+ |m, \mathbf{k}^{xy}, R_z, R_z - 1\rangle
\end{aligned} \tag{S14.93}$$

with the excitation energies being

$$E_{\mathbf{k}^{xy}}^{exact} \tag{S14.94}$$

for all four types of high-energy states, where we have also defined

$$E_{\mathbf{k}^{xy}}^{exact} = E_{\mathbf{k}^{xy}}^{hole} + E_{\mathbf{k}^{xy}}^{ele} \tag{S14.95}$$

We also mention that, in Eq. S14.93, we utilize the definition of Eq. S14.67, such that all the excitation state can be obtained by acting $S_{R_z}^+, S_{R_z\pm 1}^+$ on the $|m, \mathbf{k}^{xy}, R_z, R_z \pm 1\rangle$. In Eq. S14.67, we use $\gamma_{\mathbf{k}^{xy}, R_z, \uparrow}$ operators and $\gamma_{\mathbf{k}^{xy}, R_z, \downarrow}^\dagger$ operators to define the charge ± 1 excitation state. We could also adapt other definitions (for example, we could use $\gamma_{\mathbf{k}^{xy}, R_z, \downarrow}$ and $\gamma_{\mathbf{k}^{xy}, R_z, \uparrow}^\dagger$ operators), such that all the excitation states can be written in different formats.

However, we comment that the high-energy states (Eq. S14.93) are not normalized. We can evaluate its norm by using (Eq. S14.77, Eq. S14.71 and Eq. S14.74)

$$\begin{aligned}
&\langle m, \mathbf{k}^{xy}, R_z, R_z + 1 | (S_{R_z}^+)^\dagger S_{R_z}^+ |m, \mathbf{k}^{xy}, R_z, R_z + 1\rangle \\
&= \langle m(R_z), R_z, \mathbf{k}^{xy}, e | S_{R_z}^- S_{R_z}^+ |m(R_z), R_z, \mathbf{k}^{xy}, e\rangle \langle m(R_z+1), R_z+1, \mathbf{k}^{xy}, h | m(R_z+1), R_z+1, \mathbf{k}^{xy}, h\rangle \\
&= [S^2 - m(R_z)^2]^2 \langle m(R_z) + 1, R_z, \mathbf{k}^{xy}, e | m(R_z) + 1, R_z, \mathbf{k}^{xy}, e\rangle \beta_{m(R_z+1)} \\
&= [S^2 - m(R_z)^2]^2 \beta_{m(R_z)+1} \beta_{m(R_z+1)} = \eta_{m(R_z), m(R_z+1)}
\end{aligned}$$

$$\begin{aligned}
&\langle m, \mathbf{k}^{xy}, R_z, R_z + 1 | (S_{R_z+1}^+)^\dagger S_{R_z+1}^+ |m, \mathbf{k}^{xy}, R_z, R_z + 1\rangle = [S^2 - m(R_z+1)^2] \beta_{m(R_z+1)+1} \beta_{m(R_z)} = \eta_{m(R_z+1), m(R_z)} \\
&\langle m, \mathbf{k}^{xy}, R_z, R_z - 1 | (S_{R_z}^+)^\dagger S_{R_z}^+ |m, \mathbf{k}^{xy}, R_z, R_z - 1\rangle = [S^2 - m(R_z)^2] \beta_{m(R_z)+1} \beta_{m(R_z-1)} = \eta_{m(R_z), m(R_z-1)} \\
&\langle m, \mathbf{k}^{xy}, R_z, R_z - 1 | (S_{R_z-1}^+)^\dagger S_{R_z-1}^+ |m, \mathbf{k}^{xy}, R_z, R_z - 1\rangle = [S^2 - m(R_z-1)^2] \beta_{m(R_z-1)+1} \beta_{m(R_z)} = \eta_{m(R_z-1), m(R_z)}
\end{aligned} \tag{S14.96}$$

where we have introduced the normalization factor

$$\eta_{M, M'} = [S^2 - M^2]^2 \beta_{M+1} \beta_{M'} \tag{S14.97}$$

Now we can perform Schrieffer-Wolff transformation (Eq. S13.11)

$$H_{SW} = \frac{1}{2} \sum_{i, j, m} V_{im} V_{jm}^* \left(\frac{1}{E_{L, i} - E_{H, m}} + \frac{1}{E_{L, j} - E_{H, m}} \right) |L, i\rangle \langle L, j| \tag{S14.98}$$

We first comment that the Schrieffer-Wolff transformation describes the virtual procedure from low-energy state $|L, i\rangle$ to high-energy state $|H, m\rangle$ and then back to low-energy state $|L, j\rangle$. Therefore, the following virtual procedures could be generated and contribute to the H_{SW}

$$|L, j\rangle \rightarrow |H, m\rangle \rightarrow |L, i\rangle$$

$$\begin{aligned}
I : |m\rangle &\rightarrow \frac{1}{\sqrt{\eta_{m(R_z), m(R'_z)}}} S_{R_z}^+ |m, \mathbf{k}^{xy}, R_z, R'_z\rangle \rightarrow |m\rangle \\
II : |m\rangle &\rightarrow \frac{1}{\sqrt{\eta_{m(R'_z), m(R_z)}}} S_{R'_z}^+ |m, \mathbf{k}^{xy}, R_z, R'_z\rangle \rightarrow |m\rangle \\
III : |m\rangle &\rightarrow \frac{1}{\sqrt{\eta_{m(R_z), m(R'_z)}}} S_{R_z}^+ |m, \mathbf{k}^{xy}, R_z, R'_z\rangle \rightarrow S_{R'_z}^- S_{R_z}^+ |m\rangle \\
IV : |m\rangle &\rightarrow \frac{1}{\sqrt{\eta_{m(R'_z), m(R_z)}}} S_{R'_z}^+ |m, \mathbf{k}^{xy}, R_z, R'_z\rangle \rightarrow S_{R_z}^- S_{R'_z}^+ |m\rangle \\
&\text{with } R'_z = R_z \pm 1
\end{aligned} \tag{S14.99}$$

We now evaluate H_{SW} with contributions from each virtual procedure.

a. Contribution from I

We take

$$\begin{aligned}
|L, j\rangle &= |m\rangle, \quad |L, i\rangle = |m\rangle \\
|H, n\rangle &= \frac{1}{\sqrt{\eta_{m(R_z), m(R'_z)}}} S_{R_z}^+ |m, \mathbf{k}^{xy}, R_z, R'_z\rangle
\end{aligned} \tag{S14.100}$$

The corresponding V_{in} (from Eq. S14.88 and Eq. S14.90) is

$$V_{in} = (V_{ni}^*) = \begin{cases} -\alpha_{S, m(R_z)} \alpha_{S, m(R'_z)} (-1)^{N_{xy}} f_{z, \mathbf{k}^{xy}}^* (1 - \delta_{m(R'_z), -S}) (S - m(R_z)) \frac{\sqrt{\eta_{m(R_z), m(R'_z)}}}{S^2 - m(R_z)^2} & R'_z = R_z + 1 \\ \alpha_{S, m(R_z)} \alpha_{S, m(R'_z)} (-1)^{N_{xy}} f_{z, \mathbf{k}^{xy}}^* (1 - \delta_{m(R'_z), -S}) (S - m(R_z)) \frac{\sqrt{\eta_{m(R_z), m(R'_z)}}}{S^2 - m(R_z)^2} & R'_z = R_z - 1 \end{cases} \tag{S14.101}$$

The contribution to the H_{SW} then reads

$$\begin{aligned}
&H_{SW}^I \\
&= \sum_{m, \mathbf{k}^{xy}, R_z, R'_z = R_z \pm 1} \frac{1}{2} \left| \alpha_{S, m(R_z)} \alpha_{S, m(R'_z)} (-1)^{N_{xy}} f_{z, \mathbf{k}^{xy}} (1 - \delta_{m(R'_z), -S}) (S - m(R_z)) \frac{\sqrt{\eta_{m(R_z), m(R'_z)}}}{S^2 - m(R_z)^2} \right|^2 \\
&\quad \left(\frac{1}{-E_{\mathbf{k}^{xy}}^{exact}} + \frac{1}{-E_{\mathbf{k}^{xy}}^{exact}} \right) |m\rangle \langle m| \\
&= - \sum_{m, \mathbf{k}^{xy}, R_z, R'_z = R_z \pm 1} \frac{|f_{z, \mathbf{k}^{xy}}|^2}{E_{\mathbf{k}^{xy}}^{exact}} \prod_{i=m(R_z)+1}^{S-1} \frac{S^2 - i^2}{S(S+1) - i(i+1)} \prod_{j=m(R'_z)}^{S-1} \frac{S^2 - j^2}{S(S+1) - j(j+1)} \\
&\quad \frac{1}{S(S+1) - m(R_z)(m(R_z)+1)} (1 - \delta_{m(R'_z), -S}) (S - m(R_z))^2 |m\rangle \langle m| \\
&= - \sum_{m, \mathbf{k}^{xy}, R_z, R'_z = R_z \pm 1} \frac{|f_{z, \mathbf{k}^{xy}}|^2}{E_{\mathbf{k}^{xy}}^{exact}} \frac{(S + m(R'_z))(S - m(R_z))}{4S^2} |m\rangle \langle m|
\end{aligned} \tag{S14.102}$$

b. Contribution from II

We take

$$\begin{aligned}
|L, j\rangle &= |m\rangle, \quad |L, i\rangle = |m\rangle \\
|H, n\rangle &= \frac{1}{\sqrt{\eta_{m(R'_z), m(R_z)}}} S_{R'_z}^+ |m, \mathbf{k}^{xy}, R_z, R'_z\rangle
\end{aligned} \tag{S14.103}$$

The corresponding V_{in} (from Eq. S14.88 and Eq. S14.90) is

$$V_{in} = (V_{ni}^*) = \begin{cases} \alpha_{S,m(R_z)} \alpha_{S,m(R'_z)} (-1)^{N_{xy}} f_{z,\mathbf{k}^{xy}}^* (1 - \delta_{m(R_z),-S}) (S - m(R'_z)) \frac{\sqrt{\eta_{m(R'_z),m(R_z)}}}{S^2 - m(R'_z)^2} & R'_z = R_z + 1 \\ -\alpha_{S,m(R_z)} \alpha_{S,m(R'_z)} (-1)^{N_{xy}} f_{z,\mathbf{k}^{xy}}^* (1 - \delta_{m(R_z),-S}) (S - m(R'_z)) \frac{\sqrt{\eta_{m(R'_z),m(R_z)}}}{S^2 - m(R'_z)^2} & R'_z = R_z - 1 \end{cases} \quad (\text{S14.104})$$

The contribution to the H_{SW} then reads

$$\begin{aligned} & H_{SW}^{II} \\ &= \sum_{m,\mathbf{k}^{xy},R_z,R'_z=R_z \pm 1} \frac{1}{2} \left| \alpha_{S,m(R_z)} \alpha_{S,m(R'_z)} (-1)^{N_{xy}} f_{z,\mathbf{k}^{xy}} (1 - \delta_{m(R_z),-S}) (S - m(R'_z)) \frac{\sqrt{\eta_{m(R'_z),m(R_z)}}}{S^2 - m(R'_z)^2} \right|^2 \\ & \quad \left(\frac{1}{-E_{\mathbf{k}^{xy}}^{exact}} + \frac{1}{-E_{\mathbf{k}^{xy}}^{exact}} \right) |m\rangle \langle m| \\ &= - \sum_{m,\mathbf{k}^{xy},R_z,R'_z=R_z \pm 1} \frac{|f_{z,\mathbf{k}^{xy}}|^2}{E_{\mathbf{k}^{xy}}^{exact}} \prod_{i=m(R'_z)+1}^{S-1} \frac{S^2 - i^2}{S(S+1) - i(i+1)} \prod_{j=m(R_z)}^{S-1} \frac{S^2 - j^2}{S(S+1) - j(j+1)} \\ & \quad \frac{1}{S(S+1) - m(R'_z)(m(R'_z) + 1)} (1 - \delta_{m(R_z),-S}) (S - m(R'_z))^2 |m\rangle \langle m| \\ &= - \sum_{m,\mathbf{k}^{xy},R_z,R'_z=R_z \pm 1} \frac{|f_{z,\mathbf{k}^{xy}}|^2}{E_{\mathbf{k}^{xy}}^{exact}} \frac{(S + m(R_z))(S - m(R'_z))}{4S^2} |m\rangle \langle m| \end{aligned} \quad (\text{S14.105})$$

c. Contribution from III

We take

$$\begin{aligned} |L, j\rangle &= |m\rangle, \quad |L, i\rangle = |\tilde{m}\rangle \\ |H, n\rangle &= \frac{1}{\sqrt{\eta_{m(R_z),m(R'_z)}}} S_{R_z}^+ |m, \mathbf{k}^{xy}, R_z, R'_z\rangle, \quad R'_z = R_z \pm 1 \end{aligned} \quad (\text{S14.106})$$

where $|\tilde{m}\rangle$ denotes the ground state obtained by acting $S_{R'_z}^- S_{R_z}^+$ on the $|m\rangle$

$$|\tilde{m}\rangle = \frac{S_{R'_z}^- S_{R_z}^+}{\sqrt{[S(S+1) - m(R'_z)(m(R'_z) - 1)][S(S+1) - m(R_z)(m(R_z) + 1)]}} |m\rangle \quad (\text{S14.107})$$

where the additional coefficient in the definition of $|\tilde{m}\rangle$ has been introduced to ensure $\langle \tilde{m} | \tilde{m} \rangle = 1$ (see also Eq. S14.33). We also comment that, the contribution from $S_{R'_z}^+ S_{R_z}^- |m\rangle$ can be obtained by switching the position indices R'_z and R_z in Eq. S14.107. In practice, use the notation introduced in Eq. S14.37, we find

$$\tilde{m}(R) = \begin{cases} m(R) & R \neq R_z, R \neq R'_z \\ m(R) + 1 & R = R_z \\ m(R) - 1 & R = R'_z \end{cases} \quad (\text{S14.108})$$

The corresponding V_{in}, V_{jn}^* (from Eq. S14.88) are then

$$\begin{aligned} V_{in} = (V_{ni}^*) &= \begin{cases} -\alpha_{S,m(R_z)} \alpha_{S,m(R'_z)} (-1)^{N_{xy}} f_{z,\mathbf{k}^{xy}}^* (1 - \delta_{m(R'_z),-S}) (S - m(R_z)) \frac{\sqrt{\eta_{m(R_z),m(R'_z)}}}{S^2 - m(R_z)^2} & R'_z = R_z + 1 \\ \alpha_{S,m(R_z)} \alpha_{S,m(R'_z)} (-1)^{N_{xy}} f_{z,\mathbf{k}^{xy}}^* (1 - \delta_{m(R'_z),-S}) (S - m(R_z)) \frac{\sqrt{\eta_{m(R_z),m(R'_z)}}}{S^2 - m(R_z)^2} & R'_z = R_z - 1 \end{cases} \\ V_{nj} &= \begin{cases} \alpha_{S,\tilde{m}(R_z)} \alpha_{S,\tilde{m}(R'_z)} (-1)^{N_{xy}} f_{z,\mathbf{k}^{xy}} (1 - \delta_{\tilde{m}(R_z),-S}) (S - \tilde{m}(R'_z)) \frac{\sqrt{\eta_{\tilde{m}(R'_z),\tilde{m}(R_z)}}}{S^2 - \tilde{m}(R'_z)^2} & R'_z = R_z + 1 \\ -\alpha_{S,\tilde{m}(R_z)} \alpha_{S,\tilde{m}(R'_z)} (-1)^{N_{xy}} f_{z,\mathbf{k}^{xy}} (1 - \delta_{\tilde{m}(R_z),-S}) (S - \tilde{m}(R'_z)) \frac{\sqrt{\eta_{\tilde{m}(R'_z),\tilde{m}(R_z)}}}{S^2 - \tilde{m}(R'_z)^2} & R'_z = R_z - 1 \end{cases} \end{aligned} \quad (\text{S14.109})$$

The contribution to the H_{SW} then reads

$$\begin{aligned}
& H_{SW}^{III} \\
&= \sum_{m, \mathbf{k}^{xy}, R_z, R'_z = R_z \pm 1} \frac{1}{2} \left(\frac{1}{-E_{\mathbf{k}^{xy}}^{exact}} + \frac{1}{-E_{\mathbf{k}^{xy}}^{exact}} \right) |m\rangle \langle \tilde{m}| \\
& \quad \frac{\alpha_{S, m(R_z)} \alpha_{S, m(R'_z)} \alpha_{S, \tilde{m}(R_z)} \alpha_{S, \tilde{m}(R'_z)} (-1) |f_{z, \mathbf{k}^{xy}}|^2 (1 - \delta_{m(R'_z), -S}) (1 - \delta_{\tilde{m}(R_z), -S}) (S - m(R_z)) (S - \tilde{m}(R'_z))}{\sqrt{\eta_{m(R_z), m(R'_z)} \eta_{\tilde{m}(R_z), \tilde{m}(R'_z)}}} \\
& \quad \frac{1}{(S^2 - m(R_z)^2) (S^2 - \tilde{m}(R'_z)^2)} \\
&= \sum_{m, \mathbf{k}^{xy}, R_z, R'_z = R_z \pm 1} \frac{|f_{z, \mathbf{k}^{xy}}|^2}{E_{\mathbf{k}^{xy}}^{exact}} |m\rangle \langle \tilde{m}| (S - m(R_z)) (S - m(R'_z) - 1) \\
& \quad \prod_{i=m(R_z)+1}^{S-1} \frac{S^2 - i^2}{S(S+1) - i(i+1)} \prod_{j=m(R'_z)}^{S-1} \frac{S^2 - i^2}{S(S+1) - i(i+1)} \\
& \quad \frac{1}{\sqrt{S(S+1) - m(R_z)(m(R_z)+1)} \sqrt{S(S+1) - m(R'_z)(m(R'_z)-1)}} \\
&= \sum_{m, \mathbf{k}^{xy}, R_z, R'_z = R_z \pm 1} \frac{|f_{z, \mathbf{k}^{xy}}|^2}{E_{\mathbf{k}^{xy}}^{exact}} \frac{\sqrt{S(S+1) - m(R_z)(m(R_z)+1)} \sqrt{S(S+1) - m(R'_z)(m(R'_z)-1)}}{4S^2} |m\rangle \langle \tilde{m}| \quad (S14.110)
\end{aligned}$$

d. Contribution from IV

We take

$$\begin{aligned}
|L, j\rangle &= |m\rangle, \quad |L, i\rangle = |\tilde{m}\rangle \\
|H, n\rangle &= \frac{1}{\sqrt{\eta_{m(R'_z), m(R_z)}}} S_{R'_z}^+ |m, \mathbf{k}^{xy}, R_z, R'_z\rangle, \quad R'_z = R_z \pm 1 \quad (S14.111)
\end{aligned}$$

where $|\tilde{m}\rangle$ denotes the ground state obtained by acting $S_{R_z}^- S_{R'_z}^+$ on the $|m\rangle$

$$|\tilde{m}\rangle = \frac{S_{R_z}^- S_{R'_z}^+}{\sqrt{[S(S+1) - m(R_z)(m(R_z)-1)][S(S+1) - m(R'_z)(m(R'_z)+1)]}} |m\rangle \quad (S14.112)$$

where the additional coefficient in the definition of $|\tilde{m}\rangle$ has been introduced to ensure $\langle \tilde{m} | \tilde{m} \rangle = 1$ (see also Eq. S14.33). In practice, using the notation introduced in Eq. S14.37, we find

$$\tilde{m}(R) = \begin{cases} m(R) & R \neq R_z, R \neq R'_z \\ m(R) - 1 & R = R_z \\ m(R) + 1 & R = R'_z \end{cases} \quad (S14.113)$$

The corresponding V_{in}, V_{jn}^* (from Eq. S14.88) are then

$$\begin{aligned}
V_{in} = (V_{ni}^*) &= \begin{cases} -\alpha_{S, m(R'_z)} \alpha_{S, m(R_z)} (-1)^{N_{xy}} f_{z, \mathbf{k}^{xy}}^* (1 - \delta_{m(R_z), -S}) (S - m(R'_z)) \frac{\sqrt{\eta_{m(R'_z), m(R_z)}}}{S^2 - m(R'_z)^2} & R'_z = R_z - 1 \\ \alpha_{S, m(R'_z)} \alpha_{S, m(R_z)} (-1)^{N_{xy}} f_{z, \mathbf{k}^{xy}}^* (1 - \delta_{m(R_z), -S}) (S - m(R'_z)) \frac{\sqrt{\eta_{m(R'_z), m(R_z)}}}{S^2 - m(R'_z)^2} & R'_z = R_z + 1 \end{cases} \\
V_{nj} &= \begin{cases} \alpha_{S, \tilde{m}(R'_z)} \alpha_{S, \tilde{m}(R_z)} (-1)^{N_{xy}} f_{z, \mathbf{k}^{xy}} (1 - \delta_{\tilde{m}(R'_z), -S}) (S - \tilde{m}(R_z)) \frac{\sqrt{\eta_{\tilde{m}(R_z), \tilde{m}(R'_z)}}}{S^2 - \tilde{m}(R_z)^2} & R'_z = R_z - 1 \\ -\alpha_{S, \tilde{m}(R'_z)} \alpha_{S, \tilde{m}(R_z)} (-1)^{N_{xy}} f_{z, \mathbf{k}^{xy}} (1 - \delta_{\tilde{m}(R'_z), -S}) (S - \tilde{m}(R_z)) \frac{\sqrt{\eta_{\tilde{m}(R_z), \tilde{m}(R'_z)}}}{S^2 - \tilde{m}(R_z)^2} & R'_z = R_z + 1 \end{cases} \quad (S14.114)
\end{aligned}$$

The contribution to the H_{SW} then reads

$$H_{SW}^{IV}$$

$$\begin{aligned}
&= \sum_{m, \mathbf{k}^{xy}, R_z, R'_z = R_z \pm 1} \frac{1}{2} \left(\frac{1}{-E_{\mathbf{k}^{xy}}^{exact}} + \frac{1}{-E_{\mathbf{k}^{xy}}^{exact}} \right) |m\rangle \langle \tilde{m}| \\
&\quad \alpha_{S, m(R'_z)} \alpha_{S, m(R_z)} \alpha_{S, \tilde{m}(R'_z)} \alpha_{S, \tilde{m}(R_z)} (-1) |f_{z, \mathbf{k}^{xy}}|^2 (1 - \delta_{m(R_z), -S}) (1 - \delta_{\tilde{m}(R'_z), -S}) (S - m(R'_z)) (S - \tilde{m}(R_z)) \\
&\quad \frac{\sqrt{\eta_{m(R'_z), m(R_z)} \eta_{\tilde{m}(R_z), \tilde{m}(R'_z)}}}{(S^2 - m(R'_z)^2) (S^2 - \tilde{m}(R_z)^2)} \\
&= \sum_{m, \mathbf{k}^{xy}, R_z, R'_z = R_z \pm 1} \frac{|f_{z, \mathbf{k}^{xy}}|^2}{E_{\mathbf{k}^{xy}}^{exact}} |m\rangle \langle \tilde{m}| (S - m(R'_z)) (S - m(R_z) - 1) \\
&\quad \prod_{i=m(R'_z)+1}^{S-1} \frac{S^2 - i^2}{S(S+1) - i(i+1)} \prod_{j=m(R_z)}^{S-1} \frac{S^2 - i^2}{S(S+1) - i(i+1)} \\
&\quad \frac{1}{\sqrt{S(S+1) - m(R'_z)(m(R'_z)+1)} \sqrt{S(S+1) - m(R_z)(m(R_z)-1)}} \\
&= \sum_{m, \mathbf{k}^{xy}, R_z, R'_z = R_z \pm 1} \frac{|f_{z, \mathbf{k}^{xy}}|^2}{E_{\mathbf{k}^{xy}}^{exact}} \frac{\sqrt{S(S+1) - m(R'_z)(m(R'_z)+1)} \sqrt{S(S+1) + m(R_z)(m(R_z)-1)}}{4S^2} |m\rangle \langle \tilde{m}| \quad (\text{S14.115})
\end{aligned}$$

e. *Effective spin-spin interaction terms*

We combine Eq. S14.102, Eq. S14.105, Eq. S14.110, Eq. S14.115, and find the additional term generated by Schrieffer-Wolff transformation is

$$\begin{aligned}
H_{SW} &= H_{SW}^I + H_{SW}^{II} + H_{SW}^{III} + H_{SW}^{IV} \\
&= \sum_{m, \mathbf{k}^{xy}, R_z, R'_z = R_z \pm 1} \frac{|f_{z, \mathbf{k}^{xy}}|^2 - S^2 + m(R_z)m(R'_z)}{E_{\mathbf{k}^{xy}}^{exact} 2S^2} |m\rangle \langle m| \\
&\quad \sum_{m, \mathbf{k}^{xy}, R_z, R'_z = R_z \pm 1} \frac{|f_{z, \mathbf{k}^{xy}}|^2}{E_{\mathbf{k}^{xy}}^{exact}} \left[\frac{\sqrt{S(S+1) - m(R_z)(m(R_z)+1)} \sqrt{S(S+1) + m(R'_z)(m(R'_z)-1)}}{4S^2} |m\rangle \langle \tilde{m}| \right. \\
&\quad \left. + \frac{\sqrt{S(S+1) - m(R'_z)(m(R'_z)+1)} \sqrt{S(S+1) + m(R_z)(m(R_z)-1)}}{4S^2} |m\rangle \langle \tilde{m}| \right] \quad (\text{S14.116})
\end{aligned}$$

where $|\tilde{m}\rangle$, $|\tilde{\tilde{m}}\rangle$ states are defined via Eq. S14.108 and Eq. S14.113 respectively.

In a more compact formula, we find

$$\begin{aligned}
H_{SW} &= \sum_{m, \mathbf{k}^{xy}, R_z, R'_z = R_z \pm 1} \frac{|f_{z, \mathbf{k}^{xy}}|^2 - S^2 + m(R_z)m(R'_z)}{E_{\mathbf{k}^{xy}}^{exact} 2S^2} |m\rangle \langle m| \\
&\quad + \sum_{m, \mathbf{k}^{xy}, R_z, R'_z = R_z \pm 1} \frac{|f_{z, \mathbf{k}^{xy}}|^2}{E_{\mathbf{k}^{xy}}^{exact}} \left[\frac{\sqrt{S(S+1) - m(R_z)(m(R_z)+1)} \sqrt{S(S+1) + m(R'_z)(m(R'_z)-1)}}{4S^2} \left[|m\rangle \langle \tilde{m}| + |\tilde{\tilde{m}}\rangle \langle m| \right] \right] \quad (\text{S14.117})
\end{aligned}$$

We can rewrite Eq. S14.117 in a more compact form via the following spin operators (Eq. S14.30)

$$\begin{aligned}
S_{R_z}^{x,y,z} &= \sum_{\mathbf{k}^{xy}, \sigma, \sigma'} \gamma_{\mathbf{k}^{xy}, R_z, \sigma}^\dagger \frac{\sigma_{\sigma\sigma'}^{x,y,z}}{2} \gamma_{\mathbf{k}^{xy}, R_z, \sigma'} \\
S_{R_z}^+ &= S_{R_z}^x + iS_{R_z}^y \\
S_{R_z}^- &= S_{R_z}^x - iS_{R_z}^y \quad (\text{S14.118})
\end{aligned}$$

We find

$$S_{R_z}^z S_{R'_z}^z |m\rangle = m(R_z) m(R'_z) |m\rangle \quad (\text{S14.119})$$

Thus, acting on the ground state manifolds, we have

$$\sum_m m(R_z)m(R'_z)|m\rangle\langle m| = S_{R_z}^z S_{R'_z}^z \quad (\text{S14.120})$$

Also, we find

$$\begin{aligned} & S_{R_z}^+ S_{R'_z}^- |m\rangle \\ &= \left[\bigotimes_{R''_z \neq R_z, R''_z \neq R'_z} |R''_z, m(R''_z)\rangle \right] S_{R_z}^+ |R_z, m(R_z)\rangle S_{R'_z}^- |R'_z, m(R'_z)\rangle \\ &= \bigotimes_{R''_z \neq R_z, R''_z \neq R'_z} |R''_z, m(R''_z)\rangle \left[\sqrt{S(S+1) - m(R_z)(m(R_z)+1)} |m(R_z)+1\rangle \sqrt{S(S+1) - m(R'_z)(m(R'_z)-1)} |m(R'_z)-1\rangle \right] \\ &= \sqrt{S(S+1) - m(R_z)(m(R_z)+1)} \sqrt{S(S+1) + m(R'_z)(m(R'_z)-1)} |\tilde{m}\rangle \end{aligned} \quad (\text{S14.121})$$

Therefore, we have the following identity

$$\sum_m |\tilde{m}\rangle\langle m| = \frac{1}{\sqrt{S(S+1) - m(R_z)(m(R_z)+1)} \sqrt{S(S+1) + m(R'_z)(m(R'_z)-1)}} S_{R_z}^+ S_{R'_z}^- \quad (\text{S14.122})$$

In addition,

$$\begin{aligned} & S_{R_z}^- S_{R'_z}^+ |\tilde{m}\rangle \\ &= \left[\bigotimes_{R''_z \neq R_z, R''_z \neq R'_z} |R''_z, m(R''_z)\rangle \right] S_{R_z}^- |R_z, m(R_z)+1\rangle S_{R'_z}^+ |R'_z, m(R'_z)-1\rangle \\ &= \bigotimes_{R''_z \neq R_z, R''_z \neq R'_z} |R''_z, m(R''_z)\rangle \left[\sqrt{S(S+1) - m(R_z)(m(R_z)+1)} |m(R_z)\rangle \sqrt{S(S+1) - m(R'_z)(m(R'_z)-1)} |m(R'_z)\rangle \right] \\ &= \sqrt{S(S+1) - m(R_z)(m(R_z)+1)} \sqrt{S(S+1) + m(R'_z)(m(R'_z)-1)} |m\rangle \end{aligned} \quad (\text{S14.123})$$

Therefore, we have the following identity

$$\sum_m |m\rangle\langle \tilde{m}| = \frac{1}{\sqrt{S(S+1) - m(R_z)(m(R_z)+1)} \sqrt{S(S+1) + m(R'_z)(m(R'_z)-1)}} S_{R_z}^- S_{R'_z}^+ \quad (\text{S14.124})$$

Combining Eq. S14.117, Eq. S14.120, Eq. S14.122 and Eq. S14.124, we could rewrite the H_{SW} with the spin operators as

$$\begin{aligned} H_{SW} &= \sum_{R_z, R'_z = \pm 1} J \left[-S^2 + S_{R_z}^z S_{R'_z}^z + \frac{1}{2} S_{R_z}^+ S_{R'_z}^- + \frac{1}{2} S_{R_z}^- S_{R'_z}^+ \right] = \sum_{R_z, R'_z = \pm 1} J \left[-S^2 + \mathbf{S}_{R_z} \cdot \mathbf{S}_{R'_z} \right] \\ J &= \sum_{\mathbf{k}} \frac{|f_{z, \mathbf{k}^{xy}}|^2}{2E_{\mathbf{k}}^{ext} S^2} > 0 \end{aligned} \quad (\text{S14.125})$$

Therefore, we could observe that the z -direction hopping generates inter-layer Heisenberg-types of antiferromagnetic interactions ($J > 0$). The antiferromagnetic interactions then stabilize the following type-A antiferromagnetic state

$$\bigotimes_{R_z} |R_z, (-1)^{R_z} S\rangle \quad (\text{S14.126})$$

We also note that, by combining all terms, $H_{SW}^I, H_{SW}^{II}, H_{SW}^{III}, H_{SW}^{IV}$, we recover the SU(2) symmetry of the system.

Finally, we comment that, we could also introduce an in-plane dispersion to the flat bands. However, as we demonstrated in Ref. [108], the in-plane ferromagnetic coupling generated by quantum geometry is proportional to U , and the antiferromagnetic coupling generated by the dispersion is proportional to D^2/U with D the bandwidth of the system. Therefore, the in-plane dispersion will not destroy the in-plane ferromagnetism as long as the dispersion is weak.